

Efficient Integral Equation Algorithms and Their Application to RFID Installation

by

Joseph Daniel Brunett

A dissertation submitted in partial fulfillment
of the requirements for the degree of
Doctor of Philosophy
(Electrical Engineering)
in The University of Michigan
2008

Doctoral Committee:

Research Scientist Valdis V. Liepa, Co-Chair
Research Scientist Dipak L. Sengupta, Co-Chair
Professor Eric Michielssen
Professor Richard A. Scott
Assistant Professor Anthony Grbic

© Joseph Daniel Brunett 2008
All Rights Reserved

To my son Nathan.

ACKNOWLEDGEMENTS

I would first like to thank my wife Jennifer for believing in me throughout these many years of study. It is seldom you find a soul mate in life, but she is mine. I also wish to thank my parents, Fel and Pat Brunett, for not only providing me with a rich and explorative childhood, but for their continued support without which this work could never have been completed.

Next, I wish to acknowledge and thank my academic advisor, Dr. Val Liepa, for his mentorship, guidance, and most importantly for his friendship during my time here at Michigan. There are few people as knowledgeable and as generous as Val, and he is a joy to work with. I also wish to thank my co-chair, Professor Dipak Sengupta for his engaging discussions and for sharing his thorough understanding of electromagnetic principles and their origins.

Furthermore, I am indebted to my committee members Professor Eric Michielssen, Assistant Professor Tony Grbic, and Professor Richard Scott for their consideration of this work. I am also grateful to Professor Senior for discussions on low frequency fields.

Last but not least, I wish to recognize and thank all of the members of the University of Michigan Radiation Laboratory, both past and present, for their support and continued friendship. I am proud to be a member of such an outstanding group of individuals.

TABLE OF CONTENTS

DEDICATION		ii
ACKNOWLEDGEMENTS		iii
LIST OF TABLES		vi
LIST OF FIGURES		vii
ABSTRACT		ix
CHAPTER		
1	Introduction	1
	1.1 Motivation	1
	1.2 Discussion	2
	1.2.1 Radio Frequency Identification (RFID)	2
	1.2.2 Computational Electromagnetics	4
	1.3 Thesis Overview	6
2	Integral Equations and Fast Algorithms	8
	2.1 Time-Harmonic Electromagnetic Fields	8
	2.1.1 Maxwell's Equations and The Wave Equation	9
	2.1.2 Volume Equivalence	10
	2.1.3 Impedance Sheet Boundary Conditions	13
	2.2 Integral Equation Discretization	23
	2.2.1 Volume & Surface Integral Equations	23
	2.2.2 Integral Equation Discretization	25
	2.3 Fast Algorithms	32
	2.3.1 Matrix Compression	32
3	Multilevel Geometry Description	40
	3.1 Facet Based Geometry	41
	3.1.1 Protofacets	44
	3.1.2 Graph Nodes	48
	3.1.3 Recursing the Graph	53

3.2	Interactions and Interconnectivity	55
3.2.1	Minimum Interaction Set	56
3.2.2	Expansion Function Connectivity	57
3.3	Cost Analysis	61
3.3.1	Structure Storage	61
3.3.2	Determining the Minimum Interaction Set	61
3.3.3	Near and Distant Interactions	62
3.3.4	Overall Picture	63
4	CQ Bases and the Multibasis Method	65
4.1	Current-Charge (CQ) Expansion	65
4.2	Preconditioning Methods	69
4.2.1	Diagonal Preconditioning	69
4.2.2	Tree Basis Rearrangement	70
4.2.3	Multiresolution (MR) Method	72
4.3	The Multibasis (MB) Method	73
4.4	Cost Analysis	79
4.4.1	Sub-basis Matrix Assembly and Storage	79
4.4.2	Applying Basis Transformations	80
5	Test and Measurement	82
5.1	Field Behavior	82
5.2	Loop Antennas	84
5.2.1	Magnetic Field Coupling	84
5.2.2	Receiving Loop Sensitivity	86
5.2.3	Transmitting Loops	88
5.3	Magnetic Field Measurements	88
5.3.1	Shield Currents and Shielded Loops	89
5.4	Review	91
6	Software Validation and System Optimization	92
6.1	Efficiency	92
6.1.1	Setup Time and Memory Overhead	92
6.1.2	Basis Selection and Solution	94
6.2	Accuracy	99
6.2.1	PEC Sphere	99
6.2.2	Scattering by Finite Material Disk	100
6.3	Applicability	106
6.3.1	Tire Tag Placement	106
7	Conclusions and Future Work	111
7.1	Summary	111
7.2	Future Work	112

BIBLIOGRAPHY	114
-------------------------------	------------

LIST OF TABLES

Table

6.1	Non-magnetic thin metal sheet impedance values.	102
6.2	Magnetic thin metal sheet impedance values.	105

LIST OF FIGURES

Figure

2.1	Homogeneous slab and sheet current boundary.	14
2.2	Forward and backward sheet equivalent problems.	20
2.3	Diagram of a thick slab immersed in a standing wave.	21
2.4	Single Patch (SP) expansion function.	29
2.5	Divergence conforming expansion functions.	30
2.6	Curl conforming expansion functions.	31
2.7	Multipole alignment including local coordinate frames.	39
3.1	Forming an MLGD structure from an existing library.	42
3.2	Diagram of the MLGD oriented graph structure.	43
3.3	Translation and rotation of a facet about a line through a point.	49
3.4	Diagram outlining the procedure for construction of an MLGD node.	52
3.5	Recursion tree of the MLGD structure.	54
3.6	Divergence conforming bridge bases.	59
3.7	Curl conforming bridge bases.	60
3.8	Original and equivalent Matrix-Vector Product (MVP).	64
4.1	Tree-Basis Rearrangement (TBR) equivalent bases.	71
4.2	Multibasis (MB) iterative procedure.	76
4.3	Numerical method overview.	80
5.1	Change in magnetic field near a PEC wall.	83
5.2	Low frequency shield currents.	89
5.3	Shielded loop and measurement setup.	90
6.1	Memory overhead vs. the number of RWG unknowns.	93
6.2	Pre-compute time for a square PEC plate and PEC cylinder array.	94
6.3	MB method convergence for PEC sphere.	95
6.4	MB method convergence for PEC disk.	97
6.5	Solution time in relation to the number of RWG unknowns.	98
6.6	Current distribution on a PEC sphere.	100
6.7	Material disk LF current distribution.	101
6.8	Material disk H-field shielding: coaxial.	103

6.9	Material disk H-field shielding: coplanar.	106
6.10	Diagram of TPM sensor and initiator pair with tire cross-section. . .	107
6.11	Setup and simulation of wheel rim with LF coil excitation.	108
6.12	Magnetic field strength vs. tire rotation angle	109

ABSTRACT

Efficient Integral Equation Algorithms and Their Application to RFID Installation

by

Joseph Daniel Brunett

Co-Chairs: Valdis V. Liepa and Dipak L. Sengupta

This research reduces the expense of solving multiscale frequency domain surface integral equation problems by application of an efficient hierarchical geometry description and an alternative approach to matrix conditioning. The cost of preparing a structure for simulation is minimized by multilevel retention of facet translation and rotation data. Overlapping sub-domain bases are then simultaneously applied via a new iterative procedure that ascertains the common sub-basis solution to the overdetermined system. This approach is highly convergent and provides accurate solutions without degradation to existing $O(N)$ fast algorithms. New sheet impedance forms are introduced ensuring proper material representation. These methods are then applied in the optimization of low frequency Tire Pressure Monitoring Sensor placement on a metallic vehicle rim. Test methods required for accurate measurement of low frequency magnetic fields are discussed and measurements of an automobile wheel under like stimuli match simulated results.

CHAPTER 1

Introduction

1.1 Motivation

Radio Frequency Identification (RFID) devices have come a long way in the past sixty years. The concept first originated during World War II as a method of identifying aircraft returning to base. After the war, development centered on governmental tracking of nuclear material, but it was not until the 1970's that the first commercial patents were granted for their use [1]. Today these devices abound thanks to advancements in both their production and the development of commercial standards. Applicable to both the public marketplace and private sectors, these devices are revolutionizing the way we track goods, perform transactions, and organize our world. RFID devices are used in such a diverse range of applications as supply chain management, electronic payment, livestock tracking, passport interrogation, patient care, medical training, vehicle safety, and theft deterrence [2–10]. Just as diverse as their applications, the frequencies at which these devices operate range from from the low frequency (LF) portion of the radio spectrum to microwave frequencies. They are designed to take advantage of inductive coupling, capacitive coupling, reflected, and transmitted power. They may be active (battery powered) or more preferably passive (radio frequency field powered) devices. And yet, despite their abundance, it is

as true now as it was 60 years ago that a great deal of research and development is still needed [11]. Thankfully, the advancing computational power of the personal computer (PC) makes it possible to model the local electrical characteristics of these devices and suggests that full-wave electromagnetic modeling of the environment may now be possible. Such software could help to select RFID tag placement, interrogator shape and distance, and predict overall system limitations important in real world designs. Motivated by the potential of such a simulator, this thesis delves into the implementation of a full-wave software package with primary application to simulating low frequency environments.

1.2 Discussion

Motivated to implement and utilize such a software package, this section classifies RFID devices and discusses the challenges currently faced in numerical simulation of electrically small structures.

1.2.1 Radio Frequency Identification (RFID)

Radio Frequency Identification is a method of automatically identifying an object from locally stored data via radio frequency interrogation. Placed on or as an integral part of the object is an RFID tag, also called a transponder, that stores this information and makes it available to the interrogator. While it is conceivable that almost any radio frequency device communicating data might be labeled an RFID tag, at present these devices typically fall into one of the following two main classifications.

The first class includes those devices that operate on the principle of magnetic flux coupling; primarily Low Frequency Identification (LFID) and High Frequency Identification (HFID) devices operating in the quasi-static regime. For these devices the open-circuit voltage available to drive a load is proportional to the frequency

(time-rate of change) of the magnetic flux passing through a loop of finite area. These flux-coupled devices are preferred because increased sensitivity is achieved by increasing the antenna quality factor, either through greater numbers of turns or by loading with inexpensive low loss magnetic material. (Such materials are available with relative permeabilities on the order of 2,000 to 10,000 in this frequency range.) In contrast, electric dipole sources require very high voltages to achieve similar sensitivity. Not only are such voltages dangerous, but they are also voltage breakdown limited.

LFIDs typically operate at 125 kHz or 134 kHz and the associated tags, interrogators, and environments into which they are placed are all electrically small. LF transponders require a significant number of wire turns about a ferromagnetic core to provide adequate voltage to an embedded microprocessor. Alternatively, HFIDs operate in the 13.56 MHz Industrial Scientific & Medical (ISM) band [12] and require far fewer loop turns due to increased frequency. Since fewer turns are necessary, these devices can be manufactured using lithographic techniques at reduced cost. However, they are more sensitive to changes in their environment. Passive versions of these devices respond by modulating the flux coupled through the loop, and this flux modulation is detected by the interrogator.

The second class of RFID transponders relies on capacitive coupling or reflected power communications and typically operates in the UHF or microwave spectrum. Because these devices represent a far larger fraction of a wavelength they achieve acceptable performance using linear antenna elements, compact antennas, or meander lines. Some of these devices store received energy or modulate their scattering cross section while others use internal batteries to transmit information back to the interrogator.

In many applications the principles associated with both classifications are intermingled, including transponders interrogated at LF frequencies that respond by

battery power at UHF frequencies. Such devices require software capable of simulation across the entire spectrum, and the work presented in this thesis is wholly applicable. For the reasons discussed in the next two sections, the development of both numerical and test and measurement methods for the quasi-static regime are emphasized in this work.

1.2.2 Computational Electromagnetics

The development of computational electromagnetics (CEM) software has been ongoing for many years and recent advances allow full-wave simulation of a number of RFID structures.

For devices representing a significant fraction of a wavelength (such as UHF or microwave RFIDs), existing fast algorithms hybridized with the method of moments [13–15], the finite element boundary integral method [14], and finite difference methods [15], are implemented in a number of commercial packages [16–19]. Furthermore, the environments into which these devices are placed is typically many if not hundreds of wavelengths in dimension. Numerical methods for simulating these electrically large environments have been actively researched for over four decades.

Alternatively, the simulation of electrically small devices (such as LFID and HFID transponders and their environments) is known to encounter difficulties that are only more recently addressed. Some of these issues include:

1. The number of unknowns required in the volumetric discretization of an RFID tag is manageable. However, a volumetric mesh encompassing large scale “environmental” structures requires far too many unknowns, particularly for surfaces exhibiting fast radius of curvature. Surface integral equation (SIE) formulations become necessary, but even for an $O(N)$ surface based approach the number of unknowns is bound by finite computer memory. For cartesian array type structures redundancy minimization algorithms (RMA’s) that rely on struc-

tural regularity at high frequencies [20–22] help to rein in overhead, but are less applicable to arbitrary geometries and must be modified for use on electrically small structures.

2. The widespread surface based electric field integral equation (EFIE) employing Rao-Wilton-Glisson (RWG) expansion functions [23] fails to properly capture the Helmholtz/Hodge decomposition of the magnetic and electric fields at low frequencies (or fine mesh discretization). A diverse range of alternative expansion functions and advanced weighting procedures have been developed to remedy this situation[24–26]. However, these expansions result in slowly converging systems of equations, requiring specialized preconditioning of the iterative method. Recent works improve system conditioning by transforming non-solenoidal expansions into bases with greater spectral resolution [26–29].
3. Efficient fast algorithms used to compress electrically distant interactions fail when applied to small distances where evanescent modes dominate. While some algorithms are kernel independent [30, 31], the more efficient diagonalized versions of the Multilevel Fast Multipole Method [32, 33] require reformulation. The un-diagonalized Low Frequency Multilevel Fast Multipole Algorithm (LF-MLFMA) [34] and more recent broadband diagonalized versions [35, 36] employing evanescent wave expansions provide $O(N)$ performance due to scale invariance at low frequencies.
4. Due to low frequency field penetration, it is necessary that material characteristics be included in the numerical solver. Assuming an SIE approach, surface equivalent or multi-body equivalence forms [34] are desirable. However, if high contrast exists between different materials, multi-body formulations can result in excessive numbers of unknowns due to highly oscillatory kernels within slow wave materials. Thus, formulations for surface integral equation methods that

include analytical approximations for slow wave material characteristics are more applicable, limiting the number of unknowns to that required to properly represent the surface radius of curvature.

1.3 Thesis Overview

This work takes into account the above concerns and extends the work of many of the preceding authors. Analytical, numerical, and experimental techniques are introduced as follows.

Chapter 2 The formulation of the surface electric field integral equation (EFIE) is outlined. New analytical sheet impedance forms are provided for the inclusion of high contrast materials. Proper discretization of the EFIE is discussed and its limitations are outlined. The chapter concludes with a discussion of matrix compression methods (fast algorithms).

Chapter 3 A new form of redundancy minimization algorithm, a Multilevel Geometry Description (MLGD), is defined. Facet interactions are tracked using translation vectors and rotation matrices, ensuring only non-redundant operations are performed. Because of this multilevel approach, advanced hierarchical methods of forming bases that ensure current continuity between disjoint surfaces are introduced.

Chapter 4 The aforementioned incomplete Helmholtz decomposition is more efficiently defined via a mixed potential set of Current-Charge (CQ) sub-bases. Use of these sub-bases is shown to permit development of a new approach to matrix conditioning, termed the Multibasis (MB) method. The chapter concludes with an outline of the overall numerical implementation.

Chapter 5 The design and implementation of low frequency loop antennas, including discussions on electric field sensitivity and limitations on their use as sensors near complex media are included. Test and measurement issues specific to low frequency field measurements are also discussed and remedies are proposed.

Chapter 6 The numerical implementation of Chapters 2 through 4 is verified by theory and measurement. Efficiency, accuracy, and applicability of the simulation tool are demonstrated by comparison with measured data. Finally, selection of an improved LF tag placement location is made from simulated data, and computed field strength values are verified by measurement.

Chapter 7 The contributions of this work are reviewed and future research is discussed.

CHAPTER 2

Integral Equations and Fast Algorithms

The purpose of this chapter is to outline the path taken from Maxwell's equations to the formulation of an efficient integral equation solver for electrically small structures. In the following sections, volume equivalence forms are applied in contrast to the more common surface equivalence principle in derivation of the surface electric field integral equation (EFIE). Taking advantage of this approach, a set of equivalent sheet impedance approximate boundary conditions are derived and their application within the EFIE is outlined. Additional considerations particular to low frequency problems and the EFIE are then discussed and discretization of the integral equation is performed. Finally, existing matrix compression algorithms for accelerating iterative solution are discussed and adopted.

2.1 Time-Harmonic Electromagnetic Fields

The frequency response of electrically small structures is a smooth function. Thus, few frequency domain data points are needed to interpolate the response of these structures over many octaves of bandwidth. A transient response over this same bandwidth can be computed directly via a Fourier transform at minimal cost. For this reason, this work employs time-harmonic forms in the solution of such systems

at discrete frequencies. An exponential time harmonic dependence $e^{j\omega t}$ is assumed and suppressed throughout.

2.1.1 Maxwell's Equations and The Wave Equation

Governing all macroscopic electromagnetic phenomena discussed in this work, the time-harmonic Maxwell's equations in a homogeneous, isotropic region are [37, 38]

$$\nabla \times \mathbf{E} = -j\omega\mu\mathbf{H} - \mathbf{M} \quad (2.1)$$

$$\nabla \times \mathbf{H} = j\omega\epsilon\mathbf{E} + \mathbf{J} \quad (2.2)$$

$$\nabla \cdot \mathbf{E} = \frac{\rho_{ev}}{\epsilon} \quad (2.3)$$

$$\nabla \cdot \mathbf{H} = \frac{\rho_{mv}}{\mu}. \quad (2.4)$$

These coupled differential equations relate the vector electric and magnetic fields \mathbf{E} and \mathbf{H} to the volumetric quantities of electric current density \mathbf{J} , electric charge density ρ_{ev} , magnetic current density \mathbf{M} , and magnetic charge density ρ_{mv} . Both magnetic current and charge densities are fictitious quantities included to make the equations symmetric. Furthermore, frequency dependence is in the form of the radian frequency component $\omega = 2\pi f$, with f being the frequency of the time-harmonic fields and currents. The complex constitutive quantities μ and ϵ define the material permeability and permittivity, respectively. Both relations are decomposed into real and lossy (imaginary) components as $\mu = \mu' - j\mu'' = \mu_0\mu_r - j\mu''$ and $\epsilon = \epsilon' - j\epsilon'' = \epsilon_r\epsilon_0 - j\frac{\sigma_e}{\omega}$. μ_0 is the permeability of free space, ϵ_0 is the permittivity of free space, and σ_e is the electric conductivity of the medium. When these equations are combined with the

electric and magnetic field boundary (or jump) conditions [37]

$$\hat{n} \times (\mathbf{E}_2 - \mathbf{E}_1) = \mathbf{M}_s \quad (2.5)$$

$$\hat{n} \times (\mathbf{H}_2 - \mathbf{H}_1) = \mathbf{J}_s \quad (2.6)$$

$$\hat{n} \cdot (\epsilon_2 \mathbf{E}_2 - \epsilon_1 \mathbf{E}_1) = \rho_{es} \quad (2.7)$$

$$\hat{n} \cdot (\mu_2 \mathbf{H}_2 - \mu_1 \mathbf{H}_1) = \rho_{ms}, \quad (2.8)$$

solutions for the fields, currents, and charges in a piecewise inhomogeneous environment can be determined through solution of the resulting differential forms. (Above, the associated current and charge values along the boundary are surface densities, thus the s subscript.)

Separate equations for the electric and magnetic fields scattered by equivalent or impressed volumetric sources can be formed by substitution within (2.1), resulting in [37, 38]

$$\nabla \times \nabla \times \mathbf{E}^S - k^2 \mathbf{E}^S = -j\omega\mu \mathbf{J}_i - \nabla \times \mathbf{M}_i \quad (2.9)$$

$$\nabla \times \nabla \times \mathbf{H}^S - k^2 \mathbf{H}^S = -j\omega\epsilon \mathbf{M}_i + \nabla \times \mathbf{J}_i, \quad (2.10)$$

where $k = 2\pi/\lambda = \omega\sqrt{\mu\epsilon}$ is the wavenumber in the medium and \mathbf{J}_i and \mathbf{M}_i are impressed volumetric electric and magnetic current stimuli forcing these differential forms.

2.1.2 Volume Equivalence

Before these equations are applied, it is first necessary to discuss the approach taken to include material parameters in the numerical method.

Consider a material (defined by its constitutive relations μ, ϵ) in the presence of an impressed electric current \mathbf{J}_i . The total fields \mathbf{E}^T and \mathbf{H}^T within the medium must

satisfy

$$\nabla \times \mathbf{E}^T = -j\omega\mu\mathbf{H}^T \quad (2.11)$$

$$\nabla \times \mathbf{H}^T = j\omega\epsilon\mathbf{E}^T + \mathbf{J}_i. \quad (2.12)$$

If the same source is to radiate in the absence of this material, i.e. $\mu = \mu_0, \epsilon = \epsilon_0$, then by superposition only the background (incident) fields $\mathbf{E}^{\text{inc}}, \mathbf{H}^{\text{inc}}$ are present and satisfy

$$\nabla \times \mathbf{E}^{\text{inc}} = -j\omega\mu_0\mathbf{H}^{\text{inc}} \quad (2.13)$$

$$\nabla \times \mathbf{H}^{\text{inc}} = j\omega\epsilon_0\mathbf{E}^{\text{inc}} + \mathbf{J}_i. \quad (2.14)$$

Subtracting (2.13) from (2.11), and substituting

$$\mathbf{E}^s = \mathbf{E}^T - \mathbf{E}^{\text{inc}} \quad (2.15)$$

$$\mathbf{H}^s = \mathbf{H}^T - \mathbf{H}^{\text{inc}}, \quad (2.16)$$

a set of coupled differential equations for the scattered fields $\mathbf{E}^s, \mathbf{H}^s$ is developed

$$\nabla \times \mathbf{E}^s = -j\omega\mu_0\mathbf{H}^s - j\omega(\mu - \mu_0)\mathbf{H}^T = -j\omega\mu_0\mathbf{H}^s - \mathbf{M}_{\text{eq}} \quad (2.17)$$

$$\nabla \times \mathbf{H}^s = j\omega\epsilon_0\mathbf{E}^s + j\omega(\epsilon - \epsilon_0)\mathbf{E}^T = j\omega\epsilon_0\mathbf{E}^s + \mathbf{J}_{\text{eq}}. \quad (2.18)$$

Therein, volumetric equivalent currents

$$\mathbf{M}_{\text{eq}} = j\omega(\mu - \mu_0)\mathbf{H}^T \quad (2.19)$$

$$\mathbf{J}_{\text{eq}} = j\omega(\epsilon - \epsilon_0)\mathbf{E}^T \quad (2.20)$$

are defined, acting as equivalent polarization currents radiating in free space that

produce the same scattered fields as the original material (even for the case of a medium of finite extent) [37, 38]. As an extension of the forms above, if we look back at (2.19) and substitute (2.11), the curl of the magnetic equivalent current source within a homogeneous medium can be related directly to the electric equivalent current source

$$\begin{aligned}\nabla \times \mathbf{M}_{\text{eq}} &= j\omega(\mu - \mu_0) \nabla \times \mathbf{H}^T = (j\omega)^2 \epsilon(\mu - \mu_0) \mathbf{E}^T \\ &= j\omega\epsilon \frac{\mu - \mu_0}{\epsilon - \epsilon_0} \mathbf{J}_{\text{eq}}.\end{aligned}\tag{2.21}$$

Since this source radiates in free space it can be treated as the forcing function in the wave equation (2.9)

$$\begin{aligned}\nabla \times \nabla \times \mathbf{E}^s - k_0^2 \mathbf{E}^s &= -j\omega\mu_0 \mathbf{J}_{\text{eq}} - \nabla \times \mathbf{M}_{\text{eq}} \\ &= -j\omega\mu_0 \left(1 + \frac{-j\omega\epsilon}{-j\omega\mu_0} \frac{\mu - \mu_0}{\epsilon - \epsilon_0} \right) \mathbf{J}_{\text{eq}} \\ &= -j\omega\mu_0 \mathbf{J}'_{\text{eq}},\end{aligned}\tag{2.22}$$

with modified equivalent current

$$\begin{aligned}\mathbf{J}'_{\text{eq}} &= \left(1 + \frac{-j\omega\epsilon}{-j\omega\mu_0} \frac{\mu - \mu_0}{\epsilon - \epsilon_0} \right) \mathbf{J}_{\text{eq}} \\ &= \left(1 + \frac{\epsilon}{\mu_0} \frac{\mu - \mu_0}{\epsilon - \epsilon_0} \right) j\omega(\epsilon - \epsilon_0) \mathbf{E}^T \\ &= j\omega\epsilon \left(\frac{\mu}{\mu_0} - \frac{\epsilon_0}{\epsilon} \right) \mathbf{E}^T.\end{aligned}\tag{2.23}$$

It is evident that the introduction of a material medium is equivalent to the introduction of a set of currents radiating in free space whose value is dependent on the total field within the material.

2.1.3 Impedance Sheet Boundary Conditions

This work centers on the simulation of structures that are electrically thin at the frequency of interest, at least in terms of free-space wavelength. By application of the equivalent sources and boundary conditions above, a number of alternative sheet impedance boundary conditions are now derived for including such materials.

Thin Slab Average Boundary

The case of the one dimensional material slab is shown in figure 2.1(a) in the presence of an incident plane wave \mathbf{E}^{inc} and scattering forward and backward propagating waves, \mathbf{E}^{sB} and \mathbf{E}^{sF} , respectively. If this slab is assumed to be thin in terms of material wavelength, the average volumetric current distribution can be quite accurately represented via a sheet current $J_s = dJ_{V\text{avg}}$ [39], where d is the thickness of the slab, and $J_{V\text{avg}}$ is the average volumetric current within the slab (assumed to vary only as a function of depth). By application of the modified equivalent current (2.23), the average current in a thin slab is

$$\begin{aligned} J_{V\text{avg}} &= \frac{1}{d} \int_0^d J_V(z) dz \\ &= j\omega\epsilon \left(\frac{\frac{\mu}{\mu_0} - \epsilon_0}{\epsilon} \right) \frac{1}{d} \int_0^d E^T(z) dz \\ &= j\omega\epsilon \left(\frac{\mu}{\mu_0} - \frac{\epsilon_0}{\epsilon} \right) E_{\text{avg}}. \end{aligned} \quad (2.24)$$

The average electric field in the medium, E_{avg} , to the tangential electric field at the first surface boundary, $E(0)$, then we have a relation between the sheet current and the tangential field at the boundary. This relationship can be formed in terms of a zeroth order equivalent sheet impedance Z_{sh}^0 ,

$$E(0) = Z_{sh}^0 J_s = Z_{sh}^0 J_{V\text{avg}} d, \quad (2.25)$$

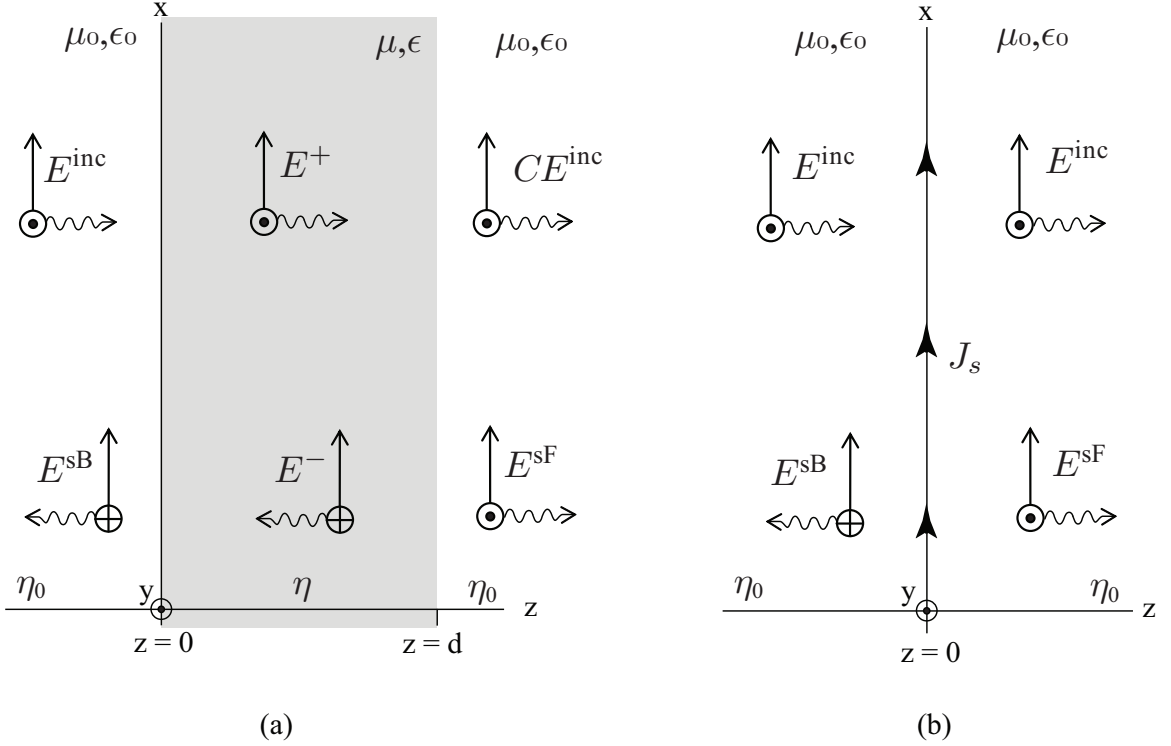


Figure 2.1: Homogeneous slab and sheet current boundary. (a) Homogeneous slab in a propagating wave. (b) Sheet current in a propagating wave.

where

$$Z_{sh}^0 = \frac{E(0)}{J_{V_{avg}} d} = \frac{1}{j\omega\epsilon\left(\frac{\mu}{\mu_0} - \frac{\epsilon_0}{\epsilon}\right) d} = \frac{\eta_2}{j\gamma_2\left(\frac{\mu}{\mu_0} - \frac{\epsilon_0}{\epsilon}\right) d}. \quad (2.26)$$

If we assume $\mu = \mu_0$, then this form is equivalent to that derived using the volume equivalent current (2.19). Furthermore, for a highly conductive non-magnetic material with $\epsilon'' \gg \epsilon'$ this form is equal to that of a resistive sheet impedance, $Z_{sh} = 1/(\sigma_e d)$ [40].

Thick Slab Average Boundary

Above it was assumed that the electrical thickness of the slab in terms of material wavelengths was negligible. While this is the case for a number of thin dielectric materials, it is not the case of most metallic and magnetic media. For these materials

interior moding must be considered in the derivation of an impedance boundary equivalent form.

However, it is first necessary to discuss the notions of incident and scattered wave impedances, η_{inc} and η_{s} , for a material interface at low frequencies. When solving for the electric field coefficients interior and exterior to an impedance slab, it is assumed that the ratio between the electric and magnetic fields in a given medium are related only to the constituent quantities of each medium. However, the ratio between these fields in the near field region depends not only on the constitutive relations but also on the distance from the source to the observation point and the source current distribution [41]. The ratio of incident tangential electric to magnetic field, $\eta_{\text{inc}} = E^{\text{inc}}(0)/H^{\text{inc}}(0) \neq \eta_0$ can be computed along with the excitation (so long as both electric and magnetic field excitation values are known). However, the ratio between the tangential electric and magnetic backward and forward scattered fields, $\eta_{\text{s}} = E^{\text{sB}}(0)/H^{\text{sB}}(0) = E^{\text{sF}}(0)/H^{\text{sF}}(0)$, is not known a-priori. In the following derivations it is assumed that the scattered wave impedance is equal to that of the incident wave impedance at the interface, $\eta_{\text{s}} = \eta_{\text{inc}}$.

Even for the near field case, fields impressed at the slab boundaries shown in figure 2.1 will be linearly related though they cannot be regarded as a translation of a transverse electromagnetic (TEM) wave. This relation is $E^{\text{inc}}(d) = CE^{\text{inc}}(0)$, where C is the complex ratio between the advancing incident field at the primary interface, $E^{\text{inc}}(0)$, and the same field at the secondary interface, $E^{\text{inc}}(d)$. Furthermore, for an electrically thick material slab (in terms of its complex wavenumber $\gamma = j\omega\sqrt{\mu\epsilon}$) a superposition of forward and backward traveling plane waves is assumed for the field distribution within the slab [39],

$$E(z) = E^+ e^{-\gamma z} + E^- e^{\gamma z}. \quad (2.27)$$

By application of the tangential field boundary conditions and the field impedance ratios for the incident, scattered, and interior fields, the interior and scattered field coefficients are related via the algebraic matrix equation [42]

$$\begin{bmatrix} E^{\text{inc}}(0) \\ E^{\text{inc}}(0) \\ CE^{\text{inc}}(0) \\ CE^{\text{inc}}(0) \end{bmatrix} = \begin{bmatrix} 1 & 1 & -1 & 0 \\ Z_{12} & -Z_{12} & 1 & 0 \\ T & T^{-1} & 0 & -1 \\ Z_{12}T & -Z_{12}T^{-1} & 0 & -1 \end{bmatrix} \begin{bmatrix} E^+ \\ E^- \\ E^{\text{s}}(0) \\ E^{\text{s}}(d) \end{bmatrix}. \quad (2.28)$$

Solving this system gives the interior field coefficients

$$E^+ = \frac{(1 + \Gamma)}{1 - \Gamma^2 T^2} E^{\text{inc}}(0) \quad (2.29)$$

$$E^- = -\frac{(1 + \Gamma) T^2 \Gamma}{1 - \Gamma^2 T^2} E^{\text{inc}}(0) \quad (2.30)$$

and relative scattered parameters

$$S_{11} = \frac{E^{\text{sB}}}{E^{\text{inc}}(0)} = \frac{(1 - T^2) \Gamma}{1 - \Gamma^2 T^2} \quad (2.31)$$

$$S_{21} - 1 = \frac{E^{\text{sF}}}{E^{\text{inc}}(0)} = \frac{C(T^2 \Gamma^2 - 1) + T(1 - \Gamma^2)}{1 - \Gamma^2 T^2} \quad (2.32)$$

in terms of the incident field at the primary interface. The first surface reflection coefficient is defined as

$$\Gamma = \frac{\eta_m - \eta_{\text{inc}}}{\eta_m + \eta_{\text{inc}}}, \quad (2.33)$$

with impedance of the material layer $\eta_m = \sqrt{\mu/\epsilon}$, and the phase variation within that layer $T = e^{-\gamma d}$. $Z_{12} = \eta_m/\eta_{\text{inc}}$ is the relative material impedance, d is the thickness of the material layer and E^{sB} is the magnitude of the backward scattered field at the $z = 0$ interface. E^{sF} is the magnitude of the forward scattered field at the $z = d$ interface. It is important to note that assuming a forward propagating incident field

implies the backward scattered field E^{sB} and the fields interior to the slab, E^+ and E^- , are not influenced by variation in the field value at the backside of the interface, $CE^{\text{inc}}(0)$.

To determine an average thick sheet boundary condition, the electric field as a function of depth within the slab is first formulated

$$E(z) = \frac{(1 + \Gamma)(e^{-\gamma z} - \Gamma T^2 e^{\gamma z})}{1 - \Gamma^2 T^2} E^{\text{inc}}(0); \quad 0 < z < d. \quad (2.34)$$

Next, the incident field at the primary interface, $E^{\text{inc}}(0)$, is related to the total field at the primary boundary, $E(0)$, via

$$E(0) = E^{\text{inc}}(0) + E^{\text{sB}} = \frac{(1 + \Gamma)(1 - T^2 \Gamma)}{1 - \Gamma^2 T^2} E^{\text{inc}}(0), \quad (2.35)$$

resulting in

$$\begin{aligned} E(z) &= \frac{(1 + \Gamma)(e^{-\gamma z} - \Gamma T^2 e^{\gamma z})}{1 - \Gamma^2 T^2} \frac{1 - \Gamma^2 T^2}{(1 + \Gamma)(1 - T^2 \Gamma)} E(0) \\ &= \frac{(e^{-\gamma z} - \Gamma T^2 e^{\gamma z})}{(1 - T^2 \Gamma)} E(0); \quad 0 < z < d, \end{aligned} \quad (2.36)$$

an expression for the field within the medium in terms of the total field at the primary interface. Following the same procedure used for the thin sheet, the average electric field in the slab becomes

$$E_{\text{avg}} = \frac{1}{d} \int_0^d E(z) dz = \frac{E(0)(1 - T)(1 - \Gamma T)}{\gamma d (1 - T^2 \Gamma)} \quad (2.37)$$

and the average first order equivalent sheet Z_{sh}^1 impedance

$$\begin{aligned} Z_{sh}^1 &= \frac{E(0)}{J_{V_{\text{avg}}} d} = Z_{sh}^0 \frac{(\gamma d)(1 - T^2 \Gamma)}{(1 - \Gamma T)(1 - T)} \\ &= \frac{\eta}{j \left(\frac{\mu}{\mu_0} - \frac{\epsilon_0}{\epsilon} \right)} \frac{(1 - T^2 \Gamma)}{(1 - \Gamma T)(1 - T)}, \end{aligned} \quad (2.38)$$

where choosing $\mu = \mu_0$ again gives the standard volume equivalent form.

Thick Slab Equivalent Boundary

While the preceding formulations have relied on the application of an average boundary condition, the following derivation takes a different approach. For an infinite electric sheet current J_s residing in free space (as in figure 2.1(b)), the sheet impedance boundary relation [40]

$$E^{\text{inc}}(0) + E^{\text{sB}} + E^{\text{inc}}(0) + E^{\text{sF}} = 2Z_{\text{sh}} J_s, \quad (2.39)$$

can be used to solve for the scattered field coefficients in terms of the scattering parameters

$$S_{11} = \frac{E^{\text{sB}}}{E^{\text{inc}}(0)} = \frac{-\eta_{\text{inc}}}{2Z_{\text{sh}} + \eta_{\text{inc}}} \quad (2.40)$$

$$S_{21} - 1 = \frac{E^{\text{sF}}}{E^{\text{inc}}(0)} = \frac{-\eta_{\text{inc}}}{2Z_{\text{sh}} + \eta_{\text{inc}}} \quad (2.41)$$

where $\eta_s = \eta_{\text{inc}}$ is assumed. Solving for the equivalent sheet impedance values in terms of these material scattering parameter gives

$$Z_{sh}^{\text{B}} = \frac{-\eta_{\text{inc}}}{2} \frac{1 + S_{11}}{S_{11}} \quad (2.42)$$

$$Z_{sh}^{\text{F}} = \frac{\eta_{\text{inc}}}{2} \frac{S_{21}}{1 - S_{21}}, \quad (2.43)$$

where Z_{sh}^B is the equivalent sheet impedance to produce the proper backward scattered field and Z_{sh}^F is the equivalent sheet impedance necessary to produce the proper forward scattered field.

Now consider the existing system as two disjoint problems. First, if there are no other scattering objects to the right of the boundary, a scattering object to the left of this sheet interacts only with the backscattered field, and thus the equivalent sheet impedance Z_{sh}^B as shown in figure 2.2(a). Second, any scattering object to the right of such a sheet (figure. 2.2(b)) would have impressed upon it a superposition of the forward scattered field E^{sF} and the incident field E_{inc} . However, as before, mutual interaction between the sheet and the scattering object occurs in terms of Z_{sh}^B . For these two disjoint problems to merge into a single, generally applicable open surface equivalent sheet impedance, like that of figure 2.2(c), the backscattered and forward scattered sheet impedances should be equivalent.

Propagating Equivalent Boundary Condition If we assume that the material slab is sufficiently thin such that $C \sim 1$, then applying the scattering parameters of (2.49) to the forward and backward scattering sheet impedances of (2.40) gives

$$Z_{sh}^B = \frac{\eta(1+\Gamma)(T^2\Gamma-1)}{2\Gamma(1-T^2)} = \frac{\eta(1+\Gamma)(T^2\Gamma-1)}{2(1-T)\Gamma(1+T)} \quad (2.44)$$

$$Z_{sh}^F = \frac{\eta T(1-\Gamma^2)}{2(1-T)(1+T\Gamma^2)} = \frac{\eta(1+\Gamma)T(1-\Gamma)}{2(1-T)(1+T\Gamma^2)}. \quad (2.45)$$

Non-propagating Equivalent Boundary Condition The derivation in the preceding paragraph assumes that the material medium is excited by a propagating wave. At very low frequencies the assumption that the impressed field is propagating is not necessarily correct. The near-field excitation might alternatively be better represented as the superposition of two waves traveling in opposite directions as depicted in figure 2.3.

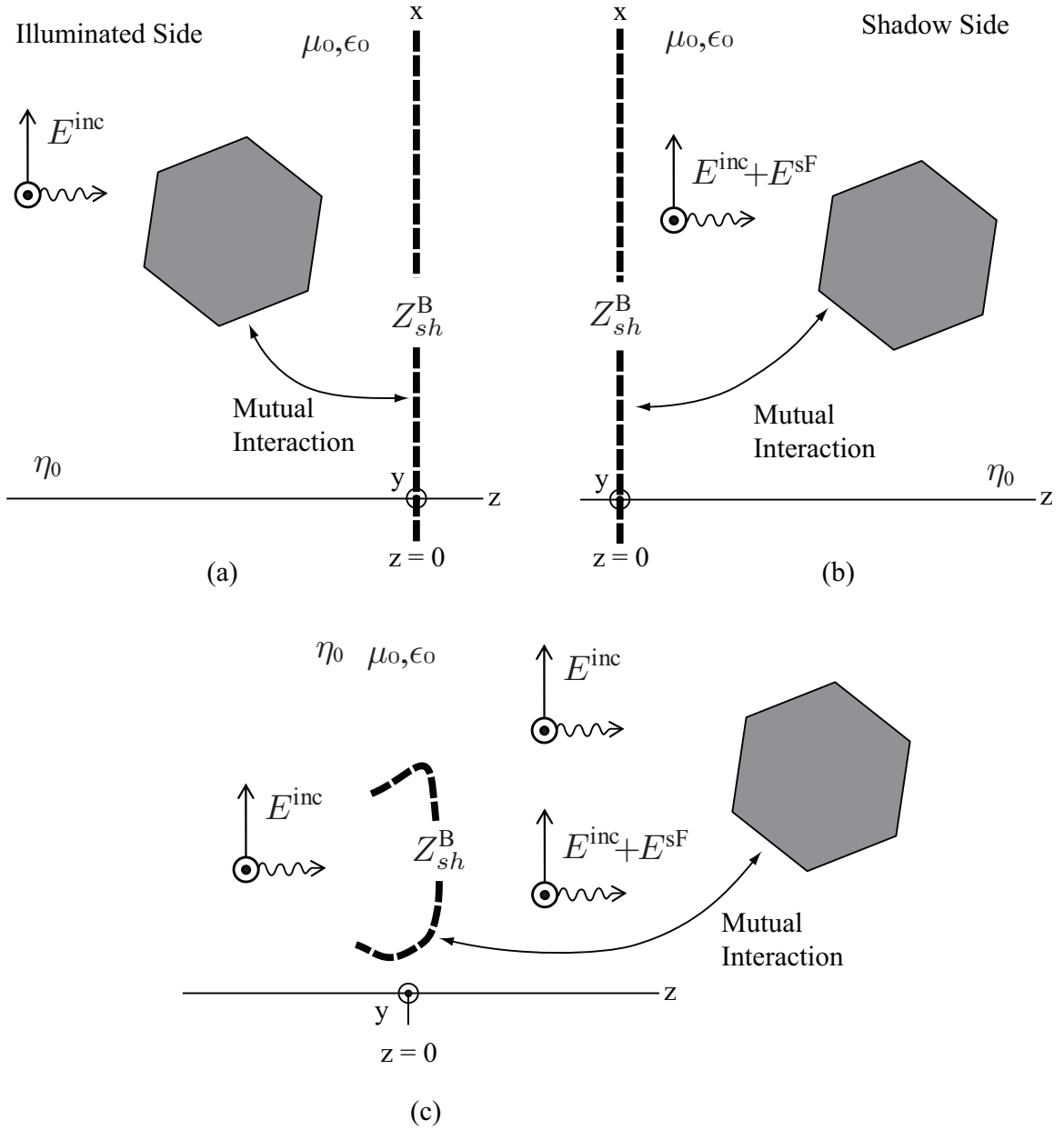


Figure 2.2: Forward and backward sheet equivalent problems. (a) Backward equivalent interaction. (b) Forward equivalent interaction. (c) Open surface equivalent, valid when $Z_{sh}^B = Z_{sh}^F$.

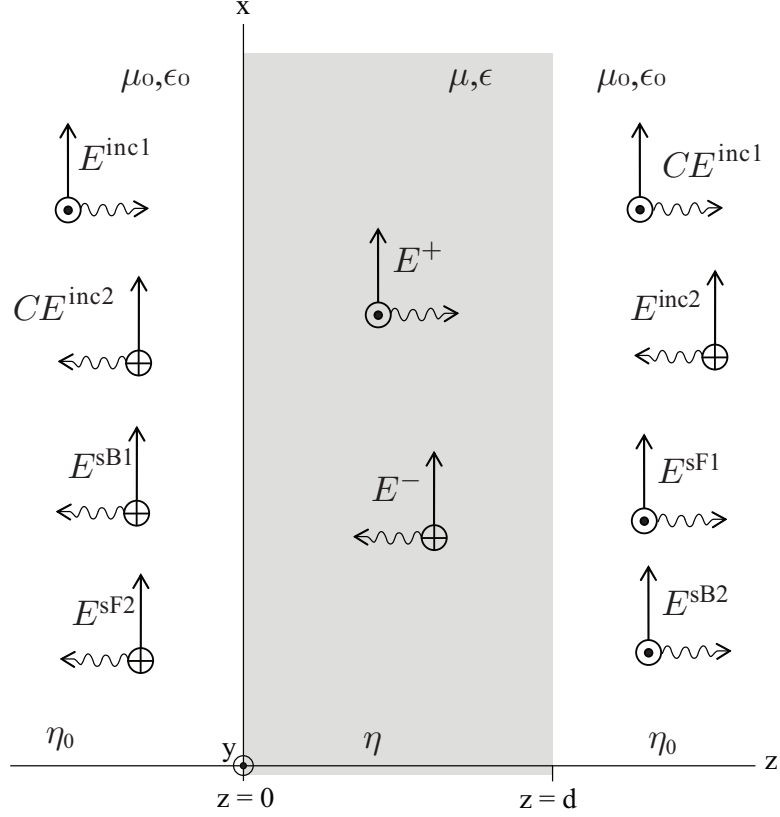


Figure 2.3: Diagram of a thick slab immersed in a standing wave.

This system requires the solution of the matrix equation

$$\begin{bmatrix} \frac{E^{\text{inc}}(0)}{2} + \frac{E^{\text{inc}}(0)}{2} \\ \frac{E^{\text{inc}}(0)}{2} - \frac{E^{\text{inc}}(0)}{2} \\ \left(\frac{CE^{\text{inc}}(0)}{2} + \frac{E^{\text{inc}}(0)}{2} \right) \\ \left(\frac{E^{\text{inc}}(0)}{2} - \frac{CE^{\text{inc}}(0)}{2} \right) \end{bmatrix} = \begin{bmatrix} 1 & 1 & -1 & 0 \\ Z_{12} & -Z_{12} & 1 & 0 \\ T & T^{-1} & 0 & -1 \\ Z_{12}T & -Z_{12}T^{-1} & 0 & -1 \end{bmatrix} \begin{bmatrix} E^+ \\ E^- \\ E^{\text{s}}(0) \\ E^{\text{s}}(d) \end{bmatrix}, \quad (2.46)$$

where $E^{\text{inc}1} = E^{\text{inc}2} = E^{\text{inc}}$ is assumed. The resulting interior field coefficients are

$$E^+ = \frac{(1 + \Gamma)(1 - CT\Gamma)}{2(1 - \Gamma^2 T^2)} E^{\text{inc}}(0) \quad (2.47)$$

$$E^- = \frac{T(1 + \Gamma)(C - T\Gamma)}{2(1 - \Gamma^2 T^2)} E^{\text{inc}}(0), \quad (2.48)$$

and the reflected and transmitted scattering parameters are

$$S_{11} = \frac{E^s(0)}{E^{\text{inc}}(0)} = \frac{(\Gamma - 1)(1 - T(C + C\Gamma - T\Gamma))}{2(1 - \Gamma^2 T^2)} \quad (2.49)$$

$$S_{21} - 1 = \frac{E^s(d)}{E^{\text{inc}}(0)} = \frac{(T - 1)(1 + T\Gamma^2 - C\Gamma(1 + T))}{2(1 - \Gamma^2 T^2)}. \quad (2.50)$$

If the material is electrically thin in terms of the exterior wavelength such that the magnitude of the impressed standing wave is nearly equivalent on both sides of the slab, then $C \sim 1$ and the scattering parameters become

$$S_{11} = \frac{(1 - T)(\Gamma - 1)}{2(1 + T\Gamma)} \quad (2.51)$$

$$S_{21} = \frac{(1 + T)(1 + \Gamma)}{2(1 + T\Gamma)}. \quad (2.52)$$

Applying the sheet current boundary conditions just described, the equivalent forward and backward scattering impedances are

$$Z_{sh}^B = \frac{-\eta_{\text{inc}}}{2} \frac{1 + S_{11}}{S_{11}} = \frac{\eta_{\text{inc}}(1 + T)(1 + \Gamma)}{2(1 - T)(1 - \Gamma)} \quad (2.53)$$

$$Z_{sh}^F = \frac{\eta_{\text{inc}}}{2} \frac{S_{21}}{1 - S_{21}} = \frac{\eta_{\text{inc}}(1 + T)(1 + \Gamma)}{2(1 - T)(1 - \Gamma)}. \quad (2.54)$$

or equivalently

$$Z_{sh}^{\text{NP}} = Z_{sh}^{\text{B,F}} = \frac{\eta_m(1 + T)}{2(1 - T)}. \quad (2.55)$$

Thus, the forward and backward scattering sheet impedances for a material slab placed in a standing wave are equal and are independent of the wave impedance of the incident (or scattered) field. A material whose interior electrical length causes $T \rightarrow 1$, has a sheet impedance $Z_{sh}^{\text{NP}} \rightarrow \infty$ and the material becomes transparent. Alternatively, for a thick lossy material $T \rightarrow 0$ and $Z_{sh}^{\text{NP}} \rightarrow \eta_m/2$.

2.2 Integral Equation Discretization

As discussed in the introduction, the use of a differential equation based numerical solver would require a volumetric discretization of the 3D structures of interest. Alternatively, to reduce the dimensionality of the problem, decrease numerical error, and improve stability, an integral equation formulation based on equivalent surface currents can be adopted. This section outlines just such an alternative formulation and discusses its application to solving the problems at hand.

2.2.1 Volume & Surface Integral Equations

The integral equation equivalent of the differential electric field wave equation in (2.9) is derived by application of the second vector dyadic Green's theorem

$$\begin{aligned} & \int_V [\mathbf{P} \cdot \nabla \times \nabla \times \overline{\mathbf{Q}} - (\nabla \times \nabla \times \mathbf{P}) \cdot \overline{\mathbf{Q}}] dv \\ & = - \oint_S [\mathbf{P} \times \nabla \times \overline{\mathbf{Q}} + (\nabla \times \mathbf{P}) \times \overline{\mathbf{Q}}] \cdot \mathbf{ds}, \end{aligned} \quad (2.56)$$

given knowledge of the Dyadic Green's function,

$$\overline{\mathbf{G}}(\mathbf{r}', \mathbf{r}) = \left(\overline{\mathbf{I}} + \frac{\nabla \nabla}{k^2} \right) g(\mathbf{r}', \mathbf{r}), \quad (2.57)$$

that satisfies the corresponding Helmholtz wave equation

$$\nabla \times \nabla \times \overline{\mathbf{G}}(\mathbf{r}', \mathbf{r}) - k^2 \overline{\mathbf{G}}(\mathbf{r}', \mathbf{r}) = \overline{\mathbf{I}} \delta(\mathbf{r} - \mathbf{r}'). \quad (2.58)$$

By substituting $\mathbf{P} = \mathbf{E}^s(\mathbf{r})$ and $\overline{\mathbf{Q}} = \overline{\mathbf{G}}(\mathbf{r}', \mathbf{r})$ into (2.22), and applying (2.58) in conjunction with a number of tensor identities [43], we arrive at the following integral

form

$$\begin{aligned}
\mathbf{E}^s(\mathbf{r}') - j\omega\mu \int_V \mathbf{J}'_{\text{eq}}(\mathbf{r}') \cdot \overline{\mathbf{G}}(\mathbf{r}', \mathbf{r}) \, dv \\
= - \oint_S [\mathbf{E}(\mathbf{r}) \times \nabla \times \overline{\mathbf{G}}(\mathbf{r}', \mathbf{r}) + (\nabla \times \mathbf{E}(\mathbf{r})) \times \overline{\mathbf{G}}(\mathbf{r}', \mathbf{r})] \cdot d\mathbf{s}. \quad (2.59)
\end{aligned}$$

As discussed in the previous section, all media is to be replaced by equivalent sources in this implementation. The closed surface integral in this equation applies to the surface at infinity which, via the radiation condition [38, 42], has zero contribution. Unlike formulations representing homogeneous materials in terms of equivalent surface currents via Huygen's principle [37], this work employs approximations to the volume equivalence of thin materials.

The total field in space, after application of the chain rule [44] and recognition that the currents in question do not flow normal to the surface, takes the form

$$\begin{aligned}
\mathbf{E}^T(\mathbf{r}) &= \mathbf{E}^{\text{inc}}(\mathbf{r}) - j\omega\mu_0 \int_S \overline{\mathbf{G}}(\mathbf{r}', \mathbf{r}) \cdot \mathbf{J}'_{\text{eq}}(\mathbf{r}') \, ds' \\
&= \mathbf{E}^{\text{inc}}(\mathbf{r}) - j\frac{\eta}{k} \left[k^2 \int_S \mathbf{J}'_{\text{eq}}(\mathbf{r}') g(\mathbf{r}', \mathbf{r}) \, ds' - \int_S \nabla' \nabla g(\mathbf{r}', \mathbf{r}) \cdot \mathbf{J}'_{\text{eq}}(\mathbf{r}') \, ds' \right] \\
&= \mathbf{E}^{\text{inc}}(\mathbf{r}) - j\frac{\eta}{k} \left[k^2 \int_S \mathbf{J}'_{\text{eq}}(\mathbf{r}') g(\mathbf{r}', \mathbf{r}) \, ds' - \int_S (\nabla' \cdot \mathbf{J}'_{\text{eq}}(\mathbf{r}')) \nabla g(\mathbf{r}', \mathbf{r}) \, ds' \right]. \quad (2.60)
\end{aligned}$$

Therein, different materials are introduced through application of the sheet impedance forms outlined earlier. While this approach may not be desirable for electrically thick dielectric or low loss materials, it is very much applicable to the solution of general problems when material thicknesses are significantly smaller than the free space wavelength.

2.2.2 Integral Equation Discretization

When subjected to electromagnetic excitation, unique distributions of fields, currents, and charges result within and surrounding an object. Quantitative analysis of these distributions allows the engineer to simplify the complex system so that it can be manipulated to serve a given purpose.

Unfortunately, many objects do not lend themselves to analytical solution of the above integral forms, and a numerical approach becomes necessary. In the numerical method, the unknown distributions are approximated by expansion functions, their interactions are computed over these domains, and finally the boundary conditions are enforced. In this work such is performed by application of the Galerkin (or weighted residual) method using the inner product

$$\langle \mathbf{\Lambda}_m, \mathbf{\Lambda}_n \rangle = \int_{S_m} \mathbf{\Lambda}'_m \cdot \mathbf{\Lambda}_n ds', \quad (2.61)$$

where $\mathbf{\Lambda}_n$ is the vector expansion function and $\mathbf{\Lambda}_m$ is an identical test function. This product is applied to the integral equation

$$\begin{aligned} j \frac{k}{\eta} \int_{S_m} \mathbf{\Lambda}_m \cdot \mathbf{E}^B ds &= j \frac{k}{\eta} \int_{S_m} \mathbf{\Lambda}_m \cdot \mathbf{E}^{\text{inc}} ds - \int_{S_m} \int_{S_n} (k^2 \mathbf{\Lambda}_m \cdot \mathbf{J}_s g(\mathbf{r}', \mathbf{r})) ds ds' \\ &\quad + \int_{S_m} \int_{S_n} [\nabla' \cdot \mathbf{J}_s] (\mathbf{\Lambda}_m \cdot \nabla g(\mathbf{r}', \mathbf{r})) ds ds' \\ &= j \frac{k}{\eta} \int_{S_m} \mathbf{\Lambda}_m \cdot \mathbf{E}^{\text{inc}} ds - \int_{S_m} \int_{S_n} (k^2 \mathbf{\Lambda}_m \cdot \mathbf{J}_s g(\mathbf{r}', \mathbf{r})) ds ds' \\ &\quad + \int_{S_m} \int_{S_n} (\nabla' \cdot \mathbf{J}_s) g(\mathbf{r}', \mathbf{r}) (\nabla \cdot \mathbf{\Lambda}_m) ds ds' \quad (2.62) \end{aligned}$$

where the gradient is passed from the Green's function to the testing function via [45]. \mathbf{E}^B is \mathbf{E}^T evaluated at the boundary where the inner product enforces tangential

equivalence. Next, \mathbf{J}'_{eq} is expanded in terms of subdomain basis functions Λ_n

$$\mathbf{J}'_{\text{eq}} = \sum_n I_n \Lambda_n. \quad (2.63)$$

The final discretized form of the integral equation becomes

$$\begin{aligned} -j\frac{k}{\eta} \sum_m \int_{S_m} \Lambda_m \cdot \mathbf{E}^{\text{inc}} + j\frac{k}{\eta} \sum_m \int_{S_m} \Lambda_m \cdot \mathbf{E}^{\text{B}} \\ = k^2 \sum_m \sum_n \left[\int_{S_m} \int_{S_n} (\Lambda_m \cdot \Lambda_n) g(\mathbf{r}', \mathbf{r}) ds ds \right] I_n \\ - \sum_m \sum_n \left[\int_{S_m} \int_{S_n} (\nabla' \cdot \Lambda_n) g(\mathbf{r}', \mathbf{r}) (\nabla \cdot \Lambda_m) ds ds \right] I_n, \end{aligned} \quad (2.64)$$

or

$$-j\frac{k}{\eta} \mathbf{V}_m^{\text{inc}} = -j\frac{k}{\eta} \overline{\mathbf{Z}}_{sh} \mathbf{I}_n + \left[k^2 \overline{\mathbf{Z}}_{mn}^A - \overline{\mathbf{Z}}_{mn}^\phi \right] \mathbf{I}_n = \overline{\mathbf{Z}}_{mn} \mathbf{I}_n \quad (2.65)$$

in matrix notation. Therein $\mathbf{V}_m^{\text{inc}}$ is the potential due to the incident field, $\overline{\mathbf{Z}}_{sh}$ is the matrix relating the sheet impedance boundary condition, $\overline{\mathbf{Z}}_{mn}^A$ is the matrix of magnetic vector potential interactions, $\overline{\mathbf{Z}}_{mn}^\phi$ is the matrix of scalar potential interactions, and \mathbf{I}_n the vector of unknown current amplitudes. Since the singularity of the integrand has been passed to the testing and basis functions, this system of equations now demonstrates only a $1/R$ singularity and can easily be evaluated. In the present work the singularity subtraction and analytical treatment of [46] is applied.

Issues with the EFIE

The EFIE formulated above suffers from two well known drawbacks.

The first drawback is the problem of interior resonance, where the EFIE kernel has a nontrivial solution at the eigenvalues of a given interior problem [34, 47]. When simulating a closed cavity at the frequencies corresponding to resonant modes, more than a single solution may exist that satisfies the boundary conditions. When this

occurs the matrix equation becomes singular as the solution sought is non-unique. The structures of interest in this work are not only generally open (i.e. do not have significant interior dimension), but for those instances where cavities do exist the structures are excited at frequencies well below the first resonant mode. Thus, the problem of interior resonance breakdown of the EFIE is not of particular concern in this work.

The second well known drawback to the use of the electric field integral equation occurs when using a high mesh granularity relative to the simulation wavelength. This breakdown (which is not limited to low frequencies) arises due to the limitations of numerical precision [26, 34]. For a very fine mesh, or any mesh in a very low frequency field, contribution from the magnetic vector potential terms, $\bar{\mathbf{Z}}^A$, are much smaller than the electric scalar potential contributions, $\bar{\mathbf{Z}}^\phi$. The resulting magnetic vector potential contributions are less accurate (or may be lost altogether) and the remaining scalar potential contributions relate only to $\nabla_s \cdot \mathbf{J}$, via the Lorentz gauge. Since the divergence of a vector field is not sufficient to determine the field in its entirety (per Helmholtz's Theorem [48]), the numerical method can diverge or arrive at an incorrect solution. For multi-scale problems whose geometric features range over orders of magnitude, the issue manifests itself by increasing the condition number of the system [34].

To remedy the situation, it is necessary to scale the solenoidal and irrotational subspaces separately. This is implemented through application of separate curl and divergence conforming expansion functions that approximate a Helmholtz decomposition.

Expansion Functions

In this work a triangular surface discretization is employed. The most popular and quite possibly best understood vector expansion functions for such are the RWG

bases. While these bases are sometimes employed in this work, it is advantageous to begin with a more rudimentary function set. From this set, solenoidal and quasi-irrotational expansions can be simply introduced through sparse mappings at minimal cost.

Single Patch Expansion Functions The lowest level set of expansion functions used in this work are divergence conforming single patch (SP) expansions, denoted here by Λ_e^p . p denotes the patch index and e denotes the edge index. When applied to a triangular patch discretization, the vector surface current \mathbf{J}^p is defined to be

$$\mathbf{J}^p = \sum_{e=1}^3 \Lambda_e^p I_e. \quad (2.66)$$

and the total charge on the patch is related to the divergence of the surface current

$$\nabla \cdot \mathbf{J}^p = \nabla \cdot \Lambda_e^p I_e. \quad (2.67)$$

Therein, the SP expansion set and its divergence are defined to be

$$\Lambda_e^p(\mathbf{r}') = \begin{cases} \frac{\boldsymbol{\rho}_e^p(\mathbf{r}')}{2A} & \mathbf{r}' \in T_p \\ 0 & \mathbf{r}' \notin T_p \end{cases} \quad (2.68)$$

$$\nabla \cdot \Lambda_e^p(\mathbf{r}') = \frac{1}{2A}. \quad (2.69)$$

where A is the area of the patch, and $\boldsymbol{\rho}_e$ is a radial vector from the e^{th} node toward the e^{th} edge. The set of three single patch expansions that exist on any given triangle are shown in figure 2.4(a). These expansions are equivalent to 1/2 of the well known RWG expansion functions [23] without inclusion of edge length. The interaction between two patches is also shown to require 10 values in figure 2.4(b), one scalar term for the divergence of the expansion and 9 vector terms, one for each pair of

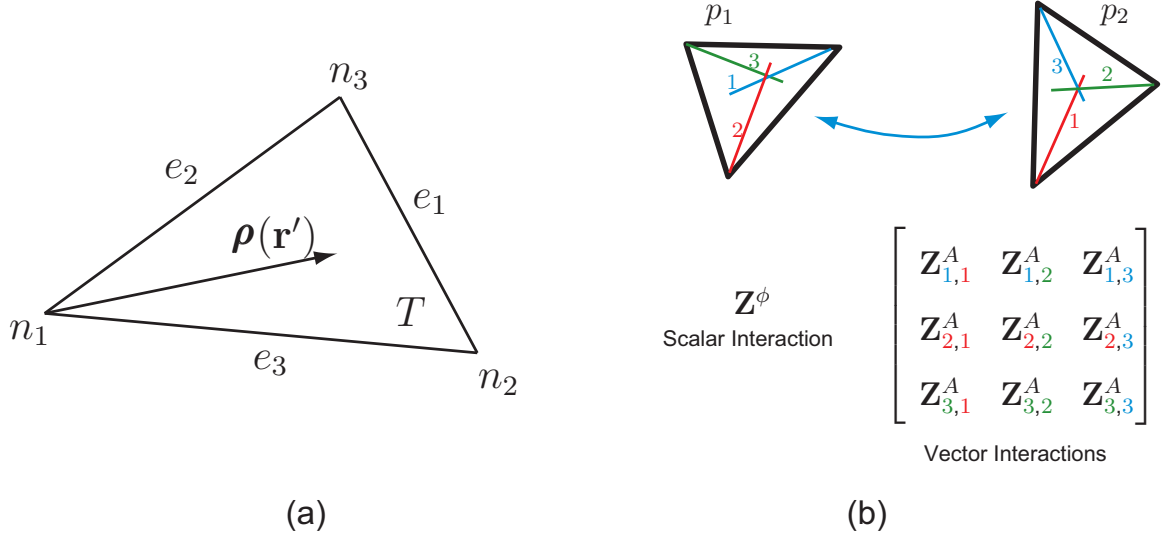


Figure 2.4: Single Patch (SP) expansion function. (a) Definition. (b) Interaction.

vector expansions.

Non-Solenoidal (Divergence Conforming) Bases While coefficients applied to the SP bases above can properly represent a complete current distribution, the SP expansions do not enforce patch current continuity. One option to ensure continuity is to employ pairs of SP expansions at common edges, resulting in RWG rooftop bases in figure 2.5(a), defined as

$$\Lambda_n^{\text{RWG}} = \begin{cases} \Lambda_{e_a}^a, & \mathbf{r}, p = 1 \\ -\Lambda_{e_b}^b, & \mathbf{r}, p = 2, \end{cases} \quad (2.70)$$

where e_a and e_b are local patch indices corresponding to the n^{th} mesh edge. When employed, the number of non-boundary edges (NBe's) is equal to the degrees of freedom (DOF) in the discretized system.

As mentioned, the EFIE requires that curl-conforming (loop) bases be employed and scaling be applied for a fine granularity mesh. In a system where the excitation is not entirely solenoidal, charge can accumulate and it is necessary to employ

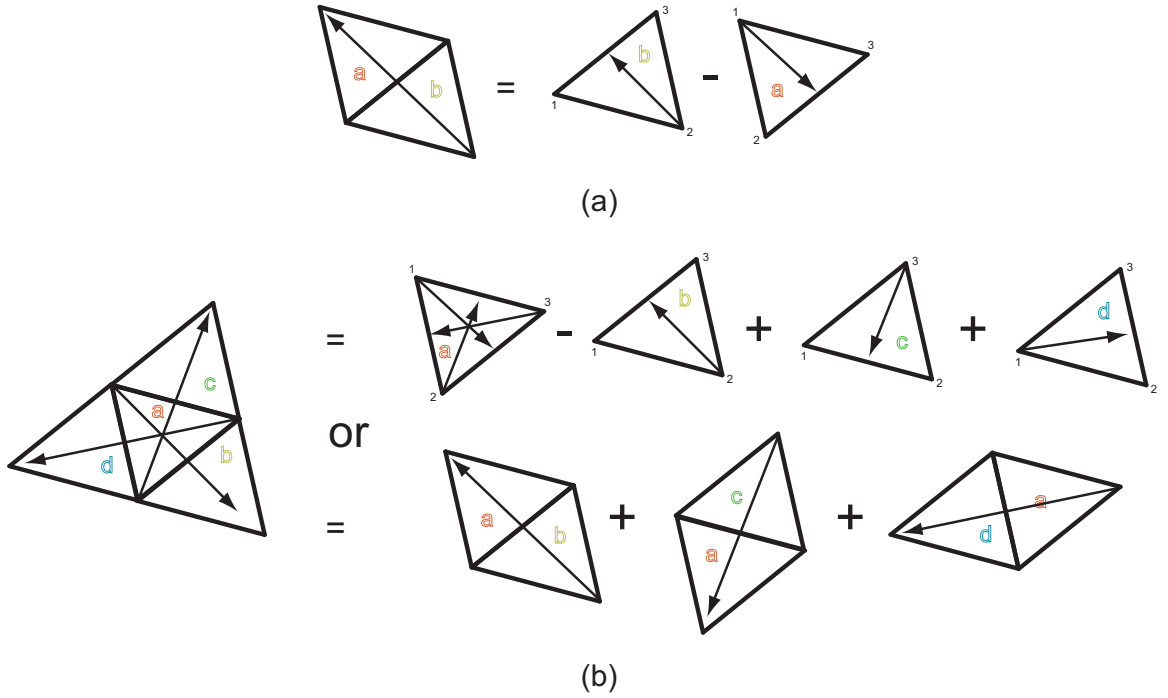


Figure 2.5: Divergence conforming expansion functions. (a) RWG basis formed from two SP bases. (b) Star basis formed from SP and RWG bases. (c) RWG, Tree, and Star bases on a surface discretization.

both solenoidal and non-solenoidal expansions. The divergence conforming expansions used are typically Tree and Star expansions. Tree expansions are a subset of the RWG expansions chosen not to form circulating currents. Alternative Star bases are equivalent to the summation of all RWG bases exiting a given triangle, as shown in figure 2.5(b) and may also be mapped via the superposition of a set of SP bases. To maintain a consistent number of DOF, the number of star and tree functions is one fewer than the number of patches (triangles) on the surface. Tree and star bases are always used in conjunction with the Loop bases, forming Loop-Tree (LT) and Loop-Star (LS) expansions of the surface current.

Solenoidal (Curl Conforming) Bases While complete divergence conforming expansion sets (e.g. RWG bases) work well at higher frequencies, fine meshes require the inclusion of curl-conforming expansions. By taking the difference between SP

bases on a given patch an alternative curl-conforming SP expansion is formed (see figure 2.6(a)). This curl conforming SP set is still incomplete (as it cannot enforce current continuity between patches). To enforce continuity, curl-conforming Loop

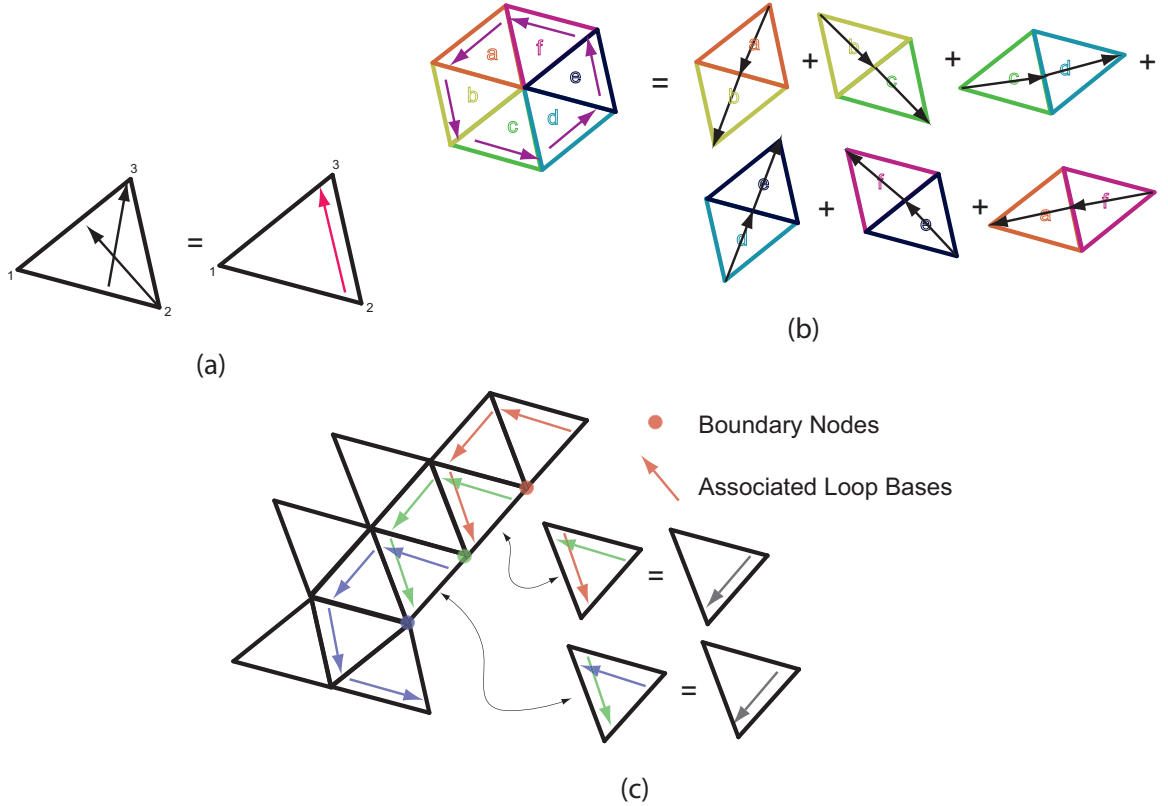


Figure 2.6: Curl conforming expansion functions. (a) Difference between two SP bases combine to form a single curl conforming expansion. (b) Loop expansion formed from an RWG expansion. (c) Partial loop bases along a boundary edge.

bases are formed as in figure 2.6(b). These expansions may be formed from sets of SP curl-conforming bases, or via superposition of RWG bases traversing the edges attached to a common non-boundary vertex. (Complete loop bases have zero divergence and a finite curl, thus they are termed curl-conforming.) Incomplete loop bases are also formed at each boundary vertex (Bv) as shown in figure 2.6(c), and are used in the following chapters. For a simple surface, the number of complete loop basis functions is equal to the number of non-boundary vertices (NBv). In the case of a

surface that contains multiple bounding edges (i.e. has holes or handles) a solenoidal current forms along the bounding edge due to the flux passing through the opening (Faraday’s Law) and an additional loop basis must be introduced to represent this current [25]). Thankfully, these loops are simply formed as the summation of all incomplete loops belonging to the boundary vertices.

2.3 Fast Algorithms

The direct solution of a linear system of N equations through Gaussian elimination requires $O(N^2)$ storage and $O(N^3)$ flop count [49], both of which are impractical for large problems. Alternatively, systems that arise from boundary element integral forms are relatively well conditioned and can be solved by a number of iterative procedures, most popular of which are the Krylov subspace schemes [49].

Such methods attain a solution of acceptable precision by applying the system matrix to a sequence of approximate solutions. Each new guess is improved until the boundary conditions are met to within a desired tolerance. Since these methods rely on repeated application of the matrix-vector product (MVP), the dominant costs are the $O(N^2)$ time and memory spent constructing and storing the matrix and $O(MN^2)$ flops to perform M iterations.

To decrease storage and compute time, both the number of iterations and the flop count of each iteration must be reduced. Improved convergence arises through the application of pre-conditioning methods and will be addressed in Chapter 4. However, reducing the $O(N^2)$ dense matrix cost is the topic of this section on fast algorithms.

2.3.1 Matrix Compression

The purpose of a fast algorithm is to achieve some form of matrix compression, whereby fewer terms must be applied to perform the MVP [50]. Some methods achieve

this by mapping existing unknowns onto regular grids (or existing grid structures) then applying Fourier transforms or algebraic techniques. Such methods include the adaptive integral method (AIM) [20], the array decomposition method (ADM) [21], and the multilevel matrix decomposition algorithm (MLMDA) [22]. Alternative approaches concentrate less on regularizing the underlying structure and more on developing low rank equivalent forms for distant interactions. Such include QR and SVD based methods [30, 31]. The most efficient techniques take the approach of applying equivalent series expansions to model the underlying interaction. The most popular of these expansion methods is the Fast Multipole Method (FMM) [33, 51–53], with lower cost diagonalized forms [32, 54].

In this work two fast algorithms are employed.

SVD Matrix Compression

The first compression method employed operates on pre-computed matrix blocks resulting in efficient low-rank equivalent forms at the expense of increased setup time. The singular value decomposition (SVD) is used for rank-deficient matrix compression as discussed in [30]. While Gram-Schmidt Orthogonalization (QR) would exhibit reduced overhead with equivalent performance, the straightforward nature of the SVD approach is employed for simplicity. Low Rank equivalent forms are computed from the SVD

$$\bar{\mathbf{A}} = \bar{\mathbf{U}}\Sigma\bar{\mathbf{V}}^* \quad (2.71)$$

by extracting only the i^{th} dominant eigenvalues $i|\lambda_i/\lambda_{\max}| > \epsilon$ relative to the desired numerical precision ϵ . The Left and Right low rank equivalent forms are

$$\bar{\mathbf{L}}(:, i) = \bar{\mathbf{U}}(:, i) \quad (2.72)$$

$$\bar{\mathbf{R}}(i, :) = \Sigma(i, i)\bar{\mathbf{V}}^*(i, :). \quad (2.73)$$

If applied to the complete matrix, this technique would result in an $O(N^{1.5})$ interaction at the expense of $O(N^3)$ setup. However, because of the unique implementation outlined in the next chapter, this method is only employed to mid-range unique facet interactions over which the non-oscillatory nature of the kernel results in significant rank reduction. Distant interactions are performed by application of the low frequency multilevel fast multipole method outlined below.

Low Frequency Multilevel Fast Multipole

Multilevel Fast Multipole Overview The multilevel fast multipole method employs a tree structure to organize interactions between groups (clusters) of basis functions. Starting with a complete basis set, successively smaller clusters are formed. By employing approximate series expansions, the interaction between distant clusters is performed at reduced cost because the number of expansion terms needed to represent distant fields is lower than the number of basis functions generating these fields. Making the technique multilevel, outgoing expansions for lower level clusters are used to form like expansions of larger and larger groupings. Similarly, incoming expansions are filtered down from higher level to lower level clusters. The efficiency of the multilevel fast multipole method comes from aggregating outgoing expansions by passing them up the tree structure, translating the expansions between sufficiently distant clusters at all levels, and then disaggregating the incoming expansions down the tree to determine the resulting potentials across all bases.

LF-MLFMA As discussed in the introduction, issues arise when applying the well known dynamic multilevel fast multipole algorithm, valid at mid-range frequencies, to the evanescent regime. In particular, the complex component of the second order Hankel function used in the diagonalized translation matrix is divergent (at a rate proportional to the function order) as the argument approaches zero. However, even

if proper scaling is applied it becomes apparent that the plane wave expansion is not capable of properly representing evanescent interactions [36].

However, the un-diagonalized LF-MLFMA [34], formed in terms of only multipole expansions, does achieve matrix compression at low frequencies if properly scaled [34]. As the interaction distance becomes significant ($> \lambda/3$), the number of multipoles required approaches the number of bases being represented, and the interaction is no longer low rank. Over the range of frequency and structural dimension employed in this work, the scaled LF-MLFMA first published in [55] can provide a significant reduction in memory overhead. Unlike the alternative diagonalized versions that employ evanescent wave expansions, frame of reference rotation is a straightforward operation and is beneficial in the structural definition of the next chapter. Because the number of spherical harmonic terms needed to represent a set of bases to a given accuracy is the same at all levels (it is scale invariant) the LF-MLFMA is asymptotically an $O(N)$ procedure. One significant downside to using this approach is that its numerical accuracy scales as $(0.75)^p$ [56], where p the number of multipoles needed in the scalar expansion. To achieve a minimum four digit accuracy, 36 multipoles are needed and, in the case of vector interactions, the near term interaction list is expanded to include second-nearest neighbors in order to maintain the accuracy desired.

LF-MLFMA Formulation The LF-MLFMA normalized translation equation expressed in its compact matrix form is

$$\bar{\alpha}(\mathbf{r}_{ij}) = \bar{\beta}(\mathbf{r}_{jJ}) \bar{\alpha}(\mathbf{r}_{JI}) \bar{\beta}(\mathbf{r}_{Ii}) \quad (2.74)$$

where $\mathbf{r}_{ij} = \mathbf{r}_{jJ} + \mathbf{r}_{JI} + \mathbf{r}_{Ii}$. Thanks to the use of multipole expansions throughout, no modified filtering algorithms such as those used in [32, 54] are necessary to pass expansions between tree levels. The translation matrices representing outgoing and

incomming spherical harmonic expansions are defined as

$$\bar{\boldsymbol{\alpha}}(\mathbf{r}, k_0)_{L',L} = \sum_{L''} j_{\ell''}(k_0 r) Y_{\ell'',m-m'}(\theta_r, \phi_r) \Upsilon_{L,L',L''} \quad (2.75)$$

$$\bar{\boldsymbol{\beta}}(\mathbf{r}, k_0)_{L',L} = \sum_{L''} h_{\ell''}^{(2)}(k_0 r) Y_{\ell'',m-m'}(\theta_r, \phi_r) \Upsilon_{L,L',L''}. \quad (2.76)$$

Here, $j_{\ell''}(k_0 r)$ is the zeroth order spherical bessel function of ℓ'' order, $h_{\ell''}^{(2)}(k_0 r)$ is a second order spherical hankel function of ℓ'' order, and $Y_{\ell'',m-m'}(\theta'', \phi'')$ is the spherical harmonic function. Furthermore,

$$\Upsilon_{L,L',L''} = 4\pi(-j)^{\ell'+\ell''-\ell} A_{L,L',L''}, \quad (2.77)$$

where $A_{L,L',L''}$ is the Gaunt coefficient in terms of the Wigner 3-j symbol. The indices are further expanded as $L = (\ell, m)$, $L' = (\ell', m')$ and $L'' = (\ell'', m'')$. The translation equation is related to the scalar Green's function via

$$g(\mathbf{r}_j, \mathbf{r}_i) = -j k_0 \alpha_{0,0}(\mathbf{r}_{ij}, k_0). \quad (2.78)$$

Direct formation of the LF-MLFMA matrices in terms of sparse component matrices is implemented utilizing the linear indices

$$L^{(t),(u)} = m^{(t),(u)} + \ell^{(t),(u)2} + \ell^{(t),(u)} + 1 \quad (2.79)$$

and matrices defined as

$$\overline{\mathbf{SH}}(L'', \ell'' + 1) = Y_{\ell'', m''}(\tilde{\theta}_r, \tilde{\phi}_r) \quad (2.80)$$

$$\overline{\mathbf{JV}}(\ell'', 1) = j_{\ell''}(rk) \quad (2.81)$$

$$\overline{\mathbf{YV}}(\ell'', 1) = y_{\ell''}(rk) \quad (2.82)$$

$$\overline{\mathbf{AM}}(L', (L - 1)(\ell''_{\max} + 1)^2 + L'') = 4\pi(-j)^{\ell' + \ell'' - \ell} A(L, L', L''). \quad (2.83)$$

Note that the matrix $\overline{\mathbf{AM}}$ is structurally independent so it can be formed as a sparse matrix and stored for large ranges of L , L' , and L'' without need for repeated computation. The desired translator matrices are then

$$\overline{\boldsymbol{\beta}}(\mathbf{r} k) = \overline{\mathbf{AM}} \text{bdiag}(\overline{\mathbf{SH}} \mathbf{JV}, (\ell_{\max} + 1)^2) \quad (2.84)$$

$$\overline{\boldsymbol{\alpha}}(\mathbf{r} k) = \overline{\boldsymbol{\beta}}(\mathbf{r} k) - j \overline{\mathbf{AM}} \text{bdiag}(\overline{\mathbf{SH}} \mathbf{YV}, (\ell_{\max} + 1)^2). \quad (2.85)$$

where $\text{bdiag}(\overline{\mathbf{A}}, n)$ forms a block diagonal matrix with n entries of the matrix $\overline{\mathbf{A}}$.

Multipole Alignment The number of multipole terms needed to interact a pair of clusters can be reduced by aligning their expansions such that the vector between the clusters is along the z-axis [34, 57, 58]. This results in a highly sparse translation matrix (due to the symmetry of the spherical harmonics) and results in a translation that is only distance dependent. While this approach is employed in the current work, a minor modification to the spherical harmonic rotation of [34] is also employed.

Standard spherical harmonic alignment [57, 58] employs only two rotation angles as the transmitting and receiving clusters are assumed to exist in the same coordinate frame. However, as outlined in the next chapter, this implementation employs localized coordinate frames for every cluster. In that case, rotations must be applied not only to align the multipole expansions in the global coordinate frame (via the global angles θ, ϕ), but must be rotated into the global frame via the euler angles

α, β, γ . A generic multipole rotation takes the form

$$\overline{\mathbf{T}}(\mathbf{r}_1) = \overline{\mathbf{R}}^* \overline{\mathbf{T}}(\mathbf{r}_2) \overline{\mathbf{R}}. \quad (2.86)$$

In this implementation the rotation matrices ($\overline{\mathbf{R}}$) employed are formed as

$$\overline{\mathbf{S}} = \overline{\mathbf{D}}(0, \pi/2, 0) \overline{\mathbf{D}}(\pi/2, 0, 0) \quad (2.87)$$

$$\overline{\mathbf{R}}_{\text{EU}} = \overline{\mathbf{D}}(0, 0, \gamma) \left(\overline{\mathbf{S}}^* \overline{\mathbf{D}}(0, \beta, 0) \overline{\mathbf{S}} \right)^* \overline{\mathbf{D}}(\alpha, 0, 0)^* \quad (2.88)$$

$$\overline{\mathbf{R}}_z = \left(\overline{\mathbf{S}}^* \overline{\mathbf{D}}(0, \theta, 0) \overline{\mathbf{S}} \right) \overline{\mathbf{D}}(\phi, 0, 0), \quad (2.89)$$

where the spherical harmonic rotation matrix $\overline{\mathbf{D}}(\alpha, \beta, \gamma)$ is defined in [34]. When implemented into the multilevel form of (2.74) the translation matrices including local to global harmonic rotations are formed as

$$\overline{\boldsymbol{\alpha}}(\mathbf{r}_{\text{global}}, k) = \overline{\mathbf{R}}_z^* \overline{\boldsymbol{\alpha}}(\mathbf{z}_{\text{global}}, k) \overline{\mathbf{R}}_z \quad (2.90)$$

$$\overline{\boldsymbol{\beta}}(\mathbf{r}_{\text{global}}, k) = \overline{\mathbf{R}}_{\text{EU}}^{\text{tx}} \overline{\boldsymbol{\beta}}(\mathbf{r}_{\text{local}}, k) \quad (2.91)$$

$$\overline{\boldsymbol{\beta}}(\mathbf{r}_{\text{local}}, k) = \overline{\mathbf{R}}_{\text{EU}}^{\text{rx}*} \overline{\boldsymbol{\beta}}(\mathbf{r}_{\text{global}}, k). \quad (2.92)$$

The inclusion of the $\overline{\mathbf{R}}_{\text{EU}}$ multipole rotation matrices does significantly effect numerical accuracy [34] or the cost of aligning the multipole expansions for a scalar interaction. For a given interaction the sparse euler rotations can be joined with the global frame rotation, $\overline{\mathbf{R}}_z$, without increasing the number of rotation terms, as shown in figure 2.7. For vector interactions, local to global rotation implies that vector expansions be coordinate rotated to ensure proper expansion function interaction ($\overline{\mathbf{E}}\mathbf{U}$ in figure 2.7).

Implementation with Incomplete Helmholtz Decomposition When LF-MLFMA is used in conjunction with the incomplete Helmholtz decomposition, it is necessary

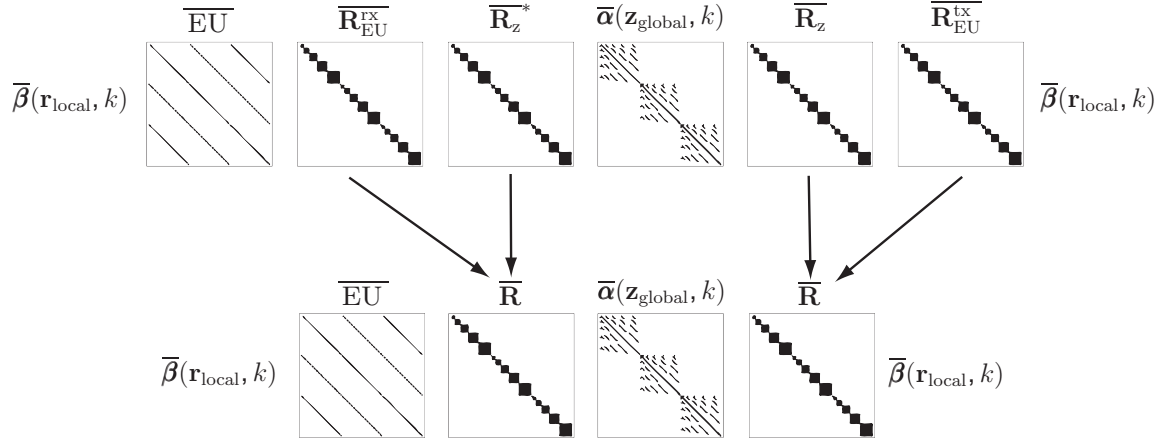


Figure 2.7: Multipole alignment including local coordinate frames.

to employ separate multipole trees for the scaled solenoidal and non-solenoidal currents. Thus, two vector multipole traversals are performed with each iteration [59] unless some form of common sub-basis is applied [34]. Furthermore, large holes or handles within a surface can limit the minimum multipole cluster size as loop bases circumventing handles have large domains. Both of these issues are addressed in Chapter 4.

CHAPTER 3

Multilevel Geometry Description

Many existing numerical approaches compute near-term basis interactions by brute force, that is they do not employ a method of eliminating redundant computations. In this chapter a general purpose redundancy minimization algorithm for both array and arbitrary surface based structures is outlined. By eliminating unnecessary operations, the number of floating point operations (flops) and memory use can be decoupled from the total number of unknowns in the structure. This is particularly important where the overhead required in solving large systems of equations becomes bound by finite computer resources. In these cases, redundancy minimization can enable the solution of a far greater number of unknowns in the same resource space. For problems where proper conditioning results in highly convergent iterative methods, the number of floating point operations employed to setup the system of equations can dominate over the time necessary to solve the system of equations. This is the situation that occurs in many low frequency simulations.

Well known approaches to redundancy minimization rely primarily on the implementation of fast iterative solvers, reducing the $O(N^2)$ cost of computing all matrix entries down to $O(N)$ near term interactions and $O(N)$ or $O(N \text{Log} N)$ multipole expansions (as detailed in the preceding chapter). Further methods take advantage of redundancy in cartesian array type structures [20, 21] or limit overhead during solu-

tion by compartmentalizing the numerical solver using domain decomposition [60–64]. As an alternative, this implementation enforces a new form of structural definition via what is coined a Multi-level Geometry Description (MLGD). Not only does the MLGD permit automated tracking and identification of local and global redundancy in array type structures, but it is equally applicable to the simulation of arbitrary engineered surfaces. By implementing this model the number of unique mesh elements, expansion functions, and their interactions is decoupled from the DOF in the system, significantly reducing the use of computing system resources, extending the upper bound on the size of the solvable system, and reducing the total time to solution.

In the MLGD, surface based structures are constructed via a tiered assembly of unique facets with associated translation vectors and rotation matrices. Using this description, LF-MLFMA is applied in absence of an oct-tree decomposition [34] and identification of a unique minimal set of both near and distant interactions is straightforward. This chapter discusses the geometric operations necessary to assemble an arbitrary surface from a facet subset and resolves implementation challenges involved in the construction of such. Included are details on proper basis formation, bridging disjoint and multiply connected facets, and detecting handles (holes) in the surface structure (an active area of research in its own right).

3.1 Facet Based Geometry

At the geometry description level it is common practice to form a structure from assembled subsurfaces. A surface is replicated, translated, and rotated into a new position and joined as a new part of the existing structure. Minor errors in numerical precision are eliminated by translational correction. However, information about facet symmetry and likeness is lost when a surface meshing algorithm is employed. As an alternative, it is proposed that a basic surface be represented in terms of

a set of elementary facets with a list of translation vectors and rotation matrices. Furthermore, just as an arbitrary surface can be composed of a set of facets, any facet may in turn be composed from other facets. A surface geometry can be defined as a hierarchy of nested surfaces, each included in the one above it through rotation and translation. In the MLGD, a completed surface geometry is simply the highest level facet definition.

To form an MLGD, we begin with a small set of pre-meshed *protofacets* with compatible mesh granularity along their bounding edges. (If mesh independent bases [34] were used, this limitation could be eliminated.) A new surface structure is formed by joining translated and/or rotated protofacets, or other higher-level surfaces already constructed, as in figure 3.1 As each new surface is joined to the existing struc-

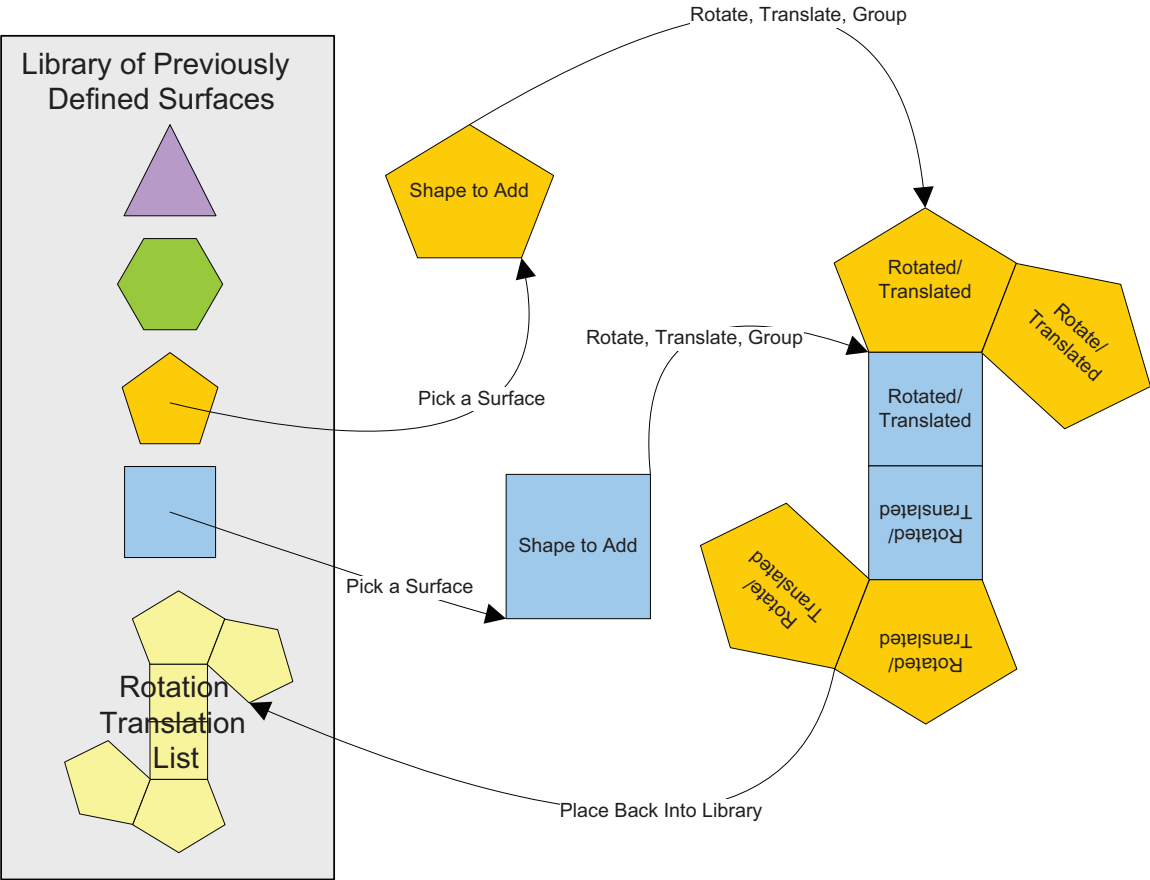


Figure 3.1: Forming an MLGD structure from an existing library.

ture, surface linking information is used to track physical bounding edges and ensure proper basis formation. Following this procedure, the resulting geometry description becomes an oriented graph structure, as depicted in figure 3.2. The nodes of the

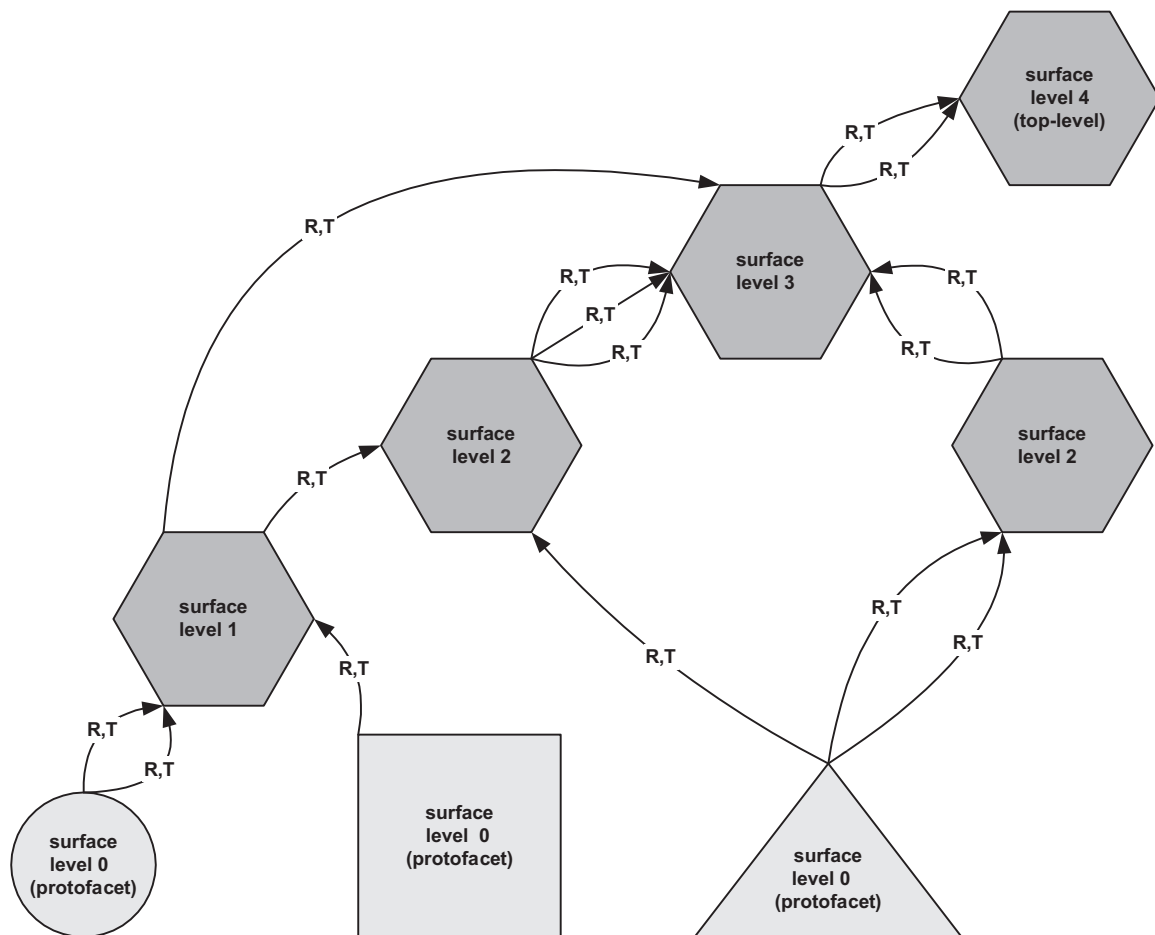


Figure 3.2: Diagram of the MLGD oriented graph structure.

graph represent physical surfaces in local coordinate frames. The edges of the graph represent translation and rotation vectors applied to lower level nodes to form the higher level nodes (surfaces). The the structure mesh is stored only in the finite set of facets at the leaves of the graph, and an extension of the surface geometry incurs only the cost of storing additional translation and rotation information. Furthermore, information about redundancy (facets with identical shape or identical interactions) remains within the structural definition and can be used to great advantage in the

numerical method. It is now necessary to define the construction of the nodes and edges of this oriented graph.

3.1.1 Protofacets

The first type of graph node is the “protofacet”. This node contains rudimentary mesh information, and there is at least one of these structures at bottom of every MLGD. While it would be possible to start an MLGD definition for a single triangular patch or small rectangle, it is not practical from a design point of view to build a substantial structure by hand from such a rudimentary shape. Thus, protofacet nodes are imported as small meshed surfaces. Each protofacet includes vertex coordinates (in a local frame of reference), relations between the vertices and the edges, and relations between the mesh patches and one or both of the previous components (i.e. all the standard components defining a surface mesh). To ensure and simplify proper connectivity within the structure, the edges and vertices of each protofacet are defined using a counter-clockwise patch-vertex-edge ordering such that surface normals computed as the cross product of the patch edges are consistent. It is not necessary that vertices interior to a protofacet be indexed in a counter-clockwise fashion, but the boundary vertices and edges are ordered to facilitate an efficient implementation.

Mesh Definition

The rudimentary building blocks of a mesh are the vertices, each of which is a point in the local coordinate frame represented by three cartesian values. Within a protofacet, the set of all vertices is gathered together into a matrix $\overline{\overline{V}}$, where the j^{th} vertex is defined by the entries in the j^{th} column of the matrix. In addition, in order to ensure efficient indexing, the vertices about the bounding edge of the protofacet are counterclockwise indexed and represent the leading columns of the vertex matrix.

The next component of the mesh is the edge element definition that depicts connectivity between the vertices. Rather than a simple look-up table, a sparse mapping is employed, where a +1 entry defines a “tail” connection to a vertex, and a −1 entry defines a “head” connection to a vertex. This results in a vertex-edge sparse mapping $\overline{\overline{\text{Mve}}}$ with vertex row indices j and edge indices k along the columns.

$$\overline{\overline{\text{Mve}}}(j, k) = \begin{cases} +1, & \{j \mid j = \text{tail}\} \\ -1, & \{j \mid j = \text{head}\} \end{cases} \quad (3.1)$$

For example, the k^{th} edge of the mapping with a tail at the 3rd vertex and a head at the 5th vertex is

$$\bar{e}_k = \overline{\overline{\text{Mve}}}(:, k) = \begin{bmatrix} 0 \\ 0 \\ +1 \\ 0 \\ -1 \\ 0 \\ \dots \end{bmatrix}. \quad (3.2)$$

The k^{th} edges corresponding to mesh boundary edges are counterclockwise indexed about the profacet and represent the first group of ordered columns in this mapping.

Next, in order to maintain a consistent orientation the following edge-patch mapping is formed. Applying counter-clockwise ordering, the sparse edge-patch mapping, $\overline{\overline{\text{Mep}}}$, is formed with +1 entries at the indices of correctly oriented row edge elements (to form the patch in the counterclockwise direction) and a −1 for those that are clockwise oriented.

$$\overline{\overline{\text{Mep}}}(j, \ell) = \begin{cases} +1, & \{(j, \ell) \mid j \in t_i \wedge \text{CCW}\} \\ -1, & \{(j, \ell) \mid j \in t_i \wedge \text{CW}\} \end{cases}. \quad (3.3)$$

Here the patch index ℓ has three values $\ell = 3(t_i - 1) + \ell_L$, corresponding to the first, second, and third local edge $\ell_L = [1, 2, 3]$ in a right handed orientation about the t_i^{th}

patch. For example, a single patch to edge mapping is

$$\bar{p}_\ell = \overline{\overline{\text{Mep}}}(:, \ell) = \begin{bmatrix} 0 & 0 & -1 \\ +1 & 0 & 0 \\ 0 & 0 & 0 \\ 0 & 0 & 0 \\ 0 & +1 & 0 \\ \dots & \dots & \dots \end{bmatrix}. \quad (3.4)$$

By filtering and transforming the mappings above, key characteristics of the mesh are extracted. The next mapping of interest describes the set of Boundary Elements (**BE**), e.g. those elements along the boundary of the current mesh. Such are the set of elements that belong to only a single patch, defined as

$$\mathbf{BE} = \{j \mid \text{colsum}\{\overline{\overline{\text{Mep}}}(j, :)\} = 1\}, \quad (3.5)$$

and represented in the sparse mapping

$$\overline{\overline{\text{MeBe}}}(j, be) = +1, \quad \{(j, be) \mid j \in \mathbf{BE}\}. \quad (3.6)$$

Care is taken to ensure each of the be^{th} boundary edges follow a counterclockwise indexing about the facet. The dual mapping for the non-boundary edges is

$$\overline{\overline{\text{MeNBe}}}(j, nbe) = +1, \quad \{(j, nbe) \mid j \notin \mathbf{BE}\}, \quad (3.7)$$

where the order of the non-boundary elements, nbe , is not particular.

Physical Vertices and Edges

To enable efficient mesh interconnectivity at higher levels of the nested structure, “physical” vertices and “physical” boundary edges are tracked in the oriented graph structure. These edges and vertices are what make up the geometry description of

the facet boundary prior to meshing. Each group of boundary edges making up a given physical edge (as provided by the surface meshing algorithm) is organized into the physical edge set,

$$\mathbf{PE}(pe) = \{j \mid j \in pe \text{ edge}\}. \quad (3.8)$$

This information is then used to form the profacet edge-physical edge mapping $\overline{\overline{\text{MePe}}}$. In this mapping, +1 is entered at row indices for mesh edges that belong to a given physical edge.

$$\overline{\overline{\text{MePe}}}(j, pe) = +1, \quad \{(j, pe) \mid j \in \mathbf{PE}(pe)\}. \quad (3.9)$$

For example, a the pe^{th} physical edge formed by joining mesh boundary edges 3, 5, and 6,

$$\overline{\overline{\text{MePe}}}(:, pe) = \begin{bmatrix} 0 \\ 0 \\ +1 \\ 0 \\ +1 \\ +1 \\ \dots \end{bmatrix}. \quad (3.10)$$

Again, because of proper ordering the boundary edges are all counterclockwise indexed and only positive entries are necessary. A physical vertex mapping for the same facet is also formed as

$$\overline{\overline{\text{MvPv}}}(i, j) = +1, \quad \{(i, j) \mid \overline{\overline{\text{Mve MePe}}}(i, j) = -1\}. \quad (3.11)$$

Further mappings are formed through multiplication and filtering. For example, in order to find the mapping between the physical vertices and a physical edge, pe , I compute $\overline{\overline{\text{MPvPe}}} = \overline{\overline{\text{Mve MePe}}}$. Therein, only physical vertices remain because interior vertices are the head of one edge and the tail of another ($+1 + -1 = 0$), while vertices at the ends of the physical edge are only head or tail ($+1$ or -1). Mappings

to the interior vertices on a physical edge are formed as

$$\overline{\overline{\text{MivPe}}}(i, pe) = +1, \quad \{(i, pe) \mid \left[\overline{\overline{\text{Mve}}} \overline{\overline{\text{MePe}}} \right] (i, pe) = 2\}, \quad (3.12)$$

where the absolute value ensures that common vertices do not cancel, ($|+1| + |-1| = 2$), as those that are used twice make up the desired set.

By adopting sparse mappings to relate mesh connectivity sets, information used in the numerical method relating to edge and vertex connectivity can be simply extracted via matrix operations.

3.1.2 Graph Nodes

The goal of using an MLGD is to minimize the information used to define facet interconnectivity at higher levels while at the same time providing a method to properly interconnect subsurface edges and vertices as the structure is defined.

However, before detailing the method of forming this hierarchy, it is first necessary to discuss a method of applying facet rotation and translation, termed “ghosting”. A ghost of a facet, or “ghostfacet” does not include any mesh information, but simply contains the relative location vectors and orientation angles (via a Euler rotation matrix [65]), along with a pointer to its profacet (or graph node) definition. An assembly of ghostfacets is a graph node.

Facet Translation and Rotation

In order to form a ghost, i.e. a translation vector and rotation matrix, it is necessary to define local-to-global and global-to-local coordinate transforms. I first discuss the act of rotating the facet at P about a unit vector $\hat{\xi}$ that passes through the points Q and N , as shown in figure 3.4. The facet at point P with local coordinate system $(\hat{x}', \hat{y}', \hat{z}')$ is related to the global origin O with global coordinate system

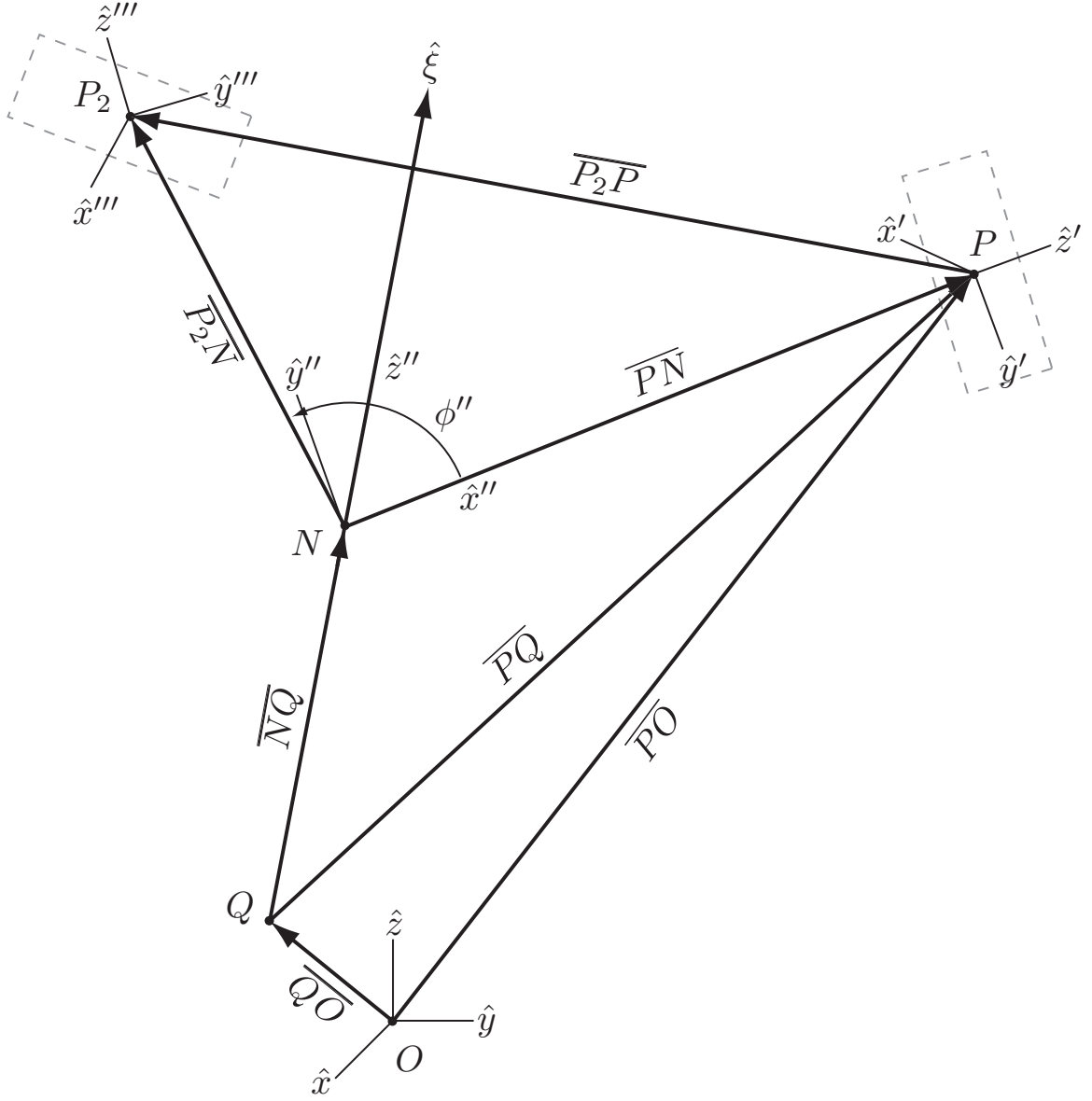


Figure 3.3: Translation and rotation of a facet about a line through a point.

$(\hat{x}, \hat{y}, \hat{z})$ through the vector $\overline{PO} = \overline{P} - \overline{O}$. The component of \overline{PO} in the direction of $\hat{\xi}$ is defined as the vector \overline{NO} . The unit vector $\hat{\xi}$ is related to the global coordinate system via

$$\hat{\xi} = \frac{\xi_x \hat{x} + \xi_y \hat{y} + \xi_z \hat{z}}{\sqrt{\xi_x^2 + \xi_y^2 + \xi_z^2}}. \quad (3.13)$$

The facet at point P is rotated in the right hand sense about the unit vector $\hat{\xi}$. Thus, we treat $\hat{\xi}$ as the \hat{z}'' component of a standard cartesian frame with \overline{PN} falling along the \hat{x}'' direction, and our rotation angle defined by ϕ'' . The coordinate frame denoted by $(\hat{x}'', \hat{y}'', \hat{z}'')$ is the local coordinate system for $\hat{\xi}$. In doing so, the point P is translated (in the global coordinate frame) to the location P_2 . First P_2 must be found, then the global rotation must be mapped into the euler rotation [65] with respect to the global frame.

Translation If $\hat{\xi}$ relates to some \hat{z}'' , and \overline{PN} relates to some \hat{x}'' , then

$$\overline{P_2N} = \overline{\overline{EU_\xi}}^T \begin{bmatrix} \cos(\phi'') & -\sin(\phi'') & 0 \\ \sin(\phi'') & \cos(\phi'') & 0 \\ 0 & 0 & 1 \end{bmatrix} \overline{PN} = \overline{\overline{EU_\xi}}^T \overline{\overline{T_{P_2/P}}} \overline{PN}. \quad (3.14)$$

$\overline{\overline{EU_\xi}}$ is the Euler rotation matrix relating $(\hat{x}'', \hat{y}'', \hat{z}'')$ to the global system $(\hat{x}, \hat{y}, \hat{z})$.

Now, the point P_2 is

$$\overline{P_2O} = \overline{QO} + \overline{NQ} + \overline{P_2N}. \quad (3.15)$$

Substituting (3.14) into (3.15) results in

$$P_2 = Q + \overline{NQ} + \overline{\overline{EU_\xi}}^T \overline{\overline{T_{P_2/P}}} (P - Q - \overline{NQ}). \quad (3.16)$$

Next, \overline{NQ} is the projection of \overline{PQ} along the direction $\hat{\xi}$, so $\overline{NQ} = \hat{\xi}(\overline{PQ} \cdot \hat{\xi})$, and $N = \overline{NQ} + Q$. The translation vector becomes

$$\overline{V_t} = \overline{P_2P} = \overline{NQ} - \overline{PQ} + \overline{\overline{EU_\xi}}^T \overline{\overline{T_{P_2/P}}} (\overline{PQ} - \overline{NQ}). \quad (3.17)$$

It is important to note in the current implementation that translations are defined relative to the center of mass of the surface as it is constructed (to aid in the proper formation of clusters in fast multipole implementation). These translations are up-

dated as each new subsurface is added to the current working graph node.

Rotation With translation determined, the Euler rotation matrix can now be found. To perform this rotation the original facet is transformed as follows:

1. Convert the local coordinate system of the facet to the global system using $\overline{\overline{EU_o}}^T$, where $\overline{\overline{EU_o}}$ is the facets original Euler rotation matrix.
2. Convert the global coordinate system to the system local to $\hat{\xi}$ using $\overline{\overline{EU_\xi}}$.
3. Perform the rotation of $\overline{\overline{T_{P_2/P}}}$.
4. Convert back to the global coordinate system using $\overline{\overline{EU_\xi}}^T$.
5. Transpose the entire operation to obtain the final Euler rotation matrix.

Mathematically this results in the following modified Euler rotation matrix for the rotated facet,

$$\overline{\overline{EU_{\text{new}}}} = \left[\overline{\overline{EU_\xi}}^T \overline{\overline{T_{P_2/P}}} \overline{\overline{EU_\xi}} \overline{\overline{EU_o}}^T \right]^T. \quad (3.18)$$

Using a non-linear least squares algorithm [66], the euler rotation angles (α, β, γ) are determined from $\overline{\overline{EU_{\text{new}}}}$ and included in the ghostfacet definition for application to the multipole rotations in the preceding chapter.

Building Nodes

As depicted in figure 3.1, each node in the oriented graph definition is a surface in its own right. When first forming a graph node, the node takes on the physical parameters of the its first ghost. The ghost definition (i.e. rotation and translation) is added into the node subsurface matrix $\overline{\overline{GSS^n}}$ (therein n superscript indicates that it belongs to the node). The transformed physical vertices of the ghost are placed in the node vertex matrix $\overline{\overline{V^n}}$, and the physical vertex-edge mapping of the ghost is adopted by the node $\overline{\overline{Mve^n}} = \overline{\overline{MPvPe}}$.

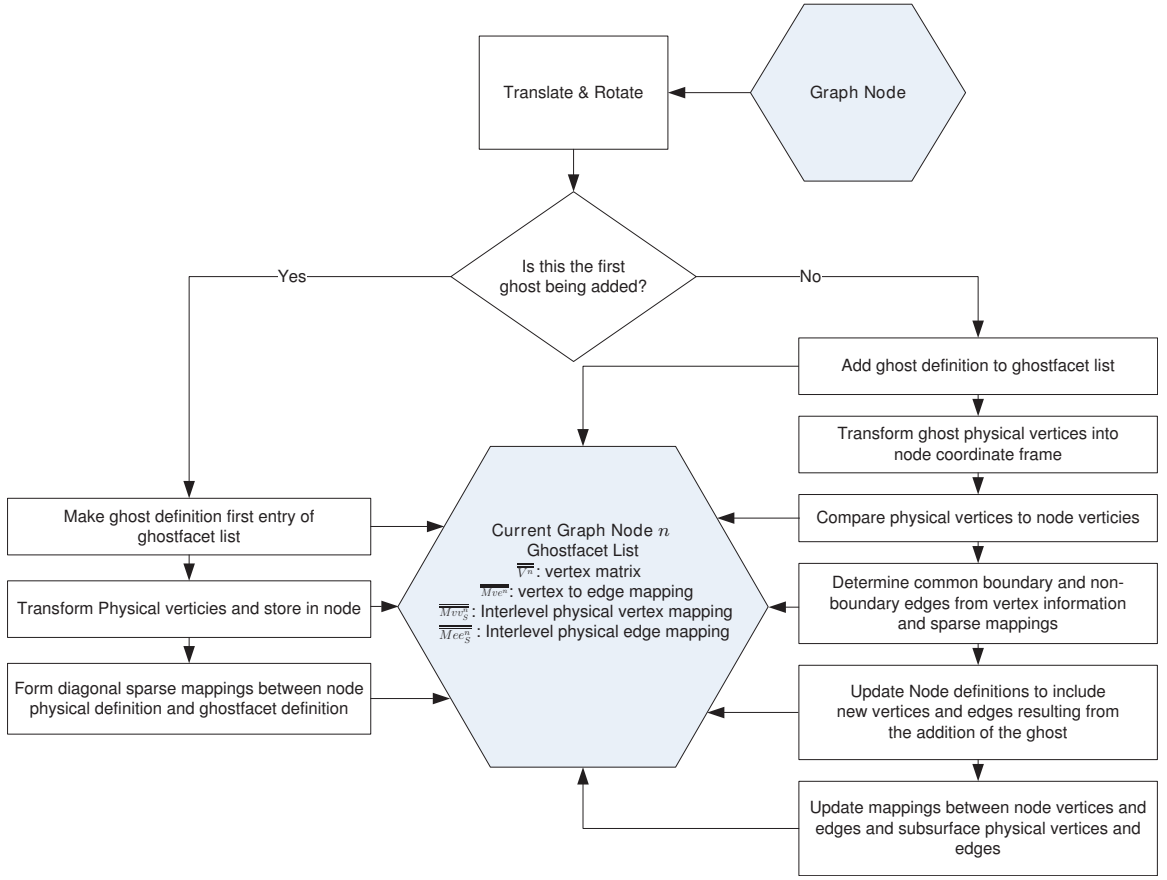


Figure 3.4: Diagram outlining the procedure for construction of an MLGD node.

In the last section an expanded patch indexing, ℓ , was used in mapping protofacet patches to their edge matrices via $\overline{\overline{Mep}}$. Similarly, physical edges can be treated as local edges of a facet that is a subsurface of a higher level facet. In order to traverse the relationship between the subsurface and supersurface node definitions, sparse mappings between physical parameters of the node and its subsurfaces are created. Like the relationship between triangles and edges in the protofacet, these new interlevel mappings use extended indexing. The node vertex to subsurface physical vertex mapping is formed by comparing existing node vertices to those of the ghost being added

$$\overline{\overline{Mvv_S^n}}(i, \ell_v) = +1, \quad \{(i, \ell_v) \mid i == \ell_v\}. \quad (3.19)$$

Therein, ℓ_v is a linear index to the physical vertex of the current ghost. Similarly, the graph node edge to subsurface physical edge mapping is defined as

$$\overline{\overline{Mee}}_S^n(j, \ell_e) = \begin{cases} +1, & \{(j, \ell_e) \mid j \Rightarrow \ell_e\} \\ -1, & \{(j, \ell_e) \mid j \Leftarrow \ell_e\} \\ 0, & \text{otherwise} \end{cases}, \quad (3.20)$$

with ℓ_e being the linear index to the physical edge of the current ghost, \Rightarrow depicting edges oriented in the same direction, and \Leftarrow depicting edges oriented in opposing directions. When first formed, both of these interlevel mappings are sparse identity matrices. As each additional ghost is added to a node, the ghost's transformed physical vertices are compared to the node's vertex matrix (see figure 3.1) and the set of unique vertices and edges that make up the updated node description are merged into $\overline{\overline{V}}_n$ and $\overline{\overline{Mve}}_n$. The sparse mappings $\overline{\overline{Mvv}}_S^n$ and $\overline{\overline{Mee}}_S^n$ are updated to include each new subsurface. Like a protofacet, each higher level node of the graph contains sparse mappings relating its subsurfaces to physical edges and vertices.

3.1.3 Recursing the Graph

In order to determine the set of unique interactions and to clearly plot the underlying MLGD structure it is necessary to recurse the multilevel description. Beginning at the top of the graph, the location and orientation of each branch is successively modified as the recursion traverses down to the leaf level. The location and orientation of each higher level node is passed down to the current node via

$$\ell_{>} = \overline{\overline{\mathbf{E}\mathbf{U}}}_{>}^T \ell_{<} + \ell_{>} \quad (3.21)$$

$$\overline{\overline{\mathbf{E}\mathbf{U}}}_{>} = \overline{\overline{\mathbf{E}\mathbf{U}}}_{<} \overline{\overline{\mathbf{E}\mathbf{U}}}_{>}. \quad (3.22)$$

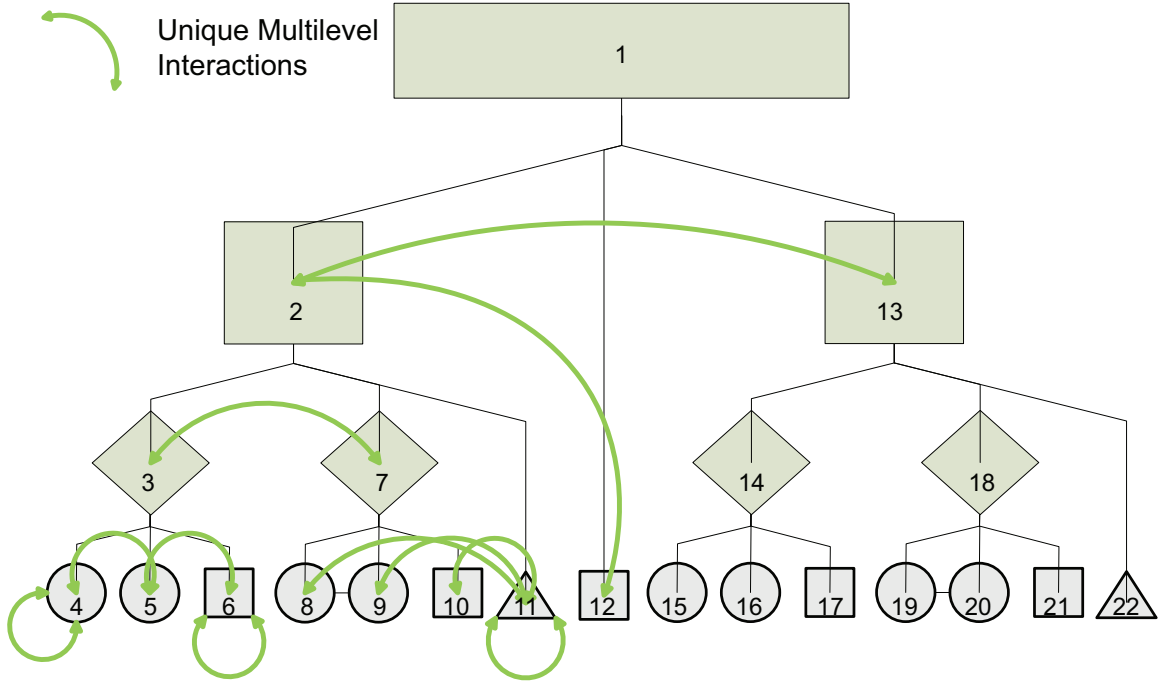


Figure 3.5: Recursion tree of the MLGD structure. Arrows indicate unique interactions. Linear indexing of the tree structure is also shown.

$\ell_{>}$ is the translation from above and $\ell_{<}$ is the translation at the current level, $\overline{\mathbf{E}\mathbf{U}}_{>}$ is the rotation passed down and $\overline{\mathbf{E}\mathbf{U}}_{<}$ the the rotation at the current level. At the leaf level of the MLGD, each local coordinate vertex \mathbf{v}_i in the global frame is transformed as

$$\mathbf{v}_i = \ell_{>} + \overline{\mathbf{E}\mathbf{U}}_{>}^T \mathbf{v}_i. \quad (3.23)$$

To properly employ the interaction search algorithm in the following section, it is necessary to maintain a linear index of the MLGD tree structure during recursion. Starting with 1 as the index of the top level surface, each subsurface in the expanded tree is assigned an incremental index based on the progression of the recursion, as depicted in figure 3.5.

Integrity of the Meshed Structure Successive rotation of a nested protofacet can accumulate location and orientation error. The final location and orientation

of the facet can be altered due to floating point errors in applying successive Euler matrix rotations and translations in finite precision arithmetic. Thankfully, MLGD vertices are defined in local coordinate frames and dilation does not occur.

However, to ensure proper mesh interconnectivity, translational and/or rotational error is removed during construction by applying corrections to ghostfacet definition before it is saved in the nodes ghostfacet list. This way latter recursions into the structure are error free to machine precision.

These corrections are performed by using a snap geometry. When the physical vertices along of a new ghostfacet are compared to those of the existing node, vertices within a given tolerance are assumed to be the same. Next, relative errors for multiple snapped vertices (i.e. those on a common edge) are compared. If the errors are of nearly equal magnitude in the node's frame of reference, then simple translational correction is all that is required, and it is included into the ghost translation vector. If the error between the points is such to that it suggests the need for rotational correction, the angle of the rotation in the global coordinate frame is determined from the vertex error magnitudes, and a correction is applied to the Euler rotation.

As these errors begin at the level of machine precision and accumulate as the geometry is constructed, they are slow growing and, in most cases translational correction is sufficient throughout most of a structural definition.

3.2 Interactions and Interconnectivity

With the basic form of the MLGD definition outlined, it is now possible to introduce algorithms that benefit the numerical method by using the information stored in the MLGD.

3.2.1 Minimum Interaction Set

As can be seen from the the MLGD structure, local “likeness” information about the surface structure is now available to the numerical solver. Using this information within the numerical method allows a reduction in the number of redundant computations performed for both near and distant interactions. In turn, both direct and multipole pre-computation and storage are reduced. However, to take advantage of this structure the set of unique interactions must be determined by comparing interactions forming an interaction list.

Comparing Interactions

Consider the i^{th} interaction pair separated by a distance \mathbf{d}^i in the global coordinate frame. The separation vectors in relation to the receiving and transmitting facets (in the global coordinate frame) are computed as $\mathbf{V}_{\text{rx}}^i = \overline{\mathbf{E}\mathbf{U}}_{\text{rx}}^i (-\mathbf{d}^i)$ and $\mathbf{V}_{\text{tx}}^i = \overline{\mathbf{E}\mathbf{U}}_{\text{tx}}^i \mathbf{d}^i$, respectively. Therein $\overline{\mathbf{E}\mathbf{U}}_{\text{rx}}$ and $\overline{\mathbf{E}\mathbf{U}}_{\text{tx}}$ are the Euler rotation matrices relating the local to global coordinate frames for the receiving and transmitting facets in the pair. For a pair of interactions i and j with known type, their relative separations are compared in terms of an acceptable error criterion ϵ .

$$\|\mathbf{V}_{\text{rx}}^i - \mathbf{V}_{\text{rx}}^j\|_2 + \|\mathbf{V}_{\text{tx}}^i - \mathbf{V}_{\text{tx}}^j\|_2 \leq \epsilon \mapsto \text{same} \quad (3.24)$$

$$\|\mathbf{V}_{\text{rx}}^i - \mathbf{V}_{\text{tx}}^j\|_2 + \|\mathbf{V}_{\text{tx}}^i - \mathbf{V}_{\text{rx}}^j\|_2 \leq \epsilon \mapsto \text{transpose.} \quad (3.25)$$

If either of the the above inequalities are true, identical, and transposed interactions are identified. If they are both false, then the interaction is a “new” interaction.

Searching the MLGD

Two options exist for implementing an interaction search algorithm. The method most transparent to the end user is to compare the set of interactions that result as

each new ghost is added to an MLGD node (keeping the number of interactions to search at a minimum and building on the information gathered as the geometry is constructed). However, such an approach requires that multipole cluster separation and other fast algorithm criteria be determined before the structure dimensions and number of MLGD levels are known. A more flexible approach is to search the MLGD graph once the structural definition is complete, using fast algorithm oct-tree criteria to determine near and distant interactions.

The search algorithm proceeds as follows:

Starting at the top of the MLGD oriented graph, the recursion algorithm discussed above is applied to recurse into the structure. By augmenting the ghost definitions in each node with a measure of subsurface dimension, interactions between the subsurfaces are compared by separation distance.

First, every pair of subsurface interactions on the current node is compared to the set of interactions already traversed (using (3.24)). If an interaction is found to match one already documented, then the linear indices (see figure 3.5) of two subsurfaces are added to the interaction along with the match criteria.

Since distant interactions are computed using the MLFMA, they are not further recursed. Also, interactions (near or far) already included in the interaction list have known interaction indexing patterns and need not be recursed again. Thus, only unrecorded near-term interactions are recursed and compared directly to the interaction list.

3.2.2 Expansion Function Connectivity

In the case of electrostatic formulations, pulse basis functions are adopted with high accuracy and excellent conditioning. Since pulse basis domains exist only over individual patches, interaction between disjoint surfaces requires no further consideration. However, simulation of surface currents requires continuity between patches be

enforced, and thus the use of vector bases with multi-patch domains. In the case of the MLGD, since the structure is assembled from a subset of protofacet elements, it is necessary to ensure bridging [21] bases are introduced to enforce continuity in the structure. The basic building blocks for these bridge bases are formed as the MLGD structure is assembled, and are stored in the MLGD nodes.

Divergence Conforming Bridges As detailed in the second chapter, the divergence conforming bases thus far discussed include RWG, Tree, and Star expansions. RWG bases are edge based elements with domains traversing only two patches. In the MLGD, an interior physical edge at vertex n maps (via $\overline{\overline{Mee_s^n}}$) to the sets of boundary edges shared by a pair of its subsurfaces. If this mapping is traversed down to the protofacet level, and all facets have maintained a consistent indexing, it is straightforward to introduce one additional RWG basis for each abutted protofacet edge element, as shown in figure 3.6(a). Similarly, tree function mappings must be included across the interior edges of nodes in the MLGD. However, care must be taken to ensure that the overall tree expansion set does not loop back on itself (such that it supports a strongly solenoidal current). In order to ensure this, the same algorithm applied to determine the tree edges of the protofacet Tree expansion are applied to determine the interior edges of the current, as in figure 3.6(d). This approach is repeated up from the protofacet level, and a single RWG expansion function along each required edge is selected (figure 3.6(b)) and stored in each node.

Like the tree bases, star basis bridging would contribute one new basis for each subsurface added to a node (figure 3.6(c)). However, unlike the tree bases, a complete star basis set would require that missing arms of subsurface stars along shared edges be reinserted when bridging subsurfaces and one additional star be included in all but one of the leaf facets. This is not practical for an efficient MLGD definition, as it is preferred that all subsurface expansions be complete at their own level. For this

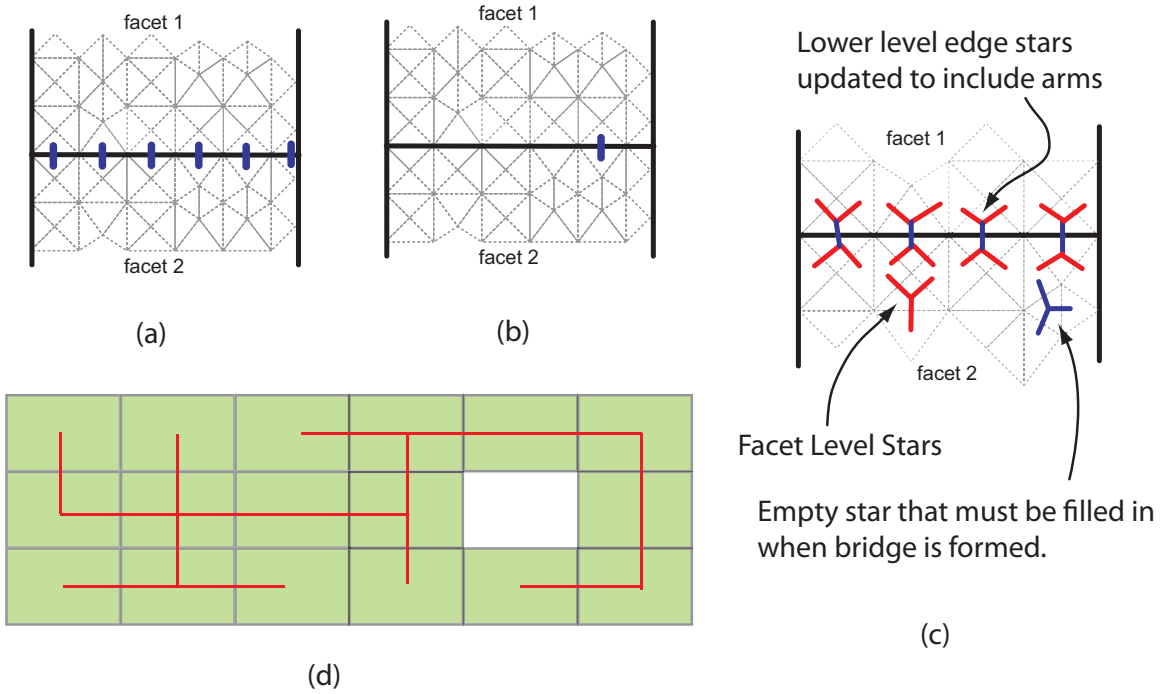


Figure 3.6: Divergence conforming bridge bases. (a) RWG bridge bases. (b) Tree bridge basis. (c) Star bridge bases. (d) Hierarchical selection of edges onto which tree bridge bases are applied.

reason, star bases are not applied in the current implementation of MLGD.

Curl Conforming Bridges For curl conforming (loop) bases, the approaches taken for both the RWG and Tree expansions above comes into play. Much like RWG bases, all interior edges of a given graph node require that Loop bases be introduced for shared sublevel vertices (see figure 3.7(a)). In the case where non-boundary vertices or *handles* are formed in a graph node, loops as shown in figure 3.7(b) and figure 3.7(c) are introduced. By applying the non-boundary edge and vertex indices of a node to the physical edge and vertex mappings, $\overline{\overline{Mee_s^n}}$ and $\overline{\overline{Mvv_s^n}}$, a recursion is used to descend the MLGD and return sets of loop mappings associated with the edges and vertices of the lower level definitions. Because of the consistent ordering employed throughout, properly gathering these sets of bases is trivial. If the edge is a non-boundary edge, then mappings for each lower level vertex are joined to form sets of

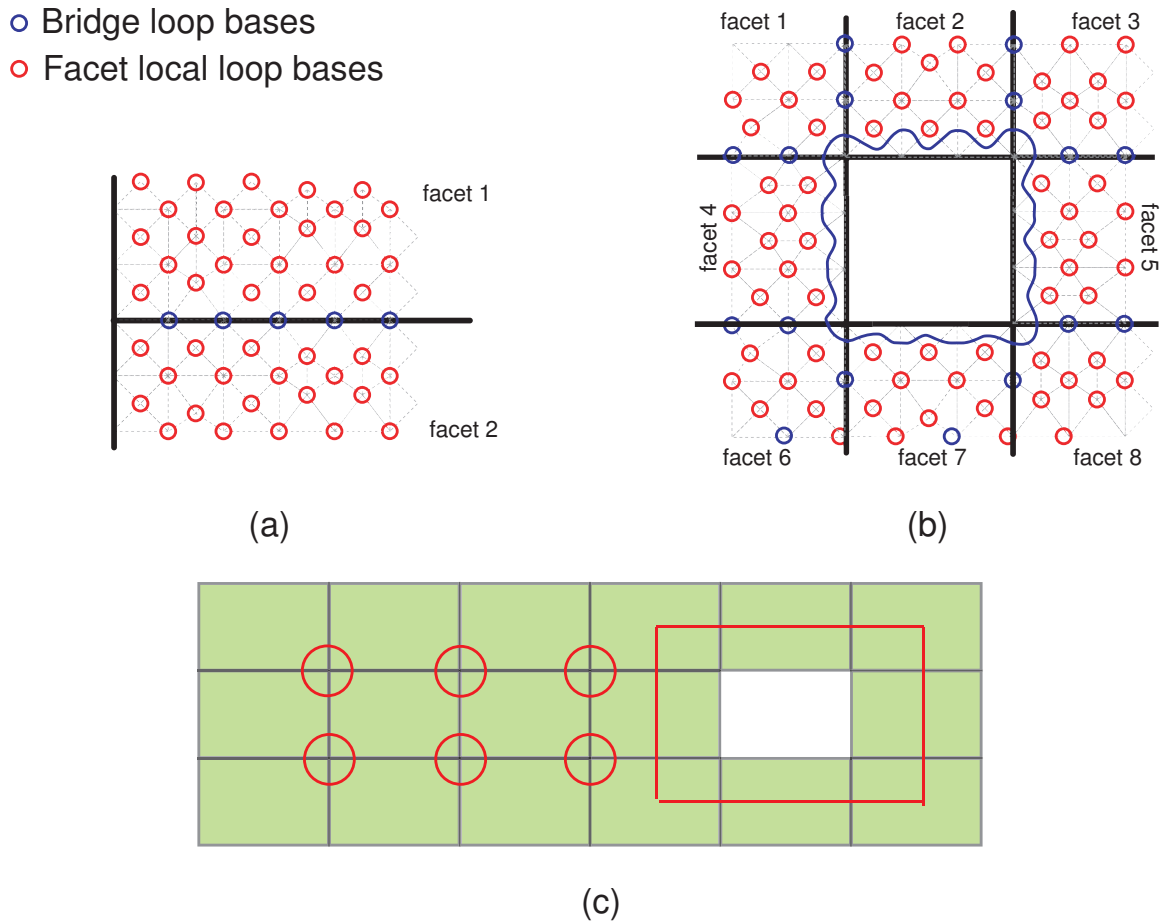


Figure 3.7: Curl conforming bridge bases. (a) Interior node based loop bridges. (b) Large loop bases representing current flowing about handle. (c) Hierarchical selection of edges and vertices from which loop bridges are formed.

interior bridge loops. If an edge is a boundary edge, then the mappings are summed into a single expansion representing a loop current segment along that edge. Following the same procedure for boundary and non-boundary vertices allows construction of the all curl conforming bases, and these bases are then stored in the current level node. A clear advantage of this method is that it readily deals with the elimination of handles due to inclusion of additional facets when forming higher level nodes and automates the formation of loop bases necessary to represent surface structures that include handles.

3.3 Cost Analysis

As mentioned at the beginning of this chapter, the purpose of introducing the MLGD description was to reduce the cost of computing and storing redundant interactions. Lets now consider the overhead associated with preparing an MLGD system for solution relative to that of a non MLGD structure.

3.3.1 Structure Storage

For a non-MLGD mesh, where all surfaces are discretized via dissimilar patches, the total memory required to store the mesh is $O(P) \propto O(N)$, where P is the total number of patches on the surface and N is the number of DOF in the system. (For a surface based implementation using first order vector expansion functions this is equal to the number of non-boundary edges, NBe, in the mesh.)

Alternatively, for an MLGD oriented graph with M upper level nodes and E edges that employs protofacets with an average of s_{avg} mesh patches, the total number of patches that can be represented by the graph structure scales as $N = (E/M)^M s$. At the same time, storing this mesh comes at a cost of $C_1 s_{\text{avg}} + C_2 E$, where C_1 the number of protofacets and C_2 is the expense of storing each edge. By substitution, the total mesh storage cost scales as $O(M \log_M(N/s))$ which is a very slow growing $O(\log N)$ algorithm.

3.3.2 Determining the Minimum Interaction Set

As described in the previous section, the minimum interaction set is determined by traversing the MLGD tree structure and comparing the interactions encountered. In the event an interaction is considered distant, based on the separation requirements of the LF-MLFMA, no further recursion into that interaction is necessary. If an interaction has already been included in the interaction list, it similarly does not need

to be recursed. By efficiently categorizing interactions by their node level, protofacet types and separation distances the search algorithm can be very efficiently performed and does not contribute significantly to simulation overhead.

3.3.3 Near and Distant Interactions

For the set of I_{near} unique near-term interactions, the mesh structure stored within one of the two associated protofacets is transformed into the global frame to perform the near-term integration. Each transform is applied only to the vertices, adding $9 v_i$ operations to the $O(1 + 9 p_i^2)$ cost of computing patch interactions via the SP bases. Here, v_i and p_i are the number of vertices and patches in the i^{th} protofacet. The total cost of computing I_{near} interactions and their related storage is thus

$$\sum_i^{I_{\text{near}}} (9 v_i + 1 + 9 p_i^2) < O(I_{\text{near}} 10 p_{\text{avg}} (1 + p_{\text{avg}})) \sim O(I_{\text{near}} p_{\text{avg}}^2). \quad (3.26)$$

Leaf level signature expansions ($\bar{\beta}$) must be formed. One benefit of the MLGD is that these expansions are formed in the local coordinate frame and thus only one is necessary for each protofacet. For an MLGD definition with P protofacets, the cost of preparing and storing the 3 vector and 1 scalar local expansions via L multipoles is

$$\sum_i^P O(L 4 p_i) \sim O(P L p_{\text{avg}}). \quad (3.27)$$

Like the near term interactions above, this set of expansions is reduced into a current-charge subset at minor additional cost.

Next, it is necessary to form the aggregation and disaggregation expansions ($\bar{\beta}$ inter-level filters) for passing up and down between graph levels. Unlike the signature expansions, these must account for vector and coordinate frame rotations. However, the MLGD again allows for a reduced number of these expansions because they relate to the edges of the oriented graph structure rather than the edges of a oct-tree struc-

ture. For an MLGD graph with G graph edges, the cost of preparing these inter-level filters is

$$\sum_i^G 9 + O(L^2) = O(G(9 + L^2)). \quad (3.28)$$

The coordinate rotation accounts for 9 additional entries of the vector Euler rotation. The I_{far} unique multipole translations ($\bar{\alpha}$) are computed and stored at a cost of

$$\sum_i^{I_{\text{far}}} 9 + O(L^2) \sim O(I_{\text{far}} L^2) \quad (3.29)$$

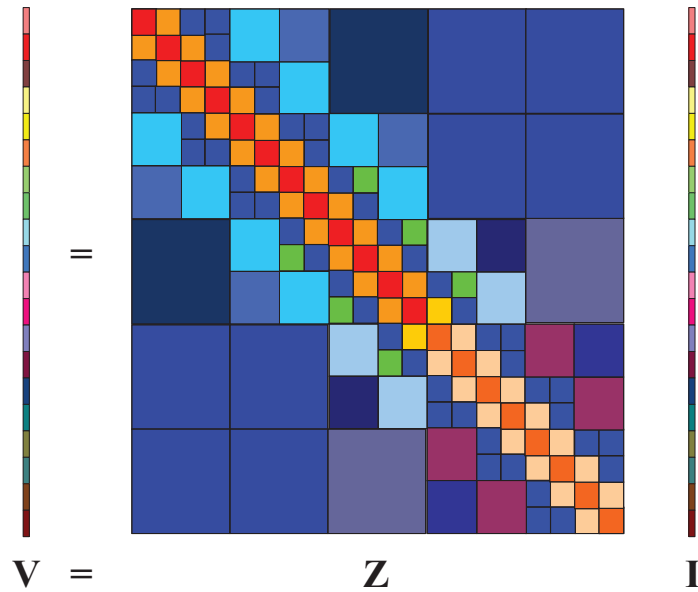
operations.

Since the total number of patches associated with the set of protofacets is generally greater than the number of unique interactions or the number of multipoles, the most expensive component of the above analysis is the $O(I_{\text{near}} p_{\text{avg}}^2)$ cost of computing the near term interactions. It is clear that the benefit of the MLGD arises from its compression of the multilevel oct-tree into an oriented graph.

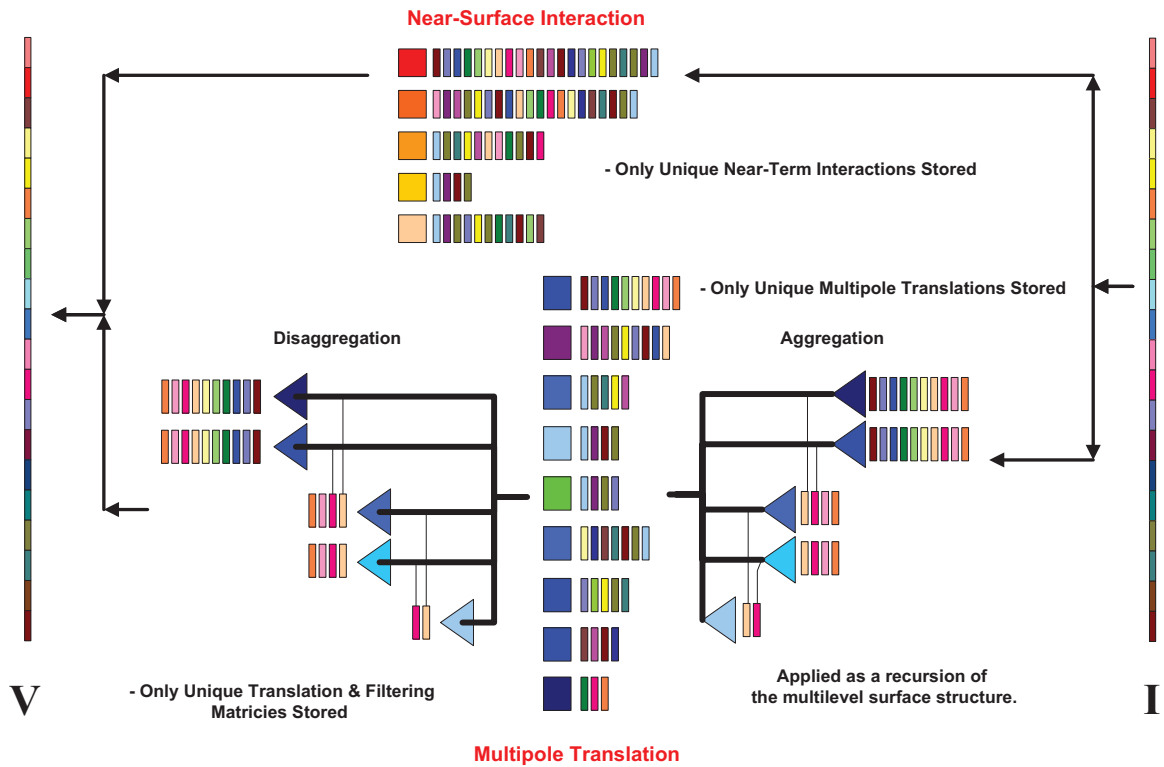
3.3.4 Overall Picture

Incorporation of the MLGD description into the numerical method can now be compared with the direct approach by observing the equivalent matrix-vector product representation. Figure 3.8(a) shows the original matrix-vector product and the associated redundant submatrices. In the equivalent MLGD form of figure 3.8(b), only the unique near-term interactions, unique aggregation and disaggregation expansions, and unique translations are pre-computed. In performing the matrix-vector product, the set of unknowns is applied, via the indexed unique interaction list, to the near-term matrices and the multilevel tree.

For the case of a geometry that contains a reasonable amount of redundancy, as most engineered geometric forms do, the MLGD allows for the simulation of larger systems in the same resource space with improved setup cost.



(a)



(b)

Figure 3.8: Original and equivalent Matrix-Vector Product (MVP). (a) Original MVP. (b) MVP after application of the MLGD and MLFMA.

CHAPTER 4

CQ Bases and the Multibasis Method

This chapter outlines the efficient assembly and fast iterative solution of the system of equations in Chapter 2 after application of the MLGD structural decomposition. However, before the system is assembled and a solution is sought, two important modifications are made to the numerical approach. First, a more efficient expansion function decomposition is defined where solenoidal and quasi-irrotational bases are mapped to a current-charge (CQ) sub-basis set. Second, the CQ sub-bases are alternatively applied in solving an overdetermined system employing multiple sets of bases. This alternative method is shown to significantly improve numerical convergence and, to the author's knowledge, represents a new approach to such problems.

4.1 Current-Charge (CQ) Expansion

The interaction matrix formed when solenoidal and quasi-irrotational bases are applied to the discretized integral equation is represented by the following linear system of equations [26]

$$\begin{bmatrix} \mathbf{V}_L \\ \mathbf{V}_C \end{bmatrix} = \begin{bmatrix} \bar{\mathbf{Z}}_{LL} & \bar{\mathbf{Z}}_{LC} \\ \bar{\mathbf{Z}}_{CL} & \bar{\mathbf{Z}}_{CC} \end{bmatrix} \begin{bmatrix} \mathbf{I}_L \\ \mathbf{I}_C \end{bmatrix}, \quad (4.1)$$

denoted henceforth as

$$\mathbf{V}_T = \bar{\mathbf{Z}}_T \mathbf{I}_T. \quad (4.2)$$

In this form, left subscripts L and C imply testing via solenoidal (loop) and non-solenoidal expansions, respectively. Similar right subscripts imply like unknown expansions. When this form is applied to a structure with handles, loop expansion functions with large domains can result. This limits the smallest cluster size that formed within the MLFMA expansion and limits its efficiency.

A well known solution to this problem relies on forming the desired expansion functions by sparse transformation with an RWG sub-basis set [34, 67]. Here, $\bar{\mathbf{Z}}_T$ is modified as

$$\bar{\mathbf{Z}}_T = \begin{bmatrix} \bar{\mathbf{T}}_C^t \\ \bar{\mathbf{T}}_L^t \end{bmatrix} \begin{bmatrix} \bar{\mathbf{Z}}_{RWG}^A + \bar{\mathbf{Z}}_{RWG}^\phi & \bar{\mathbf{Z}}_{RWG}^A \\ \bar{\mathbf{Z}}_{RWG}^A & \bar{\mathbf{Z}}_{RWG}^A \end{bmatrix} \begin{bmatrix} \bar{\mathbf{T}}_C & \bar{\mathbf{T}}_L \end{bmatrix}. \quad (4.3)$$

$\bar{\mathbf{T}}_C$ and $\bar{\mathbf{T}}_L$ are sparse transforms for the tree and loop expansion functions, respectively. $\bar{\mathbf{Z}}_{RWG}^\phi$ includes only the scalar potential interactions in triplicate for the divergence of the RWG basis and $\bar{\mathbf{Z}}_{RWG}^A$ includes only the vector potential interactions for the sub-basis RWG expansion. If LF-MLFMA is applied to the RWG sub-bases (which have small domains) the interior MVP does not run into a cluster size limitation. However, both solenoidal and non-solenoidal interactions are vector operations and two vector LF-MLFMA trees must be implemented. In the next section it is shown that alternative transforms resulting in long chains of quasi-irrotational bases are desirable for improved convergence and to permit DC simulation. This form suffers from numerical inaccuracies in these cases as the scalar and vector potential components of the non-solenoidal interaction matrix are lumped together.

In this work the following alternative form is developed

$$\bar{\mathbf{Z}}_T = \overline{\mathbf{T}}\mathbf{M}^t \bar{\mathbf{Z}}_{QCC} \overline{\mathbf{T}}\mathbf{M}, \quad (4.4)$$

where

$$\bar{\mathbf{Z}}_{QCC} = \begin{bmatrix} \bar{\mathbf{Z}}_{PP}^\phi & \bar{\mathbf{0}} & \bar{\mathbf{0}} \\ \bar{\mathbf{0}} & \bar{\mathbf{Z}}_{RWG}^A & \bar{\mathbf{Z}}_{RWG}^A \\ \bar{\mathbf{0}} & \bar{\mathbf{Z}}_{RWG}^A & \bar{\mathbf{Z}}_{RWG}^A \end{bmatrix} \quad (4.5)$$

and

$$\bar{\mathbf{T}}\mathbf{M} = \begin{bmatrix} \bar{\mathbf{T}}_Q & \bar{\mathbf{0}} \\ \bar{\mathbf{T}}_{CC} & \bar{\mathbf{0}} \\ \bar{\mathbf{0}} & \bar{\mathbf{T}}_{CL} \end{bmatrix}. \quad (4.6)$$

The first column sparse mappings $\bar{\mathbf{T}}_Q$ and $\bar{\mathbf{T}}_{CC}$ together represent divergence conforming bases. In the case of an RWG or tree basis, the associated column of $\bar{\mathbf{T}}_Q$ maps positive (+1) and negative (-1) surface charges and the same column of $\bar{\mathbf{T}}_{CC}$ maps one properly oriented RWG vector potential sub-basis. Since solenoidal bases have no associated charge, the $\bar{\mathbf{T}}_{CL}$ sparse transform maps only groups of RWG vector potential sub-bases. Solenoidal basis scaling is applied to the mapping $\bar{\mathbf{T}}_{CL} = \bar{\mathbf{T}}_{CL}/k$. Scalar interactions are performed via Patch-Patch collocation $\bar{\mathbf{Z}}_{PP}^\phi$, equivalent to that used in solving the electrostatic problem. Vector potential interactions are applied through the same $\bar{\mathbf{Z}}_{RWG}^A$ for both solenoidal and quasi-irrotational currents, which for solenoidal bases is equivalent to that used in eddy-current simulation. Using this interior product it is possible to simulate both electrostatic and eddy-current problems.

Through observation of $\bar{\mathbf{Z}}_{QCC}$, the MVP can be simplified. First, the sub-basis unknowns are defined

$$\mathbf{I}_{QCC} = \begin{bmatrix} \mathbf{Q} \\ \mathbf{I}_{QIR} \\ \mathbf{I}_{SOL} \end{bmatrix}, \quad (4.7)$$

with \mathbf{Q} being surface charge coefficients, \mathbf{I}_{QIR} being quasi-irrotational current coeffi-

icients, and \mathbf{I}_{SOL} being solenoidal current coefficients. Next, sub-basis potentials

$$\mathbf{V}_{QCC} = \begin{bmatrix} \mathbf{V}_Q \\ \mathbf{V}_{QIR} \\ \mathbf{V}_{SOL} \end{bmatrix}, \quad (4.8)$$

are defined with similar relations. These two components relate to the interior sub-basis interaction as

$$\mathbf{V}_{QCC} = \overline{\mathbf{Z}}_{QCC} \mathbf{I}_{QCC}, \quad (4.9)$$

and are related to the higher level bases via the sparse transforms

$$\mathbf{I}_{QCC} = \overline{\mathbf{T}}\mathbf{M} \mathbf{I}_T \quad (4.10)$$

$$\mathbf{V}_T = \overline{\mathbf{T}}\mathbf{M}^t \mathbf{V}_{QCC}. \quad (4.11)$$

By taking advantage of the symmetry in the matrix $\overline{\mathbf{Z}}_{QCC}$, only a single application of the vector and scalar potential interactions is required in performing the matrix-vector product of (4.9),

$$\mathbf{V}_Q = \overline{\mathbf{Z}}_{PP}^\phi \mathbf{Q} \quad (4.12)$$

$$\mathbf{V}_{QIR} = \overline{\mathbf{Z}}_{RWG}^A (\mathbf{I}_{QIR} + \mathbf{I}_{SOL}) \quad (4.13)$$

$$\mathbf{V}_{SOL} = \mathbf{V}_{QIR}. \quad (4.14)$$

This sub-basis interaction is clearly that of a current-charge (CQ) expansion. The scalar and vector components of the interactions are fully decoupled and the vector potential product is the same for both the solenoidal and quasi-irrotational currents. The matrix-vector product is performed using one vector and one scalar LF-MLFMA tree, and only a single vector disaggregation is employed.

Other mixed potential approaches employing current-charge expansions in the

solution of the EFIE have been proposed [68, 69], but the direct relationship between this implementation and the standard RWG and loop-tree formulations makes this approach simpler to implement.

4.2 Preconditioning Methods

The application of an incomplete Helmholtz decomposition by a change of bases suffices to eliminate the “low frequency” breakdown of the EFIE formulation. However, the matrices that arise for solenoidal bases are generally very well conditioned, the non-solenoidal (quasi-irrotational) expansion results in an ill-conditioned system of equations. The LT decomposition makes the solution of a highly discretized problem possible, it does not make its solution by application of an iterative solver practicable for large structures. To improve the convergence of such systems a number of preconditioning methods have been proposed, and are outlined below. These methods can be expensive and are not entirely compatible with the MLGD approach. Here, a new method for the solution of these types of systems is introduced, the Multibasis (MB) method.

4.2.1 Diagonal Preconditioning

Diagonal preconditioning (DP) is a self-term method. Similar to other near-neighbor conditioning methods, DP helps to reduce the condition number of the matrix by acting to equalize strong contributions from self-terms and to model the localized interactions of strong evanescent modes [34]. DP is beneficial in LT forms as it properly weights the matrix coefficients and is simply formed as

$$\overline{\mathbf{P}}_D = \text{diag}(\overline{\mathbf{Z}}_T)^{-1} \quad (4.15)$$

and applied to the MVP

$$\mathbf{V}_T = \overline{\mathbf{P}}_D \overline{\mathbf{T}}\mathbf{M}^t \mathbf{V}_{QQS}. \quad (4.16)$$

However, DP and other near-neighbor preconditioners do not model strong off diagonal coupling and thus fail to aid on structures where such occur. Furthermore DP does not influence spectral resolution [28] and cannot remedy bases that fail to efficiently represent eigenvectors in eigenvalue decomposition of the interaction [70]. Both of these issues arise when using Loop-Tree expansions.

4.2.2 Tree Basis Rearrangement

One method of improving the quasi-irrotational conditioning is known as tree basis rearrangement (TBR) [26]. In TBR, transforms are applied to the tree expansion in the loop-tree form, resulting in a change of basis for the non-solenoidal expansion terms. The new TBR bases are long chains of tree bases organized such that they all have a common root (starting patch) [71], as shown in figure 4.1(a). In these chains, all self term scalar contributions cancel except for those at the ends of the chain. (These bases can be thought of as meandering lines of current, where charge accumulates only at the ends of each segment.) As mentioned in discussing the second form of the sub-basis interaction in the last section, when the $\overline{\mathbf{Z}}_{RWG}^\phi$ entries are added to those of the $\overline{\mathbf{Z}}_{RWG}^A$ matrix in the upper left component of the RWG interaction, scalar contributions in the middle of the chain cannot cancel completely due to numerical precision. This basis rearrangement was first proposed [26] by application of the sparse transformation but can be more easily assembled as shown in figure 4.1 using the CQ sub-basis expansion and associated sparse mappings.

The benefits of the TBR are as follows. At DC, only the scalar contributions at the ends of the chains remain, and since all share a common root, the TBR is capable of representing a static charge distribution on the surface. Furthermore, the TBR

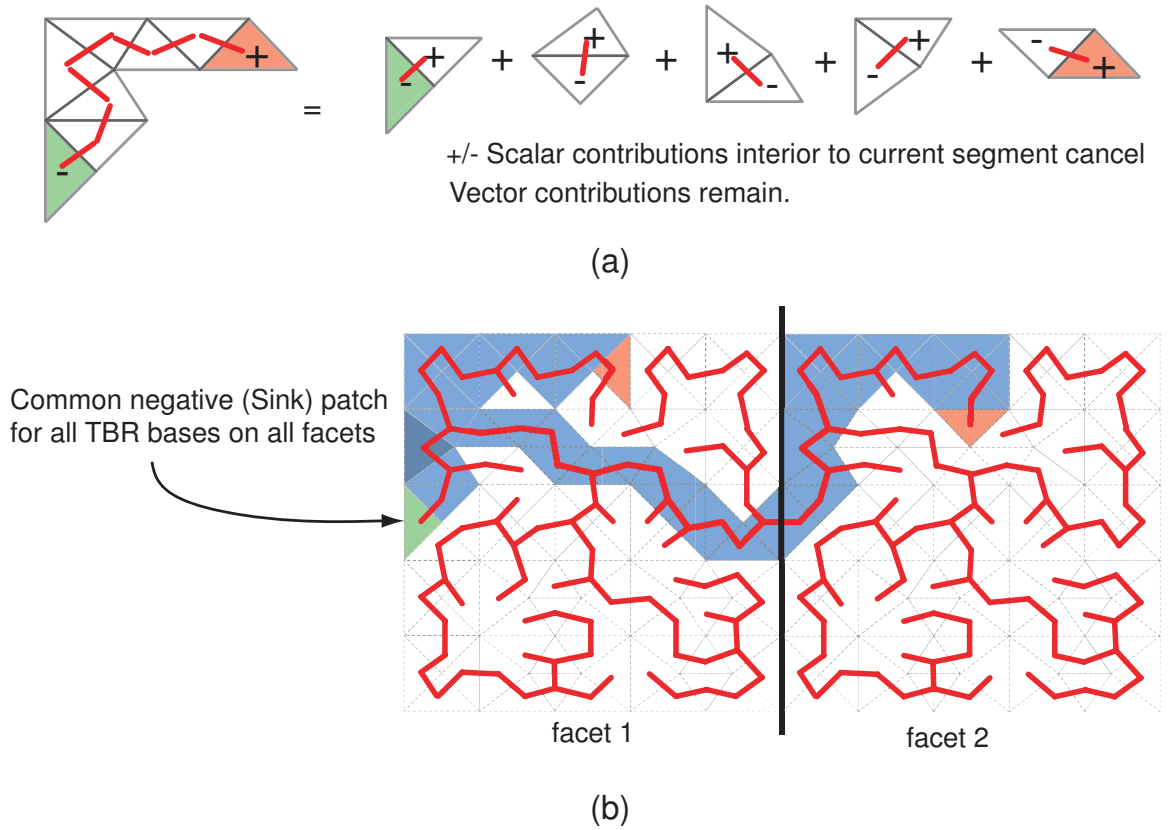


Figure 4.1: Tree-Basis Rearrangement (TBR) equivalent bases. (a) TBR CQ composition. (b) TBR bases bridging adjacent facets.

has dynamic spectral resolution because of its varying spatial resolution (some TBR bases are nearly entire domain functions, while others only traverse a small subset of patches). As discussed in the next section, dynamic spatial and thus spectral resolution provides improved convergence.

Sadly, TBR bases are impractical in an MLGD setting. Mappings involving disjoint sub-basis sets on different facets are possible, but since the resulting bases traverse multiple facets, application of the MLGD does not decrease storage or overhead for basis transforms. The resulting basis function mappings are proportional to the number of tree bases in the entire system, which is $O(N)$, but each transformation requires the superposition of large numbers of sub-bases twice per iteration.

4.2.3 Multiresolution (MR) Method

A more recent advancement in non-solenoidal conditioning is the implementation of Multiresolution (MR) schemes [27–29]. In this approach, bases are organized into levels with increasing spatial resolution. Higher level bases (with lower spatial resolution) are linear combinations of lower level (with higher spatial resolution) expansion functions. The set of bases at each resolution is complete and allows for a solution of the integral equation at any level. Some methods compress all levels into a single MR basis definition via sparse transforms (mappings) used to interrelate the higher and lower level bases [29]. Since the resulting MR bases contain a large range of spatial resolution (like TBR) the diagonal values of the resulting matrix closely resemble the eigenvalues of the matrix equation [28, 70] (after diagonal preconditioning). Since the MR expansion bases more closely represents the eigenvectors of the system, a highly convergent matrix equation results. This approach results in solution times that are better than the TBR form, but are not necessarily applicable in the electrostatic case.

Like TBR, MR bases are formed as a assembly of large numbers of expansion functions at the lowest level of the MR structure. However, unlike TBR the cost of performing this mapping is $O(N \log N)$ [29] because of the hierarchial structure used. In addition, depending on the implementation, fine meshes that increase the number of unknowns well beyond that necessary for a given geometric representation have frequently been used as a method of forming the hierarchy [29]. Recent modifications to this method form higher level bases by linear combination of RWG bases at the mesh level [27], doing away with the need for a multilevel (multigrid) mesh. However, just like the TBR, MR based on RWG sub-bases may incur numerical inaccuracy at low frequencies if the scalar potential components of the self term interactions are added to those of the vector potential prior to application of the transform, so care must be taken in this regard.

4.3 The Multibasis (MB) Method

In an effort to find a preconditioner that is more compatible with the MLGD (i.e. one that relies entirely on bases with small domains) and is less expensive than the methods discussed above, the Multibasis (MB) method is now developed. Unlike the previous approaches, the MB method does not require the formation of a linearly independent set of expansion functions with diverse spatial resolution in order to improve convergence. Instead, improved convergence comes from the solution of an over determined system utilizing multiple sets of overlapping bases with similar spatial (and thus spectral) resolution.

Premise of the MB Method

Consider the current distribution found on a dense mesh discretizing a PEC object and illuminated by an exterior impressed field. First, choose to determine the mesh currents by solution of the linear system formed by LT expansion and Galerkin testing. It is assumed that this implementation is capable of representing the solution and that the cost of solving the system is acceptable. Next, an equivalent current distribution (to within the tolerance of the chosen iterative solver) may be determined if LTBR (Loop-Tree Basis Rearrangement) is applied under the same criteria. Given the option, one generally chooses to apply the higher level bases that result in minimum total solution time. However, let's consider these mesh current distributions in terms of the CQ subset of partial expansion functions.

Both the LT and LTBR solutions above will have identical current and charge on the mesh surface and there exists a set of CQ coefficients that minimize the residual of both LT and LTBR forms. Essentially, the solution to the linear system in terms of the CQ subset will be a minima for all higher level sets built from the CQ subset. It is not the LT or LTBR coefficients that are sought, but the CQ coefficients that minimize both the LT and LTBR residuals. This is the premise of the MB method,

to apply multiple upper level expansions in finding the sub-basis coefficients that minimize the upper level error.

The MB method is not limited to LT and LTBR, but is applicable for any group of higher level expansions, including sets with similar spatial resolution. While some expansions can support a correct answer, they do not converge or converge an incorrect answer (e.g. RWG bases at low frequencies). Others are convergent, but only reach the solution only after a large number of iterations (e.g. LT/LS bases). In both cases, these basis sets share a common CQ solution set, and by computing their common residuals and properly updating the associated CQ unknowns, the collective subspace is better behaved than that of the individual expansions.

Failure of the Direct Approach

The goal of the MB method is to apply multiple sets of bases to the same surface, resulting in a single system of equations. However, direct formulation will result in an over determined system of equations. For example, consider the higher level interaction matrix resulting from application of an RWG set $\overline{\mathbf{T}}_{\text{RWG}}$ in conjunction with a loop-tree basis set $\overline{\mathbf{T}}_{\text{LT}}$

$$\overline{\mathbf{T}}_{\text{RWG}} = \begin{bmatrix} \overline{\mathbf{T}}_Q \\ \overline{\mathbf{T}}_{C_C} \\ \overline{\mathbf{0}} \end{bmatrix}, \quad \overline{\mathbf{T}}_{\text{LT}} = \begin{bmatrix} \overline{\mathbf{T}}_{Q_i} & \overline{\mathbf{0}} \\ \overline{\mathbf{T}}_{C_C i} & \overline{\mathbf{0}} \\ \overline{\mathbf{0}} & \overline{\mathbf{T}}_{C_L} \end{bmatrix}, \quad (4.17)$$

where the i^{th} charge and vector potential mappings in the LT transform are a subset of those in the RWG mapping. The resulting expanded matrix is

$$\begin{aligned}\bar{\mathbf{Z}}_T &= [\overline{\mathbf{T}}\mathbf{M}_{\text{RWG}} \overline{\mathbf{T}}\mathbf{M}_{\text{LT}}]^t \bar{\mathbf{Z}}_{QCC} [\overline{\mathbf{T}}\mathbf{M}_{\text{RWG}} \overline{\mathbf{T}}\mathbf{M}_{\text{LT}}] \\ &= \begin{bmatrix} \overline{\mathbf{T}}\mathbf{M}_{\text{RWG}}^t \bar{\mathbf{Z}}_{QCC} \overline{\mathbf{T}}\mathbf{M}_{\text{RWG}} & \overline{\mathbf{T}}\mathbf{M}_{\text{RWG}}^t \bar{\mathbf{Z}}_{QCC} \overline{\mathbf{T}}\mathbf{M}_{\text{LT}} \\ \overline{\mathbf{T}}\mathbf{M}_{\text{LT}}^t \bar{\mathbf{Z}}_{QCC} \overline{\mathbf{T}}\mathbf{M}_{\text{RWG}} & \overline{\mathbf{T}}\mathbf{M}_{\text{LT}}^t \bar{\mathbf{Z}}_{QCC} \overline{\mathbf{T}}\mathbf{M}_{\text{LT}} \end{bmatrix}\end{aligned}\quad (4.18)$$

with the upper left system

$$\begin{bmatrix} \overline{\mathbf{T}}_Q^t \bar{\mathbf{Z}}_{PP}^\phi \overline{\mathbf{T}}_Q & \bar{\mathbf{0}} & \bar{\mathbf{0}} \\ \bar{\mathbf{0}} & \overline{\mathbf{T}}_{C_C}^t \bar{\mathbf{Z}}_{RWG}^A \overline{\mathbf{T}}_{C_C} & \bar{\mathbf{0}} \\ \bar{\mathbf{0}} & \bar{\mathbf{0}} & \bar{\mathbf{0}} \end{bmatrix}\quad (4.19)$$

and the upper right system

$$\begin{bmatrix} \overline{\mathbf{T}}_Q^t \bar{\mathbf{Z}}_{PP}^\phi \overline{\mathbf{T}}_{Q_i} & \bar{\mathbf{0}} & \bar{\mathbf{0}} \\ \bar{\mathbf{0}} & \overline{\mathbf{T}}_{C_C}^t \bar{\mathbf{Z}}_{RWG}^A \overline{\mathbf{T}}_{C_{C_i}} & \overline{\mathbf{T}}_{C_C}^t \bar{\mathbf{Z}}_{RWG}^A \overline{\mathbf{T}}_{C_L} \\ \bar{\mathbf{0}} & \bar{\mathbf{0}} & \bar{\mathbf{0}} \end{bmatrix}.\quad (4.20)$$

Here the i^{th} bases are identical and the off diagonal entries in the upper right system are equal to the i^{th} entries along the matrix diagonal,

$$\overline{\mathbf{T}}_Q^t \bar{\mathbf{Z}}_{PP}^\phi \overline{\mathbf{T}}_Q(:, i) = \overline{\mathbf{T}}_Q^t \bar{\mathbf{Z}}_{PP}^\phi \overline{\mathbf{T}}_{Q_i}\quad (4.21)$$

$$\overline{\mathbf{T}}_{C_C}^t \bar{\mathbf{Z}}_{RWG}^A \overline{\mathbf{T}}_{C_C}(:, i) = \overline{\mathbf{T}}_{C_C}^t \bar{\mathbf{Z}}_{RWG}^A \overline{\mathbf{T}}_{C_{C_i}}.\quad (4.22)$$

With large equivalent entries introduced off diagonal, zero eigenvalues arises in the system of equations implying a rank deficient over determined set of equations.

In order to apply multiple sets of overlapping bases to the same surface, a departure from the standard approach to the application of the matrix-vector product in

the iterative solver is necessary.

Matrix Vector Product Redefined

By transferring the interaction to the common subset of CQ expansions, the over determined system can be efficiently solved. Note that the set of unknown CQ coefficients, \mathbf{I}_{QCC} , is mapped from the upper level expansion coefficients \mathbf{I}_T via $\overline{\mathbf{T}\mathbf{M}}$ and the sub-basis potentials, \mathbf{V}_{QCC} , map to the set of upper level potentials \mathbf{V}_T via $\overline{\mathbf{T}\mathbf{M}}^t$. Furthermore, the interaction at the sub-basis level is not over determined since each CQ basis is only interacted once. The following procedure works in solving the over determined system (see figure 4.2).

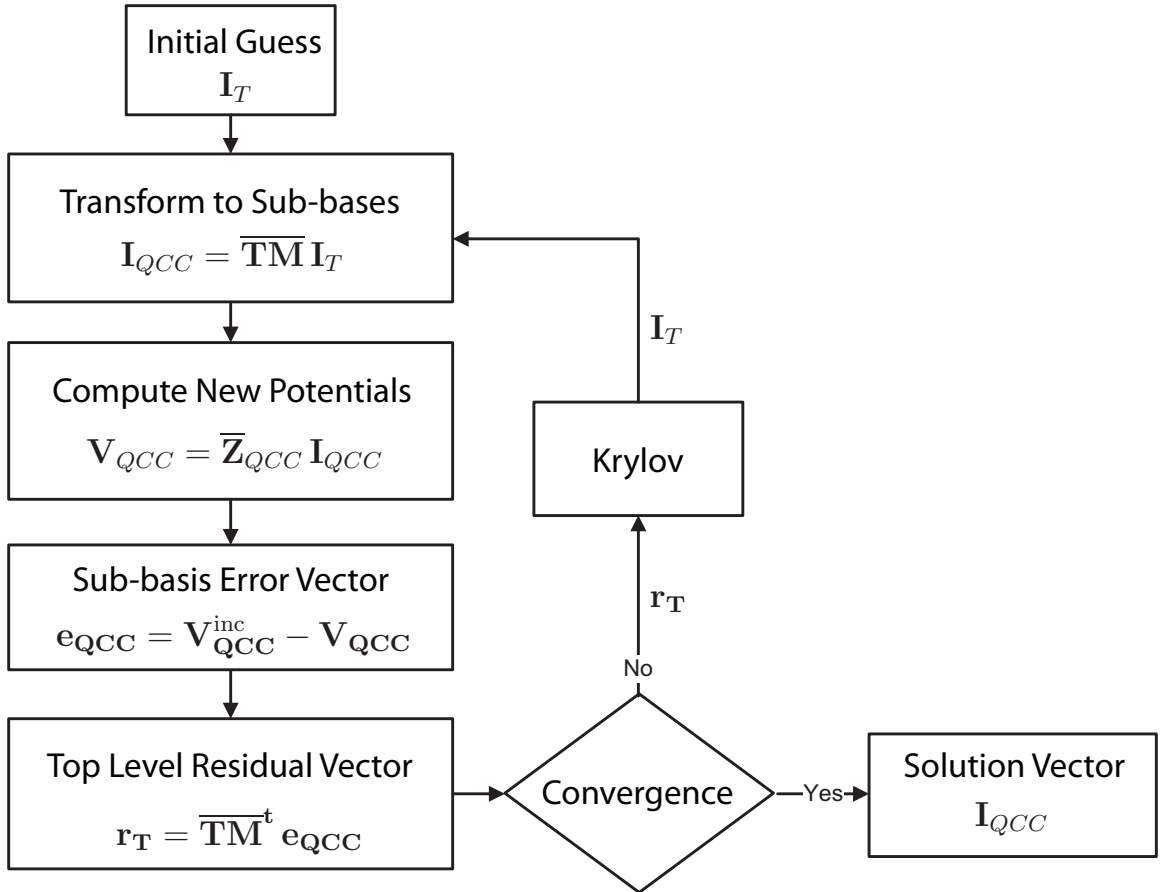


Figure 4.2: Multibasis (MB) iterative procedure. Applying top level residuals to determine a sub-basis solution set.

1. The potentials representing the proper solution $\mathbf{V}_{\text{QCC}}^{\text{inc}}$ are computed at the sub-basis level.
2. An initial guess for the top level expansion coefficient vector, \mathbf{I}_T , is formed
3. \mathbf{I}_T is passed down to the sub-basis \mathbf{I}_{QCC} via $\overline{\mathbf{TM}}$.
4. The matrix vector product is performed to determine the resulting sub-basis potentials $\mathbf{V}_{\text{QCC}} = \overline{\mathbf{Z}}_{\text{QCC}} \mathbf{I}_{\text{QCC}}$.
5. The difference between \mathbf{V}_{QCC} and $\mathbf{V}_{\text{QCC}}^{\text{inc}}$ is the sub-basis error vector

$$\mathbf{e}_{\text{QCC}} = \mathbf{V}_{\text{QCC}}^{\text{inc}} - \mathbf{V}_{\text{QCC}}. \quad (4.23)$$

6. This error is mapped to the upper level to form the residual vector at the top level

$$\mathbf{r}_T = \overline{\mathbf{TM}}^t \mathbf{e}_{\text{QCC}} \quad (4.24)$$

and convergence is met when $\|\mathbf{r}_T\|_2 \leq \epsilon$.

If the error is within the desired tolerance, ϵ , for all higher level bases, then the iterative procedure ends. Otherwise, the residual is used to form a new guess at \mathbf{I}_T , and the procedure is repeated from 3). It is important to note that $\overline{\mathbf{TM}}$ is not 1-to-1 unitary or invertible, and thus this method of passing down unknowns and passing up potentials is direction specific.

If the transformation matrix includes more than a single set of top level expansion functions, $\overline{\mathbf{TM}} = [\overline{\mathbf{TM}}_{\text{RWG}} \overline{\mathbf{TM}}_{\text{LT}}]$ for example, the resulting sub-basis current distribution is a proper solution to both of these expansions. Furthermore, since multiple sets of bases are used in computing the residual for each iterate, the search space to be traversed is improved since the collective solution spaces all share a single common minima. Put differently, the disjoint sets help to refine the direction of steepest de-

cent and the common minima shared between the bases is exploited leading to faster convergence of the iterative method.

Unlike TBR or MR expansions, which employ dynamic spatial and thus spectral resolution via basis transformation, the MB does not diversify resolution to better represent the search space, rather it alters the search space itself. Also, as the cost of including additional transforms is $O(N)$, application of this method does not alter the low frequency $O(N)$ methods used in performing the MVP.

Two other key advantages are gained with this procedure. The first is increased confidence in the solution. Not only is the solution a minima for those expansions employed during iteration, but if a particular top-level expansion was not used, its residual can simply be evaluated from final error vector \mathbf{e}_{QCC} in low $O(N)$ time. The second key advantage of this method is that it can result in a more robust implementation. For example, if one or more of the top level basis sets is incomplete (eg. Loop basis formation missed a handle), the existence of the other expansions may rain in the iterative method and the solution can still be correct.

Further Items of Note It is not possible to inexpensively change expansions actively during iteration. For example consider the cost of equating the subbases unknown vector \mathbf{I}_{QCC} computed using $\overline{\mathbf{TM}_1}$ to an identical subbases resulting from a different mapping $\overline{\mathbf{TM}_2}$;

$$\mathbf{I}_{QCC} = \overline{\mathbf{TM}_1} \mathbf{I}_{T_1} = \overline{\mathbf{TM}_2} \mathbf{I}_{T_2} \quad (4.25)$$

Solving this equation in terms of the top level set \mathbf{I}_{T_2} , we arrive at

$$\mathbf{I}_{T_2} = \left(\overline{\mathbf{TM}_2}^t \overline{\mathbf{TM}_2} \right)^{-1} \overline{\mathbf{TM}_1} \mathbf{I}_{T_1} \quad (4.26)$$

after multiplying through by $\overline{\mathbf{T}\mathbf{M}^2}^t$. While the matrix $(\overline{\mathbf{T}\mathbf{M}_2}^t \overline{\mathbf{T}\mathbf{M}_2})$ is well conditioned its inverse is full rank, making a change of basis an $O(N^2)$ operation.

Also, the application of a diagonal preconditioner is necessary to efficiently weight the expansion. The diagonal preconditioner,

$$\overline{\mathbf{P}} = \text{diag}\left(\overline{\mathbf{T}\mathbf{M}^t} \overline{\mathbf{Z}}_{QQS} \overline{\mathbf{T}\mathbf{M}}\right)^{-1} \quad (4.27)$$

may be included in the basis compression step

$$\mathbf{V}_T = \overline{\mathbf{P}} \overline{\mathbf{T}\mathbf{M}^t} \mathbf{V}_{QQS}. \quad (4.28)$$

Alternatively, since only the diagonal of $(\overline{\mathbf{T}\mathbf{M}^t} \overline{\mathbf{Z}}_{QQS} \overline{\mathbf{T}\mathbf{M}})$ is needed, it can be more efficiently formed via

$$\text{diag}\left(\overline{\mathbf{T}\mathbf{M}^t} \overline{\mathbf{Z}}_{QQS} \overline{\mathbf{T}\mathbf{M}}\right)^{-1} = \text{diag}\left(\overline{\mathbf{T}\mathbf{M}^t} \cdot \overline{\mathbf{T}\mathbf{M}}\right)^{-1} \text{diag}\left(\overline{\mathbf{Z}}_{QQS}\right)^{-1}. \quad (4.29)$$

4.4 Cost Analysis

In this chapter the preferred use of a CQ sub-basis expansion was outlined and applied in the formation of the more MLGD friendly MB iterative approach. It is important that the cost of implementing both these sub-bases and the iterative procedure be examined. The diagram of figure 4.3 shows the overall numerical procedure used in setting up and solving the linear system of equations for a given surface structure.

4.4.1 Sub-basis Matrix Assembly and Storage

Assembly of the CQ sub-basis interactions, $\overline{\mathbf{Z}}_{PP}^\phi$ and $\overline{\mathbf{Z}}_{RWG}^A$, and their multipole signature function counterparts comes at a reduced cost relative to the use of an

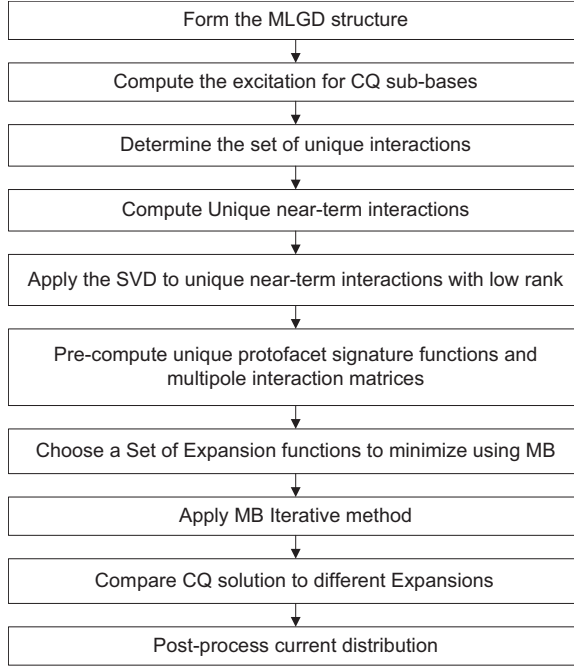


Figure 4.3: Numerical method overview.

RWG sub-basis interaction (when both are transformed from the single-patch SP interactions of the second chapter). RWG expansions are the superposition of both the scalar and vector interactions between pairs of SP bases (2.70), requiring mappings with $2N_{Be} + 2P$ entries. Alternatively, the CQ sub-bases require superposition of only vector potential SP interaction pairs, thus requiring a mapping with only $2 N_{Be}$ entries (the $\bar{\mathbf{Z}}_{PP}^\phi$ interaction is used as is). The resulting near-term interactions of CQ bases require less storage because the number of patches is always less than the number of non-boundary edges.

4.4.2 Applying Basis Transformations

When the CQ basis subset is applied, the number of transformation matrix entries required to map curl-conforming loop bases is the same as that necessary when and RWG subset is applied. However, divergence conforming bases require additional entries to include the positive and negative charges at their ends. Applying a mapping

between the CQ subset and a divergence conforming superset requires 2 additional operations per expansion.

Within the iterative procedure, basis transformations are applied twice, first to pass down the current distribution and then to pass up the resulting potential error vector. The added cost of the CQ transformation relative to that of an RWG sub-basis expansion is $4N$ added operations per iterate. If more than a single upper level expansion is applied to improve convergence, then the number of additional operations scales at $O(K4N)$, where K is the number of complete upper level expansion sets.

CHAPTER 5

Test and Measurement

The preceding chapters outlined the formulation and implementation of an efficient integral equation solver. However, the goal of this work is not only the implementation of such a tool but also its verification and application. To ensure that simulations correlate with real world phenomena, it is necessary to compare simulated results to measured data. However, making such measurements requires an advanced understanding of low frequency electromagnetic field behavior, the design and limitations of measurement probes, and most importantly the measurement setup that must be used. This chapter discusses these issues and outlines what is required to ensure reliable measurements are obtained.

5.1 Field Behavior

The low frequency electromagnetic fields generated by a solitary loop antenna are equivalent to those of an infinitesimal magnetic (or Fitzgerald) dipole [37] when observed at 5 or more radii from the source [72]. The dividing line between radiating and non-radiating field regions occurs at $r = \lambda_0/2\pi$, where r is the radial distance from the antenna and λ_0 is the free-space wavelength. Interior to this boundary the $1/r^3$ inductive terms are dominant and result in a rate of field decay on the order of

60 dB/decade. Beyond this boundary the $1/r$ radiative terms dominate.

In the case of a 125 kHz LFID initiating coil ($\lambda_0 = 2400$ m), the free-space near-field to far-field dividing line occurs at 382 meters from the source. Coupling between tags and interrogators in this frequency range occurs entirely within the inductive field region. Thus, it is the effect of materials placed within this region that must be investigated. Detailed analysis of these effects for arbitrarily shaped objects will require application of the aforementioned numerical method. However, the magnetic field of a loop source near a PEC wall, formulated by standard Image Theory [37], provides adequate insight into field behavior in this region. In figure 5.1, the magnetic

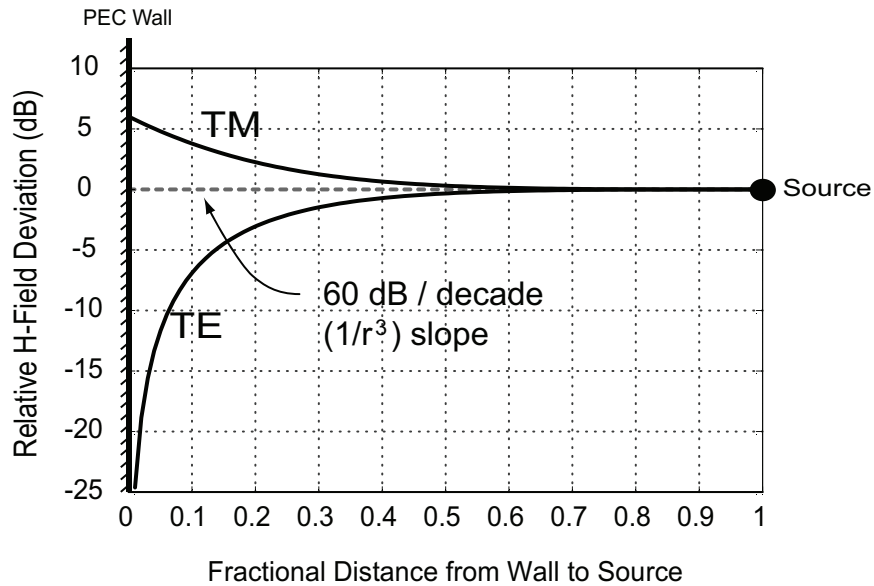


Figure 5.1: Change in magnetic field near a PEC wall. H-field for TE (transverse electric) and TM (transverse magnetic) loop source polarization.

field in the presence of a PEC wall relative to that in free space is plotted. When the loop is oriented with its axis normal to the wall (transverse electric) the currents formed on the wall generate fields in opposition to the excitation and the total normal magnetic field decays exponentially approaching the interface. Alternatively, when the loop axis is tangential (transverse magnetic), wall currents produce additive fields and double the total magnetic field at the interface.

5.2 Loop Antennas

It is evident that the field of interest will be highly variable. In order to measure fields and operate LFID systems under these conditions it is necessary to optimize tag (or sensor) sensitivity as well as obtain a clear understanding of coupling between receiving loops, their images, and an interrogating source.

5.2.1 Magnetic Field Coupling

Initiating (transmitting) coils used in RFID systems are typically installed in the absence of the tags to which they communicate and are driven using a fixed voltage source. Because of near-field coupling, the current in the transmitting coil will change as tags couple to it. It is necessary to determine received voltage at the tag including this variation because the current in the transmitting coil is not re-measured as each tag is included.

To determine this value a number of assumptions can be made. The coupling between the transmitting and receiving coils can be represented by a reactive mutual-impedance

$$Z_{ij} \sim j \omega L_{ij}, \quad (5.1)$$

where the mutual resistance and capacitance values are assumed to be negligible. The loop mutual inductance is

$$L_{ij} = \frac{\Phi_{ij}}{I_{jj}}, \quad (5.2)$$

where I_{jj} is the current in the j^{th} loop and Φ_{ij} the flux passing through loop i generated by loop j . The self-impedance ($Z_{ij} |_{i=j}$) of a small loop is dominated by its reactive self-inductance and ac resistance, with radiation losses playing an insignificant role. Via Faraday's Law, the open circuit voltage at the receiving antenna

in the presence of N other loops can be approximated by

$$V_{Li} = \frac{V_{ii}}{Z_{iD}} Z_{Li}, \quad (5.3)$$

where higher order coupling between secondary loops is neglected. The first order driving impedance of the i^{th} loop in terms of j other loops is

$$Z_{iD} = Z_{ii} + Z_{Li} - \sum_{j \neq i}^N \frac{Z_{ij}^2}{Z_{jj} + Z_{Lj}}, \quad (5.4)$$

and the initial open circuit voltage induced in the loop is

$$V_{ii} = -j\omega \sum_{j \neq i}^N \mathbf{L}_{ij} I_{jj}^{\text{orig}}. \quad (5.5)$$

I_{jj}^{orig} is the j^{th} transmitting coil current prior to introduction of the receiving coil, i .

In the case of a single transmitting and receiving pair

$$V_{L1} = \frac{Z_{L1}}{Z_{11} + Z_{L1} - \left(\frac{Z_{12}^2}{Z_{22} + Z_{L2}} \right)} V_{11}. \quad (5.6)$$

If $(Z_{11} + Z_{L1})(Z_{22} + Z_{L2}) \gg Z_{12}^2$ the received voltage is independent of the self impedance of the transmitting loop. This is generally the case for RFID systems and the received voltage via

$$V_{Li} = V_{ii} \frac{Z_{Li}}{Z_{ii} + Z_{Li}} \quad (5.7)$$

is commonly assumed. While these equations are derived for an antenna pair, they are equally applicable in the case of coupling between a loop and any set of currents formed in a nearby material.

5.2.2 Receiving Loop Sensitivity

The goal of designing any antenna is optimizing its sensitivity across the necessary operating bandwidth. Sensitivity can be defined in terms of either voltage or power. In a situation where the load impedance is fixed, then the voltage sensitivity of the antenna is a sufficient figure of merit. However, if the load impedance can be adjusted then it is beneficial to employ power sensitivity in selecting the proper loading mechanism.

Magnetic field power sensitivity is equal to the ratio between the power delivered to the load and the field density at the sensor location. When the voltage divider of (5.7) is an appropriate approximation, then coil power sensitivity is

$$S_m = \frac{P_L}{(A/m)^2} = \left| \frac{(V_L)^2}{Z_L H^2} \right| = \left| \frac{V_{\text{emf}}^2 Z_L}{H^2 (Z_{11} + Z_L)^2} \right| = (\omega \mu A N)^2 \frac{Z_L}{(Z_{11} + Z_L)^2}. \quad (5.8)$$

The leading terms of this form, ω , μ , A , and N are the radian frequency, the loading permeability, the loop area, and the number of loop turns, all of which are physical parameters relating to the selection of the proper coil. Only the latter terms serve in selecting the proper load impedance for the sensor.

It is first assumed that the antenna is not operated at its own self resonance, but that the impedance of the coil is dominated by its self inductance and resistive loss $Z_{11} = R_a + j\omega L_a$. If the antenna were operated at self resonance then minor changes in its environment could significantly shift the resonant point. Unlike a coil that is resonated out by means of a lumped element capacitor, a coil that is self-resonant relies on the capacitance between its windings to set the resonant frequency. If this sensor is placed near a dielectric object its capacitance will change and the resonant frequency will drift. This makes the coil less reliable as both a measurement device and an LFID tag.

Broadband Detection If it is desirable that the antenna operate with a large bandwidth, then a resistive loading is selected. This also reduces the coupling between the coil and any other current, and raises the critical frequency of the output voltage divider (causing the loop sensor to remain proportional to the derivative of the average magnetic field passing through the loop). Such a load linearly degrades the sensitivity of the sensor

$$S_m^B = \frac{(\omega\mu AN)^2}{R_L} \quad (5.9)$$

proportional to the magnitude of the load impedance selected (assuming $R_L \gg R_a$).

Narrow-Band Detection For narrow-band applications, strong coupling and greater sensitivity are found by conjugate matching the antenna at the operating frequency. For a resonated receiving coil the voltage available to drive the load is equal to the open circuit voltage multiplied by the unloaded resonator quality factor Q [73]. This results in a sensitivity of

$$S_m^N = (\omega\mu AN Q_{\text{unloaded}})^2 \frac{Z_L}{(R_a + Z_L)^2}. \quad (5.10)$$

While (5.10) is maximized if both the load and the coil loss/radiation resistance are less than unity, this is not a generally achievable condition for loops with multiple turns or magnetic material loading. Despite this limitation clear improvement is observed. Even if the load impedance is significantly larger than the antenna resistance,

$$S_m = \frac{(\omega\mu AN Q_{\text{unloaded}})^2}{Z_L}, \quad (5.11)$$

and the sensitivity is improved relative to (5.9) by the square of the unloaded antenna quality factor. Relating the quality factor to bandwidth, a resonant coil operating

in half the bandwidth of a similar coil has the potential to be 6 dB or 4 times more sensitive.

5.2.3 Transmitting Loops

When designing a transmitting loop (initiator), it is generally desirable to make the antenna as efficient as possible, maximizing the flux coupled to the LFID tag or for field measurement sensor. This is performed by resonating the coil for narrow band operation and matching its ac resistance to the generator used.

5.3 Magnetic Field Measurements

The choice of employing a resonated or broadband probe in making magnetic field strength measurements comes down to a trade off between sensitivity, measurement accuracy, and required operating bandwidth.

If employing a resonated probe, greater sensitivity is achieved but care must be taken when measuring fields in the close vicinity of conducting media. Near to the surface, the mutual coupling between the sensor and its image can result in measurement error due to the change in the loop driving impedance, (5.4). Alternatively, a large resistive load will minimize this influence but significantly decrease coil sensitivity.

While these problems cannot be alleviated, the effect of resonant probe mutual coupling can be detected. The change in loop driving impedance that results from strong image coupling is linked to a probe resonant frequency shift. If the transmitting coil is broadband and frequency swept, while the receiver employs a resonated coil and a swept detector, then the frequency at which maximum coupling occurs will shift if the probe experiences significant image coupling. Using this approach it is possible to detect when the measurements made could be in error.

5.3.1 Shield Currents and Shielded Loops

One remaining challenge when making low level LF measurements of inductive fields is the formation of unintended common mode currents along probe cabling, as depicted in figure 5.2(a). If a sensor approaches an object with ground reference, then the capacitance between the probe and the object, C_{cg} (center to ground capacitance) and C_{sg} (shield to ground capacitance), can result in a current imbalance at the sensing coil. The equivalent circuit model for this situation is outlined in figure 5.2(b). If

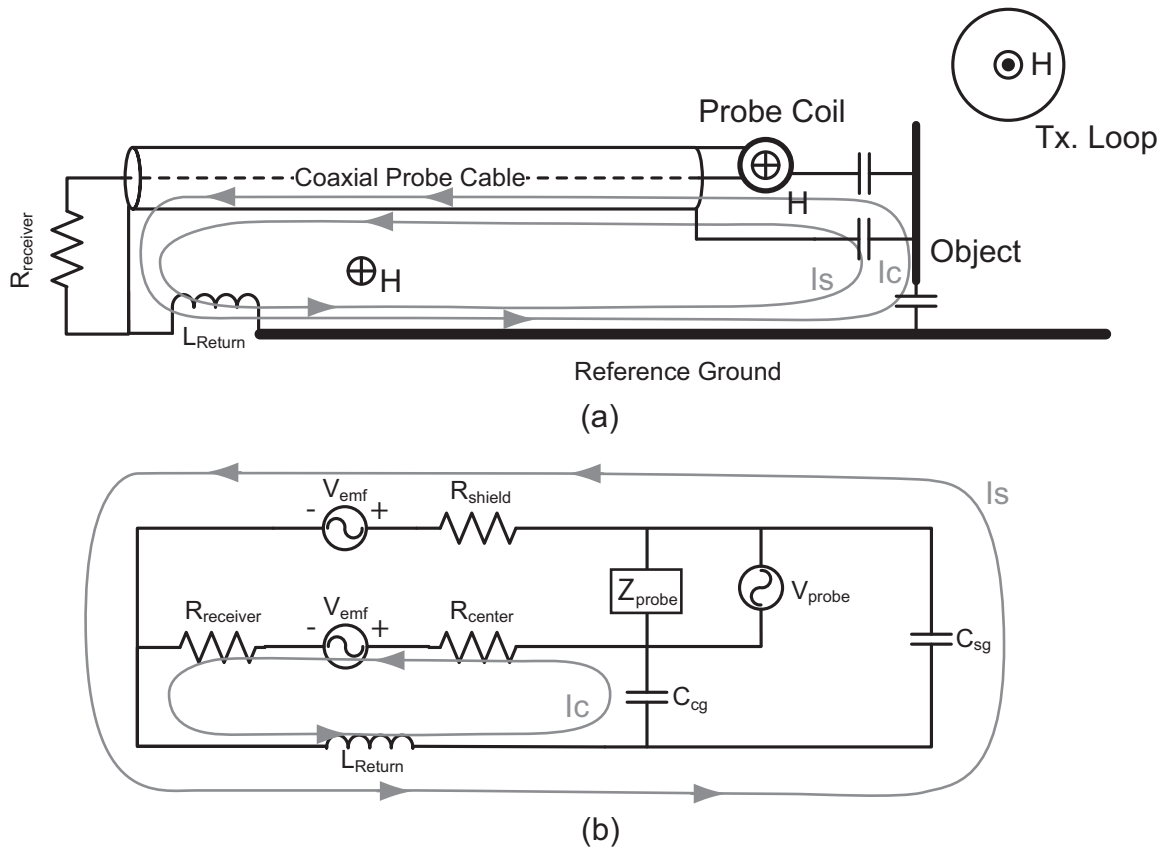


Figure 5.2: Low frequency shield currents. (a) Measurement scenario. (b) Equivalent circuit model.

the capacitances C_{cg} and C_{sg} are significantly imbalanced or C_{cg} becomes quite large, then the impressed common mode current I_c will contribute in driving the receiver impedance.

To maintain a balance between C_{cg} and C_{sg} at low frequencies, shielded loops

are employed as shown in figure 5.3(a). It should also be noted that the typical

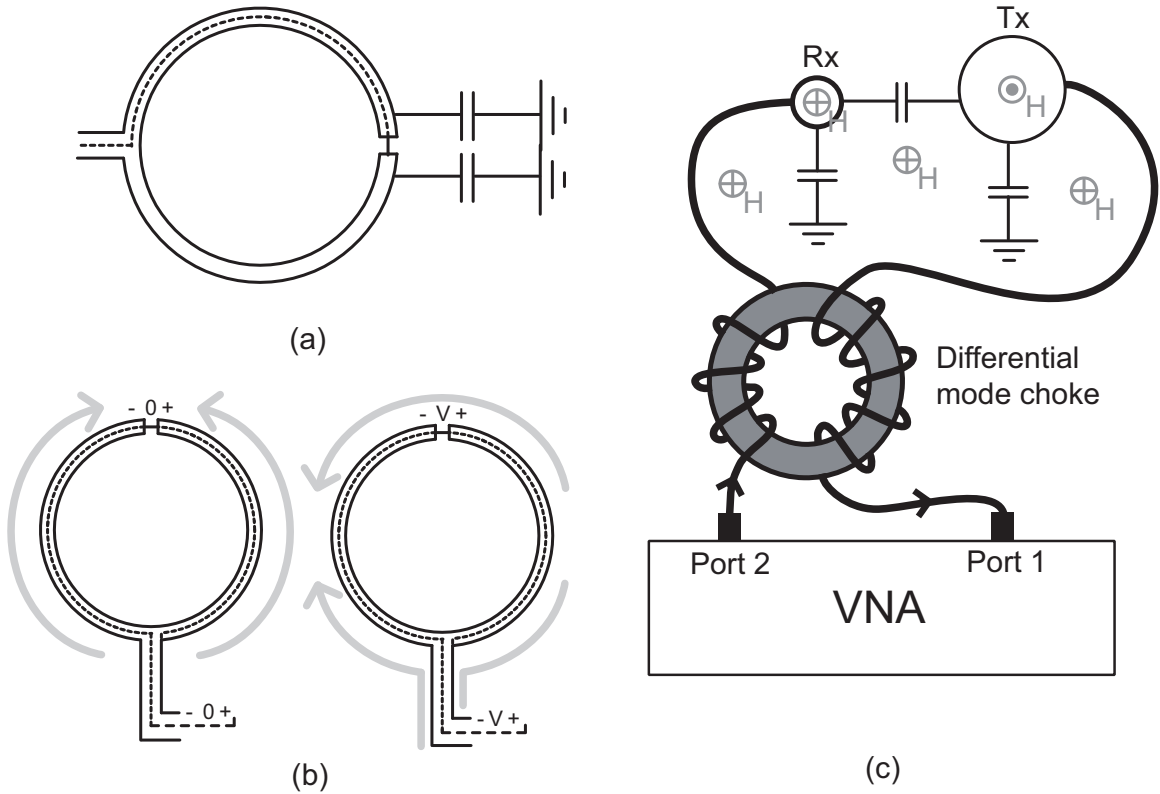


Figure 5.3: Shielded loop and measurement setup. (a) Capacitance balancing by a shielded loop. (b) Shielded loop sensitivity to non-solenoidal electric field. (c) Test setup used to eliminate common mode currents.

method of constructing a shielded loop antenna leaves the probe sensitive to strong non-solenoidal electric fields that are asymmetric with respect to the shield gap and feed (see figure 5.3(b)). These can occur when attempting measure the magnetic field of electric dipole sources, but for the LF magnetic fields in question the electric field contribution is very small and entirely solenoidal.

Shielded loops are generally broadband, non-resonant probes. When greater sensitivity is required then a resonated coil may alternatively be used if a choke is employed along the probe line, increasing the return path inductance and eliminating the common mode current along the probe cables. In the case where a vector network analyzer (VNA) is employed for characterization of field decay, then a differential mode choke

between the transmit and receive channels helps to eliminate common mode shield currents, as shown in figure 5.3(c).

5.4 Review

The goal of this chapter was to discuss the highly variable fields, antenna sensitivity limitations, and measurement concerns that arise for systems in the induction region of a current loop source. Considerations for optimizing receiving loop sensitivity were made and modified test and measurement procedures were introduced to help alleviate concerns about probe image coupling and shield current imbalance.

CHAPTER 6

Software Validation and System Optimization

In this chapter the efficiency of the numerical implementation is first analyzed. The benefits of the MLGD technique are demonstrated and an optimal MB expansion set is selected. Solution accuracy is verified by comparison of field strength data computed from simulation and that measured using the techniques of Chapter 5. In these comparisons the sheet impedance forms of Chapter 2 are also evaluated. Finally, applicability of the numerical method is demonstrated as simulations and measurements, performed on actual LFID systems, are used to predict tag placement.

6.1 Efficiency

The efficiency of this numerical implementation stems from introduction of the MLGD and the improved convergence of employing the Multibasis iterative procedure. The reduced flop count and memory overhead of the MLGD is first examined and convergence for different bases are compared.

6.1.1 Setup Time and Memory Overhead

The primary goal of implementing the MLGD is to reduce the overhead in preparing a system of equations for solution. As a demonstration of the benefits of imple-

menting this method, figure 6.1 shows the memory requirements when the MLGD is applied to a PEC square plate and a set of circularly symmetric PEC cans. For

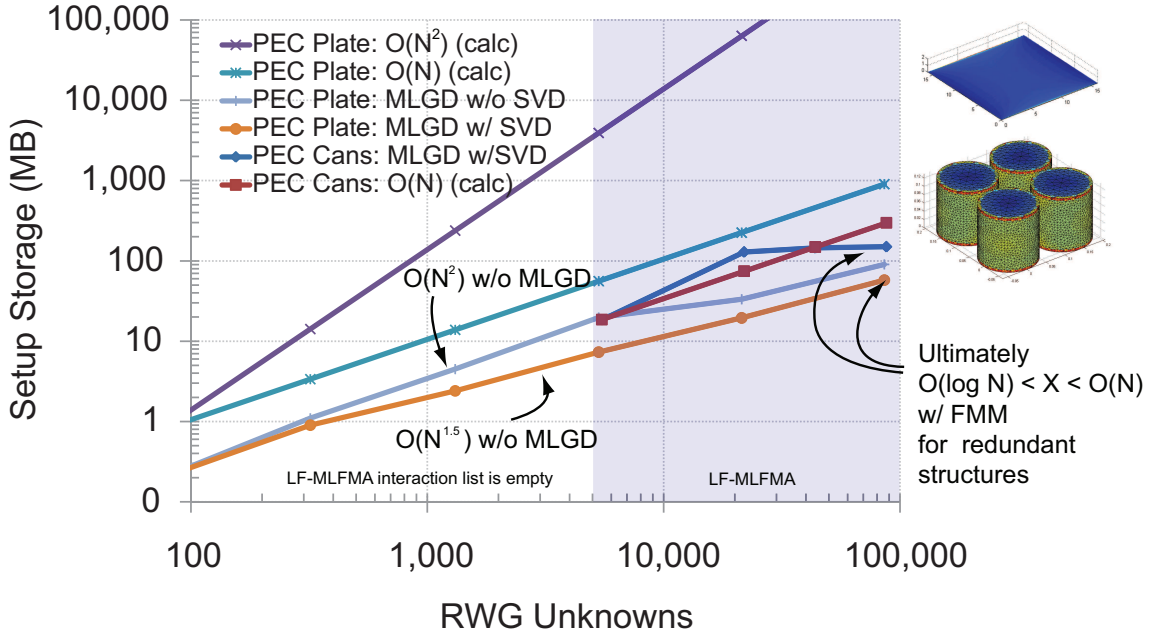


Figure 6.1: Memory overhead vs. the number of RWG unknowns. MLGD employing 4 subfacets/superfacet at 125 kHz. LF-MLFMA with $L = 5 > 5,000$ RWG Unknowns.

structures with significant numbers of redundant interactions, the memory overhead required to store near-term and scale invariant multipole expansions is significantly reduced. When the MLGD is used in the absence of matrix compressions techniques, improvement depends on the regularity of the structure in question. For example, constant storage is achieved in figure 6.1 for a set of PEC cans because of the toeplitz nature in which they are constructed. For an arbitrarily assembled PEC plate there exists a greater number of unique near-term interactions and slow storage growth continues. When used in conjunction with multilevel matrix compression techniques the overall storage requirements decrease from from $O(N)$ to low $O(\log N)$.

Directly correlated to the storage cost is the time (and corresponding flop count) required to pre-compute these interactions, as shown in figure 6.2. By implementing the MLGD in conjunction with fast iterative methods such as an MLFMM, the setup

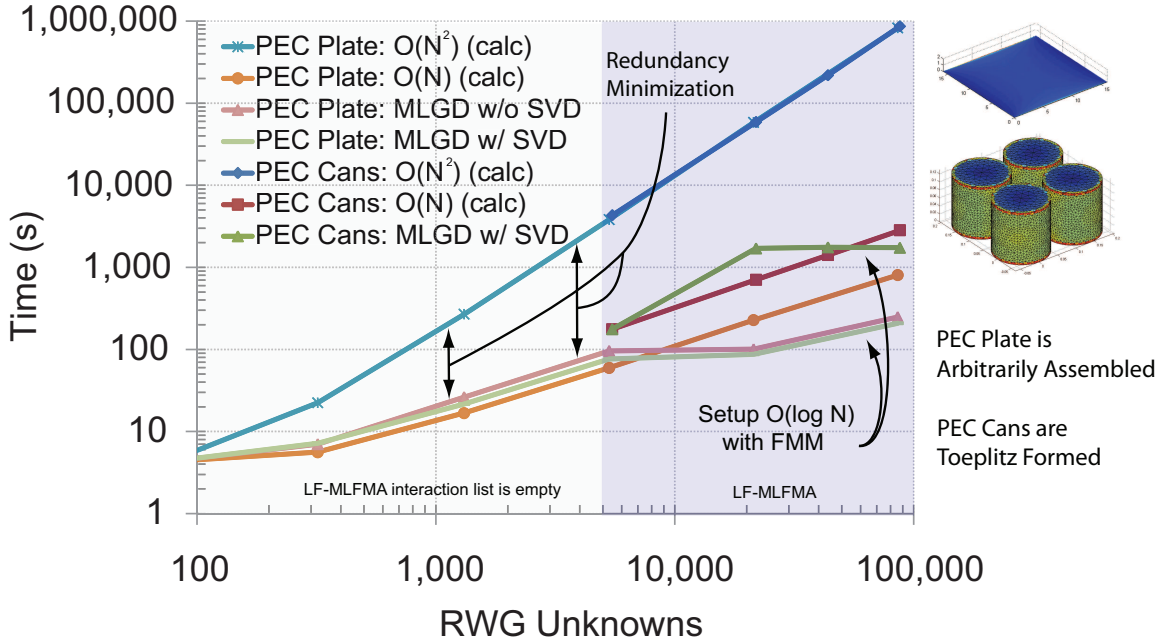


Figure 6.2: Pre-compute time for a square PEC plate and PEC cylinder array. MLGD employing 4 subfacets/superfacet at 125 kHz. LF-MLFMA with $L = 5 > 5,000$ RWG Unknowns.

time and storage requirements of solving engineered structures can be significantly decreased.

6.1.2 Basis Selection and Solution

While the MLGD method of describing the structure is beneficial in reducing memory overhead and setup time, it does not have a significant effect on the cost of solving the system of equations. In this work solution time is improved by application of the Multibasis method in conjunction with matrix compression techniques. This section examines the rate of convergence for different multibasis expansion sets. The best multibasis set is then applied to the solution of systems with increasing numbers of unknowns.

Convergence

Since the MB method employs simultaneous application of multiple higher level expansions it is necessary to examine the convergence of the method for different higher level groupings. Typically, information detailing the matrix condition number and eigenspectra would be provided when discussing iterative method convergence. However, the MB method matrix is an an over determined set of equations (when directly formed), and it is not a straightforward task to compare its condition number or eigenspectra to predict convergence. Instead, this work employs a Monte Carlo approach by examining iteration count for a range of higher level expansions on a PEC spherical shell and a PEC disk over a range of frequencies.

The results obtained when simulating a PEC sphere illuminated by a plane-wave and solved using the Conjugate Gradient Squared (CGS) algorithm [49] in conjunction with the MB method are depicted in figure 6.3.

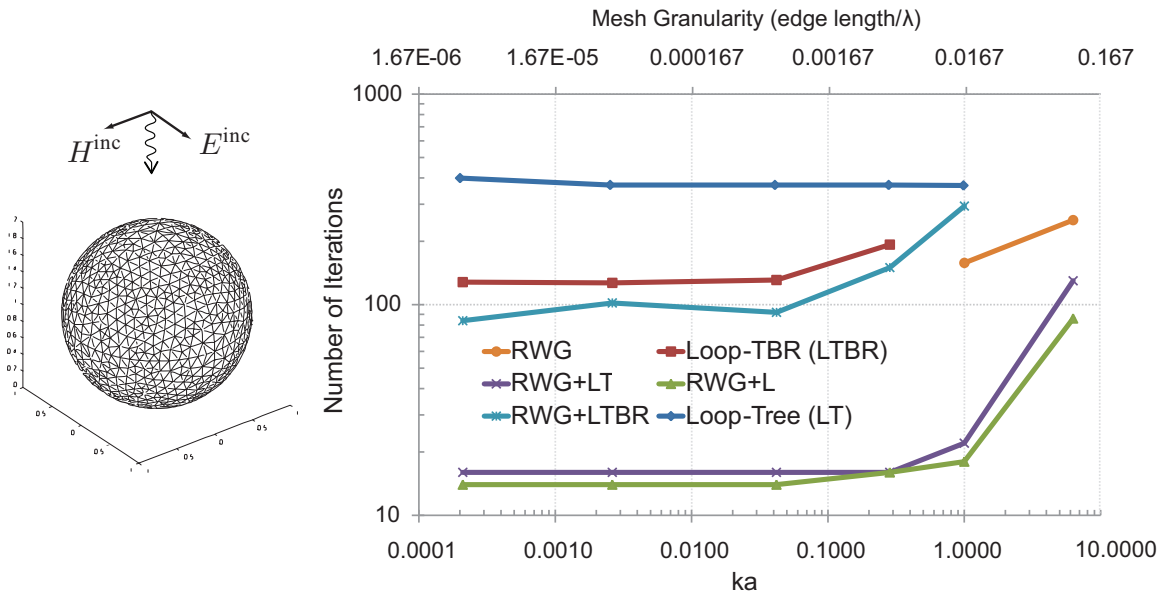


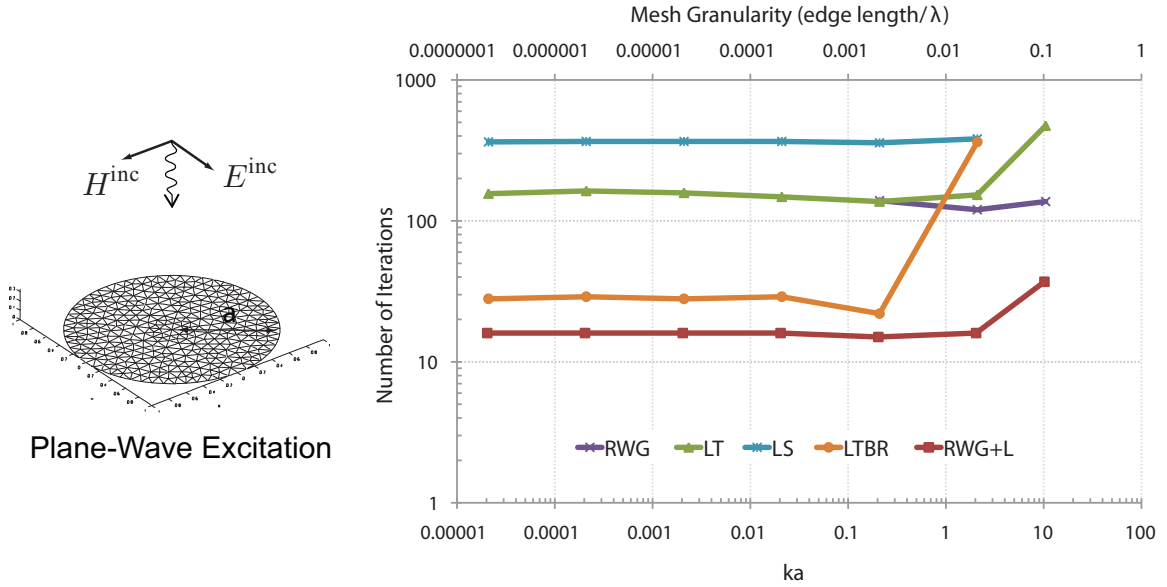
Figure 6.3: MB method convergence for PEC sphere. Simulation of $a = 1$ m radius sphere with 3240 RWG unknowns. Convergence at $\epsilon_{\text{tol}} = 1 \times 10^{-6}$ via CGS.

The solitary RWG expansion set is shown to converge with accurate results in

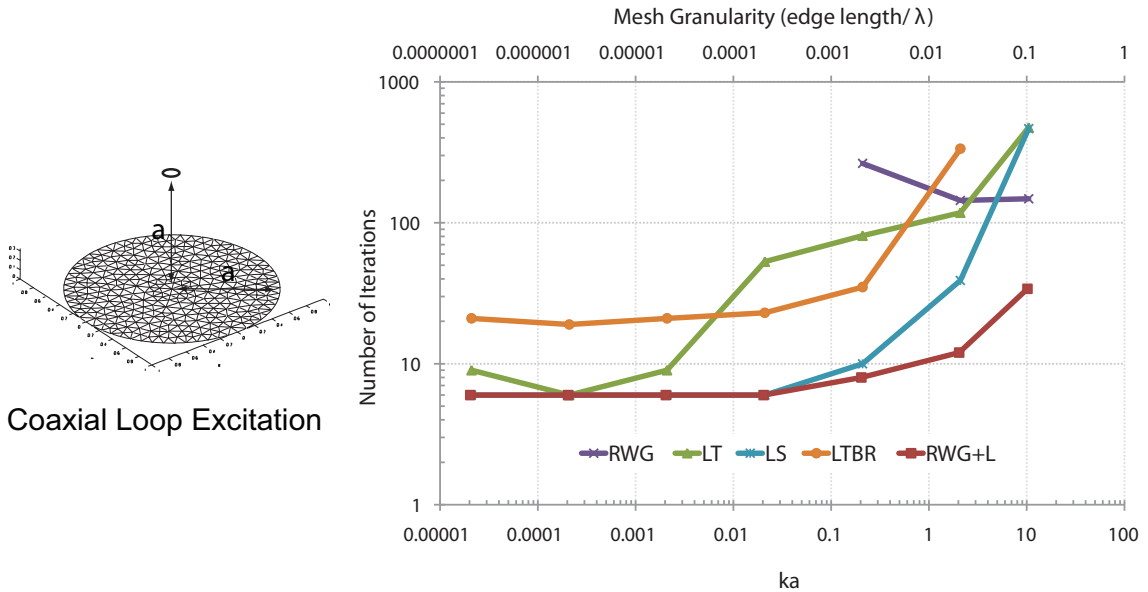
100 to 300 iterates for mesh granularity in the range of $\lambda/50$ to $\lambda/10$. For fine discretization the system is ill-conditioned (failing to account for solenoidal currents) and the iterative solver fails to converge in fewer than 500 iterates (the selected upper bound in this experiment). The Loop-Tree (LT) expansion by contrast consistently converges in 300 to 400 iterates for fine mesh but falters for granularity greater than $\lambda/50$. When Loop-Tree Basis Rearrangement (LTBR) is applied, the number of iterates on a fine mesh is significantly reduced relative to *LT*, but it continues to exhibit ill-conditioning above $\lambda/50$.

Alternatively, for the RWG+LT multibasis expansion (where both the RWG and Loop-Tree expansions are included in the MB transforms) convergence is clearly superior, reaching the solution in as few as 16 iterates for fine mesh and outperforming RWG at coarse granularity. Now, since the Tree expansion is simply a subset of the RWG expansion, an examination of the RWG+L MB expansion seems appropriate. Since the solution space is the same as that of the RWG+LT expansion (but requires fewer error terms be minimized), the RWG+L expansion demonstrates slightly improved converge relative to RWG+LT across the spectrum. The final MB expansion reported is the RWG+LTBR set. While there is a distinct improvement relative to the LTBR alone, the solution spaces of these two expansions do not compare with the improved performance of the RWG+L set.

Clearly, the MB method can significantly improve convergence on the smooth surface sphere above. To ensure that the performance is not particular to the surface previously employed and that it properly converges for structures with significant edge current, further examination is performed. Figure 6.4(a) shows the number of iterations required a when employing the RWG+L expansion in relation to the other common expansions, this time including the Loop-Star bases, on a PEC disk under plane wave illumination. As with the sphere, significant improvement is evident for plane wave incidence on the open surface object. However, for the low frequency



(a)



(b)

Figure 6.4: MB method convergence for PEC disk. Simulation of $a = 1$ meter radius disk with 924 RWG Unknowns. Convergence at $\epsilon_{tol} = 1 \times 10^{-6}$ via CGS. (a) Plane Wave excitation. (b) Loop source excitation.

RFID simulations motivating this work the excitation will not be a plane wave, but will arise primarily from loop sources. This situation is considered in Figure 6.4(b) where the number of iterations is compared for a disk illuminated by a small coaxial

loop source at one radius elevation. In the case of purely solenoidal excitation the fine mesh (low frequency) performance of all expansions that include the curl conforming loop bases are improved. Since the excitation is purely solenoidal the resulting current distribution is also solenoidal and the loop expansion dominates the solution. The loop basis expansion is well conditioned and thus all of the methods perform well. However, at higher frequencies (coarse granularity) the excitation at the disk surface is no longer purely solenoidal and the RWG+L expansion is clearly the best choice.

Solving the Linear System

Now that the MB method with RWG+L expansion has been clearly shown as the best performing approach across a wide range of mesh granularity and for open and closed surfaces, the cost RWG+L application in conjunction with the MLGD and matrix compression is examined. Figure 6.5 shows the time required by the

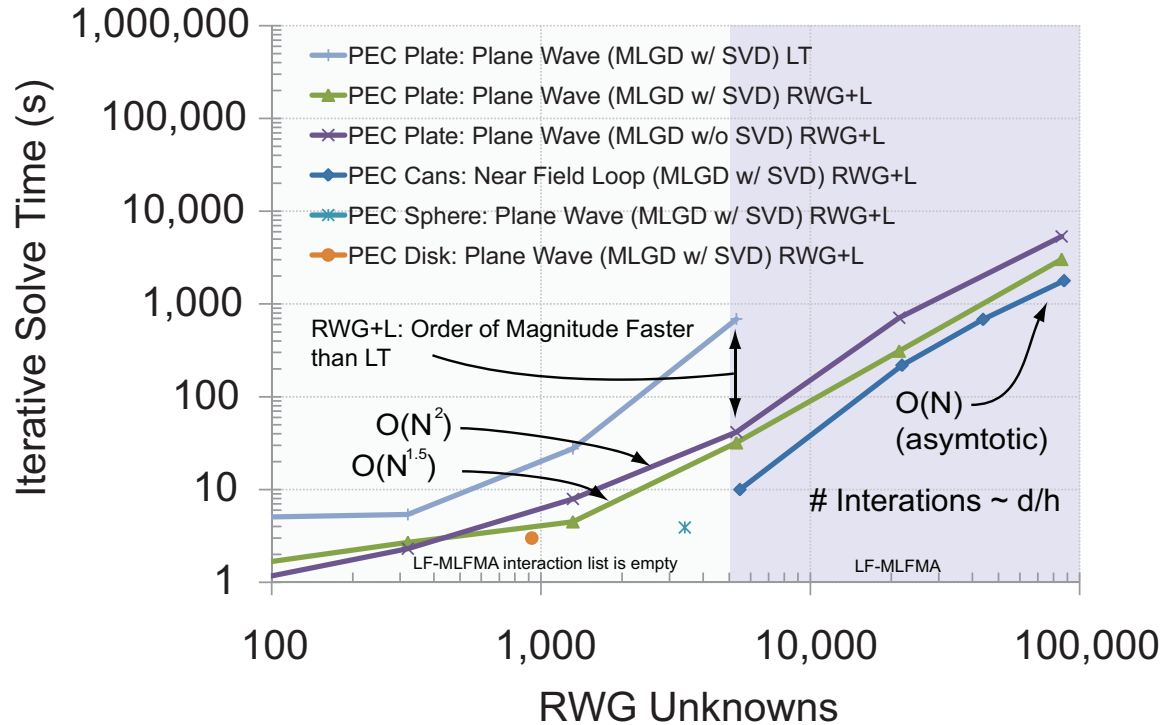


Figure 6.5: Solution time in relation to the number of RWG unknowns. $f = 125$ kHz. PEC plate – plane wave excitation. PEC cans – loop excitation. Matlab implementation, 2 GHz Intel Core 2 Duo (single core).

current MATLAB [74] implementation to correctly solve a set of structures at 125 kHz with increasing numbers of unknowns. For unknown count the driving factor for solver compute time is the number of LF-MLFMA levels and cluster sizes. Since the current simulator does not employ an adaptive multilevel FMM algorithm, the numbers of unknowns employed at the protofacet level dictate the cluster size and must be chosen judiciously to achieve an acceptable solution time. Furthermore, the accuracy of the LF-MLFMA expansion requires that next-nearest neighbors be included in the near term interaction list, and this in turn pushes the corner for $O(N)$ performance to much larger simulations.

6.2 Accuracy

In order to ensure that the software implementation described in the preceding chapters is accurate, both theoretical and experimental verification need to be employed.

6.2.1 PEC Sphere

The exact solution for a closed spherical shell of perfect electric conductivity is described by its Mei series solution [38]. To compare with the theoretical current distribution, a PEC spherical shell of $a = 1$ meter radius under plane wave illumination is simulated at $ka = 0.0026$ and $ka = 1.000$. Theoretical and simulated surface current distributions are shown in figure 6.6, and clearly show the accuracy of the implementation.

While typically this type of validation is performed by computing the bistatic radar cross section (RCS) of such an object, rather than its current distribution, such solutions are not sufficiently unique for electrically small structures. When a highly conductive and electrically small object is illuminated by a plane wave, circulating

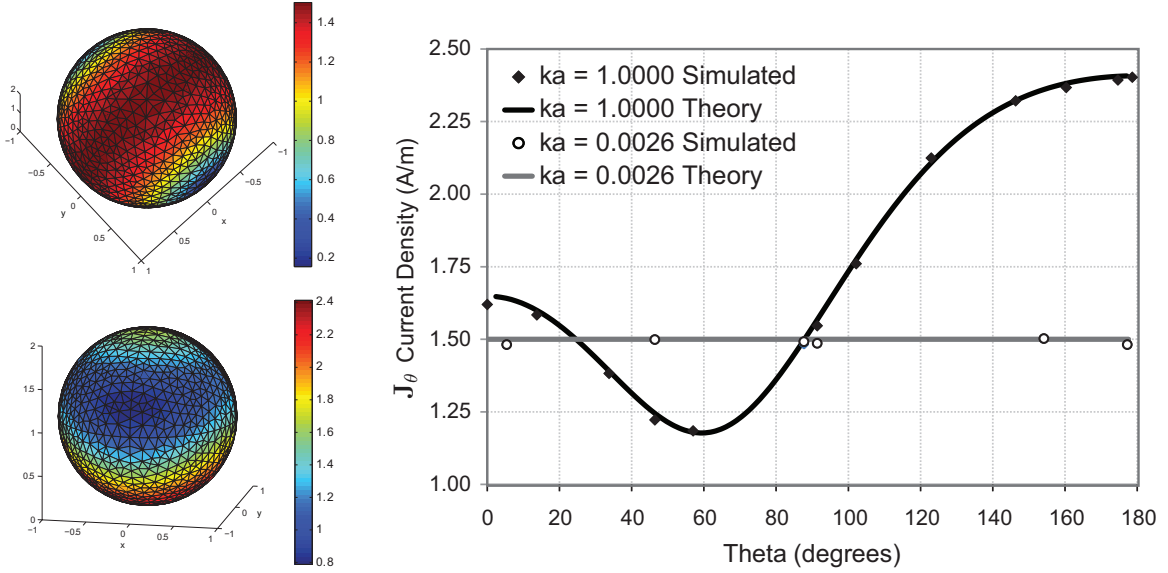


Figure 6.6: Current distribution on a PEC sphere. A 1 m radius PEC sphere immersed in a \hat{z} directed plane wave, $E_x = 120\pi(V/m)$. (a) $ka = 0.0026$, (b) $ka = 1.000$, (c) Theoretical and simulated surface current density \mathbf{J}_θ .

eddy currents in opposition to illuminating magnetic field dominate. However, these circulating currents do not contribute to the far-field scattering cross section [44] and their accuracy could not be verified by comparing RCS data.

6.2.2 Scattering by Finite Material Disk

With simulator performance verified for a PEC structure, it is now desirable to examine its performance for non-PEC objects. This is performed through simulation and measurement of a set of metallic disks excited by a current loop. Measurements, made taking into account the probe, source, and setup considerations of Chapter 5, are compared to simulated data.

In the case of conductive materials with impressed solenoidal electric fields, Eddy currents form at every point on the metallic surface in opposition to the induced magnetic flux (Lenz's Law [48]). For high conductivity metals, adjacent current loops current cancel until they reach a bounding edge. These currents traverse along the edges of surface and follow circulating paths. However, as the sheet impedance

value of a material increases (e.g. the metal is thinned or is of lower conductivity), adjacent currents no longer cancel efficiently and edge currents move away from the disk edge and decrease in magnitude, as shown in figure 6.7. Here it is evident that

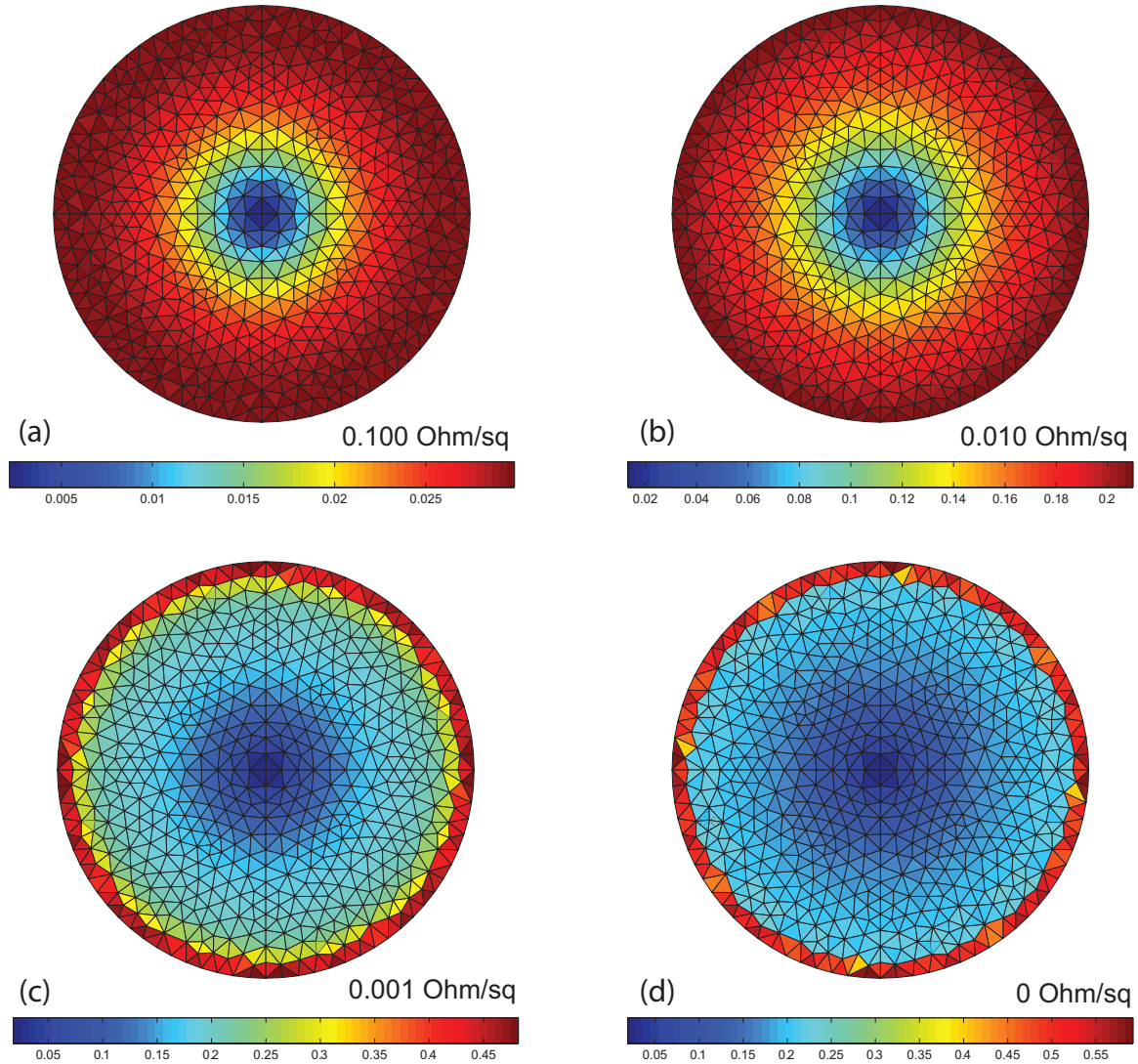


Figure 6.7: Material disk LF current distribution. Radius = 6.5 cm, $N = 1580$, $f = 125$ kHz. (a) 0.1 Ω /sq resistive disk (27 ITERS), (b) 0.01 Ω /sq resistive disk (26 ITERS), (c) 0.001 Ω /sq resistive disk (14 ITERS), (d) PEC disk (9 ITERS).

the influence of low contrast materials on electric and magnetic fields in the LF band is minimal. Alternatively, high contrast metallic materials have a significant effect and must be considered.

Before delving into the simulation and measurement results, I first examine the

sheet impedance values computed for a representative set of non-magnetic conducting materials, including lead, aluminum, and copper, as shown in Table 6.1.

Table 6.1: Non-magnetic thin metal sheet impedance values. Lead, Aluminum, and Copper. Z_{sh} reported in Ω/\square at 125 kHz. Incident wave impedance $\eta_{inc} = 1\Omega$ is assumed.

Material $\eta_m(\Omega)$	Lead 3.1E-4(1+j)	Aluminum 1.1E-4 (1+j)	Copper 9.3E-5 (1+j)
Thickness	0.0078 mil	0.001 mil	0.00066 mil
Z_{sh}^0	1.0	1.0	1.0
Z_{sh}^1	1.0 + j 1.6E-7	1.0 + j 2.1E-8	1.0 + j 1.4E-8
Z_{sh}^B	1.0 + j 4.6E-7	1.0 + j 6.1E-8	1.0 + j 4.0E-8
Z_{sh}^F	1.0 - j 4.3E-7	1.0 - j 5.7E-8	1.0 - j 3.8E-8
Z_{sh}^{NP}	1.0 + j 1.6E-8	1.0 + j 2.1E-9	1.0 + j 1.4E-9
Thickness	0.4 mil	0.65 mil	0.01 mil
Z_{sh}^0	2.0E-2	1.6E-3	6.8E-2
Z_{sh}^1	2.0E-2 + j 3.4E-6	1.6E-3 + j 5.4E-6	6.8E-2 + j 9.2E-8
Z_{sh}^B	2.0E-2 + j 3.5E-6	1.6E-3 + j 5.5E-6	6.8E-2 + j 1.0E-7
Z_{sh}^F	2.0E-2 - j 1.9E-6	1.6E-3 - j 2.7E-6	6.8E-2 - j 6.0E-8
Z_{sh}^{NP}	2.0E-2 + j 8.4E-7	1.6E-3 + j 1.4E-6	6.8E-2 + j 2.1E-8
Thickness	100 mil	2 mil	20 mil
Z_{sh}^0	7.9E-5	5.2E-4	3.4E-5
Z_{sh}^1	3.1E-4 + j 3.1E-4	5.2E-4 + j 1.7E-5	9.2E-5 + j 9.4E-5
Z_{sh}^B	3.1E-4 + j 3.1E-4	5.2E-4 + j 1.7E-5	9.2E-5 + j 9.4E-5
Z_{sh}^F	-1.6E-5 + j 1.0E-6	5.2E-4 - j 8.4E-6	-6.0E-6 - j 1.6E-5
Z_{sh}^{NP}	1.5E-4 + j 1.6E-4	5.2E-4 + j 4.2E-6	4.3E-5 + j 3.9E-5

As mentioned in Chapter 2, the forward and backward scattering sheet impedance values, Z_{sh}^B and Z_{sh}^F are particularly useful as a figure of merit when using sheet impedance equivalent boundary conditions. If the backward and forward sheet impedances are equal (or nearly equal) then the material can be accurately modeled via an electric sheet impedance boundary. When the medium is thin in terms of exterior wavelength then the average first and second order forms, Z_{sh}^0 and Z_{sh}^1 , are useful for low and high contrast media, respectively. The equivalent forms Z_{sh}^B and Z_{sh}^{NP} can similarly be applied in the case of propagating and non-propagating field regions.

For the metals in table 6.1, the first set of rows depicts the thickness at which

the sheet impedance equivalent forms are all approximately $1 \Omega/\square$. At this level of resistivity the materials are essentially transparent to 125 kHz LF fields. The other end of the spectrum is depicted by the bottom set of sheet impedance values. Here, the material thickness is such that the forward and backward scattering impedances are not equivalent, but the overall equivalent resistivity is so low that the material can be considered a PEC surface.

To verify that these sheet representations can accurately predict physical phenomena for LFID systems at 125 kHz, the total normal magnetic field in the shadow region of a set of 6.5 cm radius metallic disks is simulated and measured. Each disk is illuminated by a near-field current loop and the shadow region field is measured along the disk axis, as depicted in figure 6.8(a). For the non-magnetic materials shown in

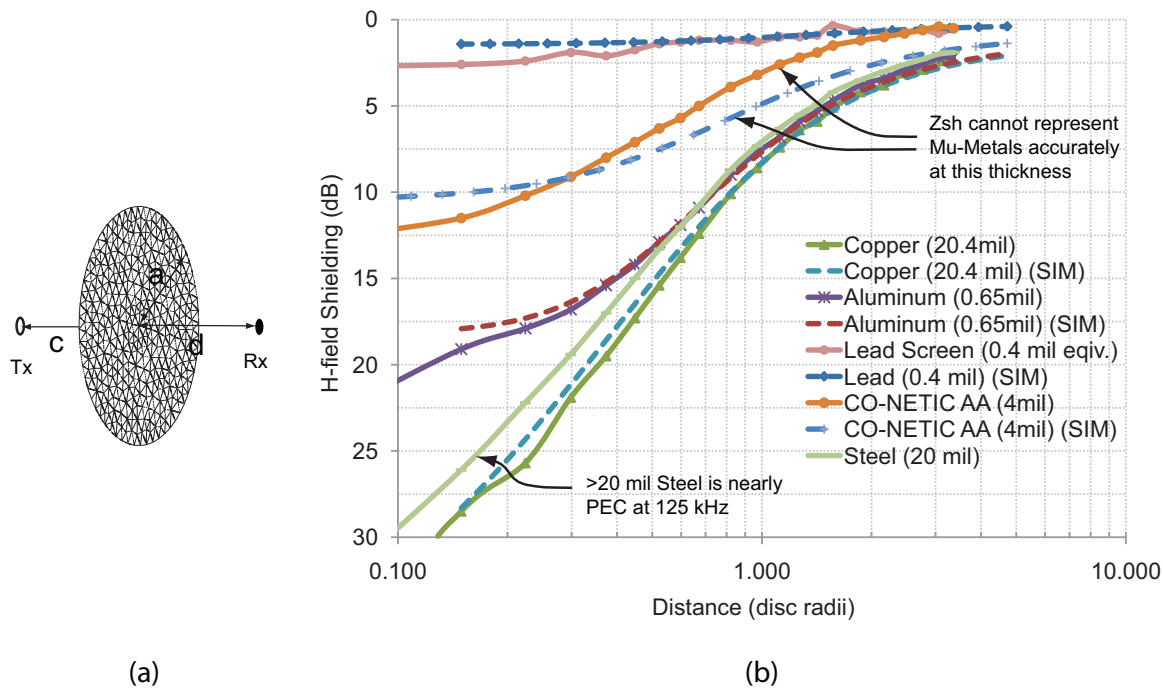


Figure 6.8: Material disk H-field shielding: coaxial. (a) Measurement setup, $a = 6.5$ cm, $c = 8.5$ cm. (b) Measured and simulated results.

figure 6.8(b), the different sheet boundary forms are all equivalent. Results for the 20 mil copper disk are essentially that of a PEC plate, showing how the magnetic moment of the eddy currents acts to cancel the incident field near the disk center.

However, with thin aluminum and lead samples disc current decreases and the magnetic moment of the disk no longer cancels the incident field on the shadow side. Clearly, comparison of the simulated and measured data shows that the sheet impedance forms for the non-magnetic materials tested properly depict the transparency of the disk. However, included in the same figure are the results for simulation and measurement of some high permeability metal disks that must be discussed.

Included in figure 6.8(b) are the measurement and simulation results for both a 20 mil mild steel plate and a 4 mil CO-NETIC metal. Co-NETIC is a Nickel-Iron-Molybdenum composite high μ metal, with relative permeability of 30,000 and a conductivity of 1.86×10^6 S/m [75]. The relevant sheet impedance forms for these two materials in addition to an intermediate μ -metal (Netic) are included in table 6.2. For these high permeability metals, the different sheet impedance forms exhibit greater variation depending on the material thickness. In the case where these metals are very thin (the first set of rows in table 6.2) the forward, backward, and non-propagating sheet impedances are equivalent while the zeroth and first order average approximations continue to predict PEC behavior. Since the forward, backward, and non-propagating forms are based on the equivalent current formulation rather than the average approach, they are expected to be more accurate.

For the case of thicker magnetic metals (in the second set of rows in table 6.2) it becomes clear that the forward and backward sheet impedances are not equivalent. In these cases the material cannot be accurately represented solely via the electric sheet impedance formulations presented. As expected the simulator is unable to properly capture the rate of field decay on the backside of the disk in figure 6.8 for the 4 mil thick CO-NETIC material. One exception to this rule occurs for the case of a vanishing forward sheet impedance. When no forward scattered field exists, then the material is entirely non-transparent, and (when electrically small) it can be accurately modeled by a PEC surface.

Table 6.2: Magnetic thin metal sheet impedance values. CO-NETIC, NETIC, and Steel. Z_{sh} reported in Ω/\square at 125 kHz. Incident wave impedance $\eta_{inc} = 1\Omega$ is assumed.

Material $\eta_m(\Omega)$	CO-NETIC AA 8.9E-2(1+j)	NETIC 3.3E-3 (1+j)	Steel 2.2E-2 (1+j)
Thickness	0.021 mil	0.043 mil	0.019 mil
Z_{sh}^0	3.4E-5-1.3E-16	5.0E-3-3.9E-15	5.2E-4-1.8E-15
Z_{sh}^1	3.4E-5 + j 4.4E-7	5.0E-3 + j 9.1E-8	5.2E-4 + j 4.1E-7
Z_{sh}^B	1.0 + j 3.7E-2	1.0 + j 5.1E-5	1.0 + j 2.3E-3
Z_{sh}^F	1.0 - j 3.5E-2	1.0 - j 4.7E-5	1.0 - j 2.2E-3
Z_{sh}^{NP}	1.0 + j 1.3E-3	1.0 + j 1.8E-6	1.0 + j 7.9E-5
Thickness	4 mil	4 mil	4 mil
Z_{sh}^0	1.8E-7-j 6.6e-19	5.4E-6-j 4.2E-18	2.5E-6-8.5E-18
Z_{sh}^1	2.9E-6 + j 2.9E-6	1.6E-5 + j 1.7E-5	1.1E-5 + j 1.1E-5
Z_{sh}^B	8.6E-2 + j 1.1E-1	3.3E-3 + j 3.5E-3	2.2E-2 + j 2.3E-2
Z_{sh}^F	-8.7E-9 + j 5.1E-9	-2.8E-4 - j 3.5E-4	-5.3E-4 + j 3.9E-4
Z_{sh}^{NP}	4.5E-2 + j 4.5E-2	1.5E-3 + j 1.5E-3	1.1E-2 + j 1.1E-2
Thickness	20 mil	20 mil	20 mil
Z_{sh}^0	3.5E-8-j 1.3e-19	1.1E-6-j 8.4E-19	4.9E-7-1.7E-18
Z_{sh}^1	2.9E-6 + j 2.9E-6	1.7E-5 + j 1.7E-5	1.1E-5 + j 1.1E-5
Z_{sh}^B	8.8E-2 + j 1.1E-1	3.3E-3 + j 3.3E-3	2.2E-2 + j 2.3E-2
Z_{sh}^F	-2.1E-38 - j 4.7E-38	-5.5E-10 - j 2.4E-9	-9.3E-12 - j 1.5E-12
Z_{sh}^{NP}	4.5E-2 + j 4.5E-2	1.7E-3 + j 1.7E-3	1.1E-2 + j 1.1E-2

This is the case for the material thickness shown in the bottom data set of table 6.2. For these samples the forward scattering impedance is vanishing, and they can be modeled as PEC surfaces without significant error. Such is the case for the 20 mil thick mild steel plate measured in figure 6.8, which has a shadow region field similar to that of a highly conductive non-magnetic plate.

To further investigate material and disk effects in the case of a coplanar excitation, the loop is placed in the plane of the material disk, as in figure 6.9. In this scenario the induced current rotates in the same direction as the source, and the resulting scattered field adds in phase to the incident field. For high conductivity materials, edge currents predominate and the singularity effect increases the total magnetic field measured near the disk edge. Again, simulation and measurement match well.

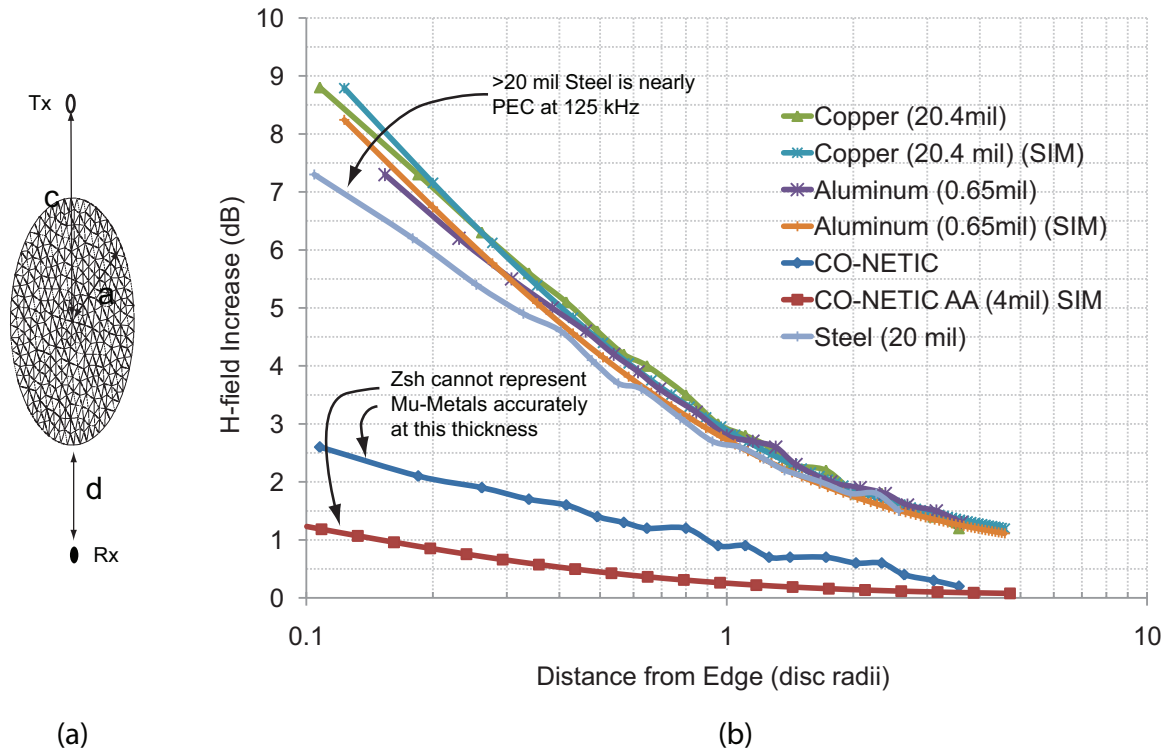


Figure 6.9: Material disk H-field shielding: coplanar. (a) Measurement setup, $a = 6.5$ cm, $c = 13.2$ cm. (b) Measured and simulated results.

6.3 Applicability

Now that the decreased overhead of the MLGD has been verified, an optimal MB expansion was selected, and the limitations of simulating relevant material media were examined, all that remains is to demonstrate the applicability of this work to low frequency RFID system optimization.

6.3.1 Tire Tag Placement

In the year 2000, the United States Congress passed the Transportation Recall Enhancement, Accountability, and Documentation (TREAD) Act [76]. Following from the requirements of this act, the Department of Transportation mandated that Tire Pressure Monitoring Systems (TPMS) be phased into all new motor vehicles with a gross vehicle weight of less than 10,000 pounds. Over the course of the

next few years, these TPM systems will be placed into the majority of consumer vehicles to alert the driver when a tire is under-inflated. Direct versions of these systems utilize active tire pressure transponders in each tire cavity. These devices are small, battery operated UHF transmitters that send tire pressure and temperature data to an onboard receiver when interrogated by an LF excitation. Each tire is interrogated separately so that the receiver can correlate pressure and temperature with a particular tire, even if the user rotates them regularly.

In order to interrogate an active TPM sensor mounted on a wheel rim, LF initiator coils are placed above or to the side of the tire (along the stone guard in the fender of the vehicle) as depicted in figure 6.10(a). Within the wheel, the TPM sensor is

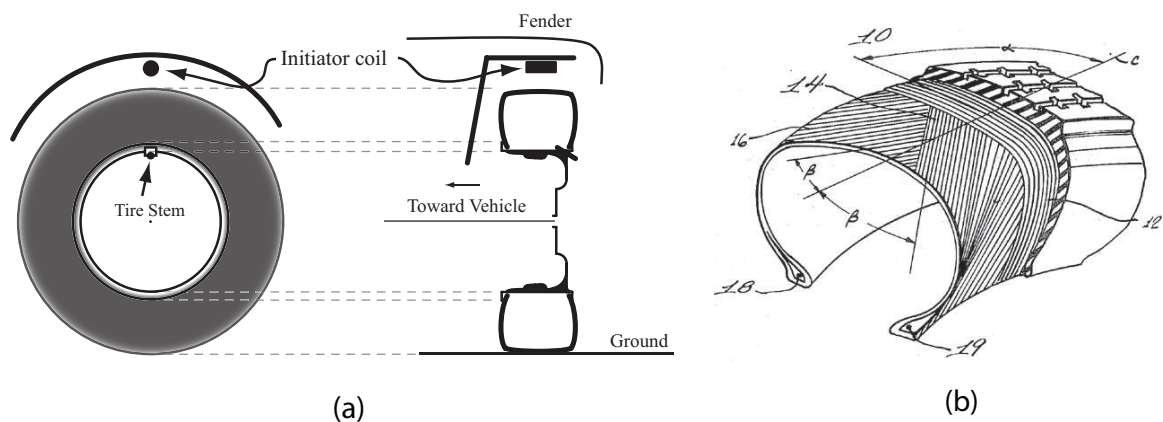


Figure 6.10: Diagram of TPM sensor and initiator pair with tire cross-section. (a) Diagram showing the LF initiator and TPM sensor placement in a vehicle wheel well. (b) A cross-section of a tire. Number 12 is the radial-ply while numbers 14 and 16 are bias-plyes (Source: From [77]).

frequently affixed to the valve stem or strapped to the rim via a metal band. Wheel rims are made of either steel or aluminum alloys, ranging in thickness from 100 to 600 mils (2.5 to 15 mm). Placed over the rim is a steel-belted radial tire that includes a webbing of steel wires and fiber strands as depicted in figure 6.10(b). However, these wires do not form closed conducting loops within the tire and measurements confirm that the tire has no measurable effect on LF coupling to the TPM sensor.

A key concern with interrogation of TPM sensors in a rotating tire is the prob-

ability of a communication failure or interrogation of an unintended recipient. For example, if the LF field at the sensor location varies dramatically for different tire rotation angles, then initiator coil current must be increased to ensure that the likelihood of a read failure is minimized. However, a higher current initiator is more likely to actuate an unintended TPM sensor in another wheel well or adjacent vehicle.

In order to investigate the coupling phenomena between an initiator and TPM sensor, a steel rim with 120 mil minimum thickness is simulated. Because of its thickness, the rim can be treated as a PEC surface. It is excited by an LF initiating coil with a magnetic moment of $\mathbf{m} = A\omega\mu_0 I = 0.007$ A-m at a distance of 47 cm from rim center, as depicted in figure 6.11(a). The resulting current distribution in

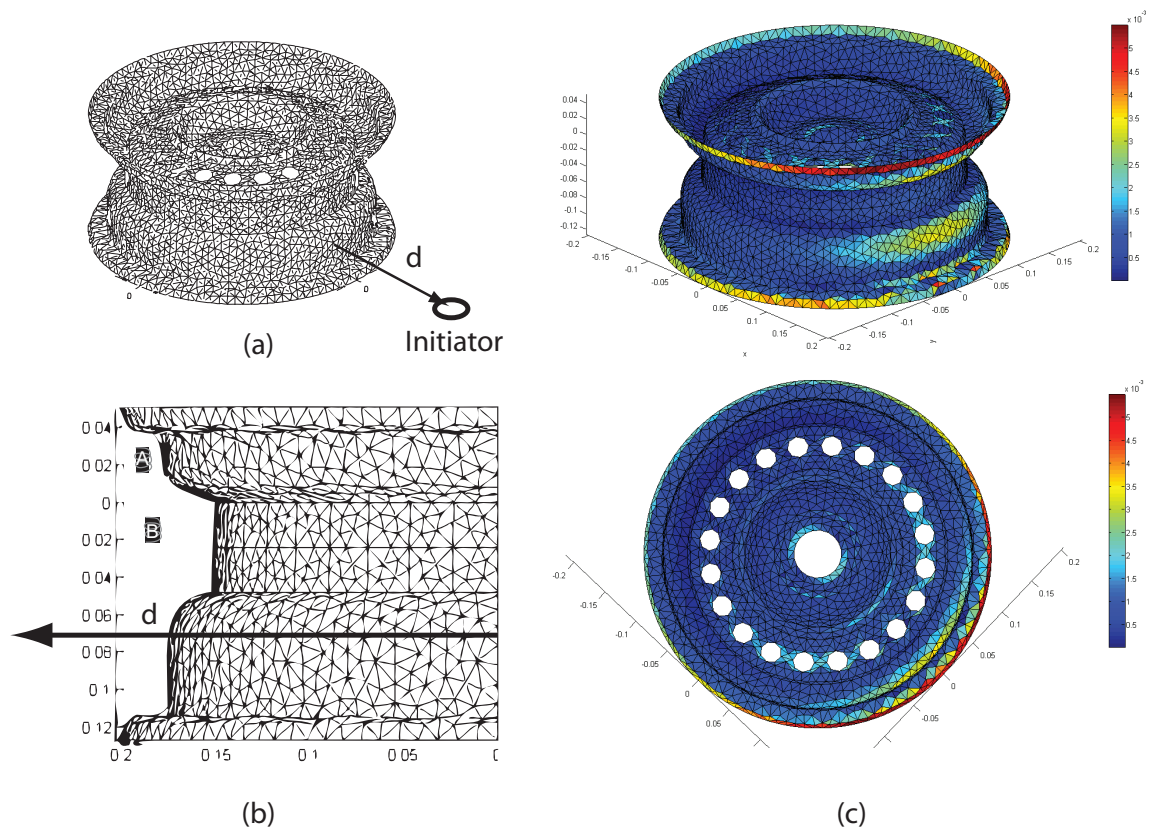


Figure 6.11: Setup and simulation of wheel rim with LF coil excitation. (a) Simulation setup, $d = 47$ cm, 9940 RWG unknowns. (b) Field strength measurement locations A and B . (c) Current distribution on the rim.

figure 6.11(c) shows that, much like a flat metallic plate, eddy currents on the the

rim move to the outer edges and circulate in an additive fashion with the excitation. To investigate sensor placement optimization, two locations are selected on the rim as shown in figure 6.11(b). Magnetic field strength is computed from the simulated current distribution, and measurements are made at the same location on a rotating rim utilizing a network analyzer setup as depicted in Chapter 5, figure 5.3. The resulting simulated and measured field strength data normalized to the highest power measured at sensor location B are plotted in figure 6.12. The resulting magnetic field

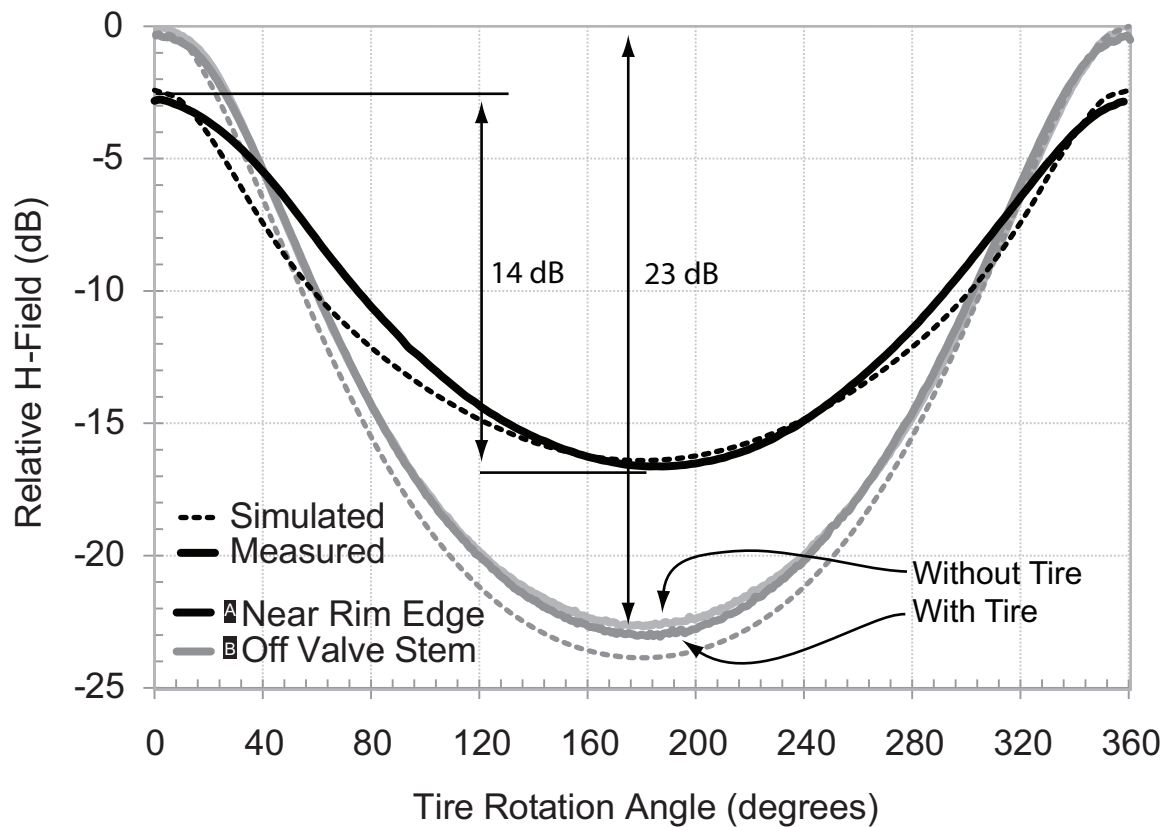


Figure 6.12: Magnetic field strength vs. tire rotation angle. Measurement and data shown for test locations *A* and *B*, as well as measurements with and without steel belted radial tire.

variation for the two sensor placement locations correlates well between simulation and measurement. For the case of a sensor with coil near the valve stem of the rim (location B), a variation of 23 dB in magnetic field strength is observed as the tire rotates. Alternatively, a coil placed closer to the rim edge (location A) demonstrating

only a 14 dB front to backside ratio as it benefits from the singularity of the eddy current in the shadow region, but is less optimally coupled to the initiator coil on the front side due to its normal proximity to the lip of the rim.

Thus, simulation indicates that shadow side improvement can be expected if the coil is placed on or near the outermost edges where the eddy currents flow.

CHAPTER 7

Conclusions and Future Work

7.1 Summary

Motivated by a desire to accurately simulate electromagnetic phenomena associated with low frequency RFID installations, this work has detailed the formulation, implementation, and validation of an advanced surface EFIE based simulator.

The first chapter of this dissertation discussed the history and practical application of RFID systems and the motivation for this work. Emphasis was placed on the challenges of simulating electrically small environments and on the limitations of currently available commercial software packages. Chapter 2 outlined the formulation of the numerical method in progression from Maxwell's equations to the discretized surface based EFIE employed. Along the way, a range of new sheet impedance approximations, including forward, backward, and non-propagating versions, were introduced. Additional considerations were made for the use of matrix compression techniques and the efficient implementation of curl and divergence conforming expansion functions. In Chapter 3 a new approach to minimizing redundant computations was described in the form of a Multilevel Geometry Description (MLGD). The MLGD compression algorithm was shown to enable efficient tracking of unique surface interactions and thus minimize the setup cost when solving a properly discretized system. Be-

cause of this multilevel approach, advanced hierarchical methods for forming bridge bases to ensure current continuity were introduced. Chapter 4 began by modifying the underlying set of sub-bases used into a more efficient current-charge (CQ) sub-basis group. Next, the expense of employing existing preconditioning methods to the MLGD structure was outlined and motivated the development of an entirely new iterative procedure. The resulting Multibasis (MB) method solves the overdetermined system of equations resulting from simultaneous application of multiple higher level expansions with accelerated convergence. The MB method was shown to be an $O(N)$ procedure, maintaining the asymptotic performance of the overall implementation. Chapter 5 departed from numerical methods to discuss the practicality of loop antenna design and the realities of the electromagnetic environment at low frequencies. Included were discussions of issues that arise when making LF field strength measurements and a pair of modified test methods were presented to help overcome these issues. Chapter 6 validated the numerical implementation through comparison with both theoretical and measured data. The overall efficiency of the simulator was examined and the optimal RWG+L MB expansion set was identified. The simulation tool was accurately applied in computing the field in the shadow region of different material disks. Finally, the applicability of the numerical implementation to the simulation and optimization of an LFID installation was demonstrated through accurate computation of the magnetic field on a vehicle rim in the presence of a low frequency TPMS initiator coil.

7.2 Future Work

While the numerical method detailed in this dissertation has many advantages over existing implementations, it is still a work in progress.

One limitation of the current work is the need for hands on assembly of the MLGD

structure by the design engineer. To facilitate a hands-off approach for pre-drawn structures, efforts employing tiling algorithms, particle packing methods, and most promisingly Oct-tree surface re-meshing need to be explored. Further improvements to the MLGD approach would include the use of local planes of symmetry and toeplitz indexing of protofacet meshes. Curvilinear meshing and mesh independent expansion functions, as well as adaptive mesh refinement through application of facet scaling are also of interest.

A second limitation resides in the use of the non-adaptive, non-diagonalized, LF-MLFMA algorithm. Inclusion of more recent broadband diagonalized approach and adaptive refinement at the protofacet level would extend the MLGD advantages to electrically large problems while at the same time reducing overall solution time.

Additional improvements to the current implementation could include the extension of the MLGD to the computation of scattered field values about the structure, the inclusion of the magnetic field integral equation kernel and magnetic surface currents (for simulations where tangential E-field boundary conditions are not applicable), and application of the Multibasis method in conjunction with preconditioning approaches such as Multiresolution.

BIBLIOGRAPHY

- [1] “The history of rfid technology,” *RFID Journal*, January 2005. 1
- [2] “Ic’s for tire pressure monitoring systems,” *Amtel Corporation*, 2006. 1
- [3] “United states department of defense suppliers passive rfid information guide,” <http://www.acq.osd.mil/log/rfid/index.htm>, 2007. 1
- [4] “Amex adds rfid to blue credit cards,” *RFID Journal*, June 2007. 1
- [5] “Nasco life/form auscultation trainer and smartscope.” 1
- [6] “Passive keyless entry (pke) reference design users manual,” *Microchip Corporation*, 2005. 1
- [7] G. Goth, “Rfid: Not quite prime time but dawdle at your own risk,” *IEEE Distributed Systems Online*, vol. 6, no. 2, 2005. 1
- [8] T. Smith, “Animal identification pilot program,” *USDA National Agricultural Library*, June 2006. 1
- [9] L. Sullivan, “Fda approves rfid tags for humans,” *Information Week*, October 2004. 1
- [10] D. H. Williams, “The strategic implications of wal-mart’s rfid mandate,” *Directions Magazine*, July 2004. 1
- [11] H. Stockman, “Communication by means of reflected power,” *Proceedings of the IRE*, vol. 36, no. 10, pp. 1196–1204, Oct. 1948. 2
- [12] *Title 47 Part 15 Section 225*. United States Code of Federal Regulations, 2007. 3
- [13] R. F. Harrington, *Field Computation by Moment Methods*. Malabar, Florida: Robert E. Krieger Publishing Company, Inc., 1968. 4
- [14] J. Jin, *The Finite Element Method in Electromagnetics*, 2nd ed. New York: John Wiley & Sons, Inc., 2002. 4
- [15] M. N. O. Sadiku, *Numerical Techniques in Electromagnetics*. Ann Arbor: CRC Press, 1992. 4

- [16] “Em studio: Static and low frequency design & analysis,” *Computer Simulation Technology Inc.*, 2008. 4
- [17] “Hfss & q3d: 3d full-wave electromagnetic field simulation,” *Ansoft Corporation*, 2008. 4
- [18] “Emcube propagation module: Advanced ray tracing solution.” *EMAG Technologies Inc.*, 2008. 4
- [19] “Ie3d: Full-wave em simulation, optimization, and synthesis package,” *Zeland Software Inc.*, 2008. 4
- [20] M. B. Bleszynski, E. and T. Jaroszewicz, “Aim: Adaptive integral method for solving large-scale electromagnetic scattering and radiation problems,” *Radio Sci.*, vol. 31, no. 5, Sept.-Oct. 1996. 5, 33, 40
- [21] R. Kindt, K. Sertel, E. Topsakal, and J. Volakis, “Array decomposition method for the accurate analysis of finite arrays,” *Antennas and Propagation, IEEE Transactions on*, vol. 51, no. 6, pp. 1364–1372, June 2003. 5, 33, 40, 58
- [22] E. Michielssen and A. Boag, “A multilevel matrix decomposition algorithm for analyzing scattering from large structures,” *Antennas and Propagation, IEEE Transactions on*, vol. 44, no. 8, pp. 1086–1093, August 1996. 5, 33
- [23] S. Rao, D. Wilton, and A. Glisson, “Electromagnetic scattering by surfaces of arbitrary shape,” *Antennas and Propagation, IEEE Transactions on [legacy, pre - 1988]*, vol. 30, no. 3, pp. 409–418, May 1982. 5, 28
- [24] E. Arvas and R. Harrington, “Computation of the magnetic polarizability of conducting disks and the electric polarizability of apertures,” *Antennas and Propagation, IEEE Transactions on [legacy, pre - 1988]*, vol. 31, no. 5, pp. 719–725, September 1983. 5
- [25] G. Vecchi, “Loop-star decomposition of basis functions in the discretization of the efie,” *Antennas and Propagation, IEEE Transactions on*, vol. 47, no. 2, pp. 339–346, February 1999. 5, 32
- [26] J.-S. Zhao and W. C. Chew, “Integral equation solution of maxwell’s equations from zero frequency to microwave frequencies,” *Antennas and Propagation, IEEE Transactions on*, vol. 48, no. 10, pp. 1635–1645, October 2000. 5, 27, 65, 70
- [27] F. Andriulli, F. Vipiana, and G. Vecchi, “Enhanced multi-resolution basis for the mom analysis of 3d structures,” *Antennas and Propagation International Symposium, 2007 IEEE*, 9-15 June 2007. 5, 72
- [28] F. Vipiana, P. Pirinoli, and G. Vecchi, “Spectral properties of the efie-mom matrix for dense meshes with different types of bases,” *Antennas and Propagation, IEEE Transactions on*, vol. 55, no. 11, pp. 3229–3238, November 2007. 5, 70, 72

- [29] F. Vipiana, G. Vecchi, and P. Pirinoli, “A multiresolution system of rao-wilton-glisson functions,” *Antennas and Propagation, IEEE Transactions on*, vol. 55, no. 3, pp. 924–930, March 2007. 5, 72
- [30] S. Kapur and D. Long, “Ies3: efficient electrostatic and electromagnetic simulation,” *Computational Science & Engineering, IEEE*, vol. 5, no. 4, Oct-Dec 1998. 5, 33
- [31] S. M. Seo and J.-F. Lee, “A single-level low rank ie-qr algorithm for pec scattering problems using efie formulation,” *Antennas and Propagation, IEEE Transactions on*, vol. 52, no. 8, pp. 2141–2146, August 2004. 5, 33
- [32] v. R. L. Greengard, J. Huang and S. Wandzura, “Accelerating fast multipole methods for the helmholtz equation at low frequencies,” *Computational Science & Engineering, IEEE*, vol. 5, no. 3, Jul-Sep 1998. 5, 33, 35
- [33] V. Rokhlin, “Rapid solution of integral equations of scattering theory in two dimensions,” *J. Comput. Phys.*, vol. 36, no. 2, pp. 414–439, 1990. 5, 33
- [34] E. M. J. S. W. C. Chew, J-M. Jin, *Fast and Efficient Algorithms in Computational Electromagnetics*. Boston, London: Artech House, Inc., 2001. 5, 26, 27, 35, 37, 38, 39, 41, 42, 66, 69
- [35] M. Ayatollahi and S. Safavi-Naeini, “Adaptive plane-wave expansion algorithm for efficient computation of electromagnetic fields in low-frequency-problems,” *IEE Proceedings Microwaves, Antennas and Propagation*, vol. 153, no. 2, April 2006. 5
- [36] E. M. B. Hu, W. C. Chew and J. Zhao, “Fast inhomogeneous plane wave algorithm for the fast analysis of two-dimensional scattering problems,” *Radio Science*, vol. 34, no. 4, pp. 759–772, July 1999. 5, 35
- [37] C. A. Balanis, *Advanced Engineering Electromagnetics*. New York: John Wiley & Sons, Inc., 1989. 9, 10, 12, 24, 82, 83
- [38] R. F. Harrington, *Time-Harmonic Electromagnetic Fields*. New York: McGraw-Hill, 1961. 9, 10, 12, 24, 99
- [39] E. Newman, “A sheet impedance approximation for electrically thick material shields,” *Antennas and Propagation, IEEE Transactions on*, vol. 50, no. 4, pp. 435–443, April 2002. 13, 15
- [40] T. Senior, “Combined resistive and conductive sheets,” *Antennas and Propagation, IEEE Transactions on [legacy, pre - 1988]*, vol. 33, no. 5, pp. 577–579, May 1985. 14, 18
- [41] D. L. Sengupta and V. V. Liepa, *Applied Electromagnetics and Electromagnetic Compatibility*. New York: John Wiley & Sons, Inc., 2006. 15

- [42] J. A. Stratton, *Electromagnetic Theory*. York, Pennsylvania: McGraw-Hill Book Company, Inc., 1941. 16, 24
- [43] C.-T. Tai, *Dyadic Green Functions in Electromagnetic Theory, 2nd. Edition*. New Jersey: IEEE Press, 1994. 23
- [44] J. V. Bladel, *Electromagnetic Fields*. New York: McGraw-Hill Book Company, Inc., 1964. 24, 100
- [45] J. L. Volakis, 1993, eECS 633 Coursepack. 25
- [46] P. Yla-Oijala and M. Taskinen, “Calculation of cfe impedance matrix elements with rwg and n/spl times/rwg functions,” *Antennas and Propagation, IEEE Transactions on*, vol. 51, no. 8, August 2003. 26
- [47] A. J. Buron and G. F. Miller, “The application of integral equation methods to the numerical solution of some exterior boundary-value problems,” *Proc. Roy. Soc. Lond. A.*, vol. 323, pp. 201–210, 1971. 26
- [48] D. K. Cheng, *Field and Wave Electromagnetics*. New York: Addison-Wesley Publishing Company, Inc., 1989. 27, 100
- [49] L. N. Trefethen and D. B. III, *Numerical Linear Algebra*. Philadelphia: SIAM, 1997. 32, 95
- [50] W. C. Chew, J.-M. Jin, C.-C. Lu, E. Michielssen, and J. Song, “Fast solution methods in electromagnetics,” *Antennas and Propagation, IEEE Transactions on*, vol. 45, no. 3, pp. 533–543, March 1997. 32
- [51] C. C. Lu and W. C. Chew, “A fast algorithm for solving the hybrid integral equation,” *IEE Proc. Pt. H*, vol. 140, no. 6, pp. 455–460, 1993. 33
- [52] V. R. R. Coifman and S. Wandzura, “The fast multipole method for the wave equation: a pedestrian prescription,” *Antennas and Propagation Magazine, IEEE*, vol. 35, no. 3, pp. 7–12, June 1993. 33
- [53] ———, “Faster single-stage multipole method for the wave equation,” *10th Annual Review of Progress in ACES*, pp. 19–24, 1994. 33
- [54] E. M. B. Hu, W. C. Chew and J. Zhao, “A Succinct Way To Diagonalize The Translation Matrix in Three Dimensions,” *Microwave and Optical Technology Letters*, vol. 15, no. 3, June 1997. 33, 35
- [55] J.-S. Zhao and W. C. Chew, “Three dimensional multilevel fast multipole algorithm at very low frequencies,” *Antennas and Propagation Society International Symposium, 2000. IEEE*, vol. 4, pp. 1884–1887, 2000. 35
- [56] R. Beatson and L. Greengard, *A short course on fast multipole methods*. <http://math.nyu.edu/faculty/greengar/>: Online. 35

- [57] S. Koc and W. C. Chew, "Calculation of acoustical scattering from a cluster of scatterers," *J. Acoust. Soc. Am.*, vol. 103, no. 2, February 1998. 37
- [58] J.-S. Zhao and W. C. Chew, "Applying matrix rotation to the three-dimensional low-frequency multilevel fast multipole algorithm," *Microwave and Optical Technology Letters*, vol. 26, no. 2, July 2000. 37
- [59] Y. Chu and W. C. Chew, "A fast algorithm for electrically small composite objects," *Antennas and Propagation Society International Symposium, 2004. IEEE*, vol. 4, pp. 3960–3963 Vol.4, 20-25 June 2004. 39
- [60] M. Carr, "Domain decomposition by iterative field bouncing," *Antennas and Propagation Society International Symposium, 2002. IEEE*, vol. 3, pp. 298–301 vol.3, 2002. 41
- [61] L. Hamandi, R. Lee, and F. Ozguner, "Review of domain-decomposition methods for the implementation of fem on massively parallel computers," *Antennas and Propagation Magazine, IEEE*, vol. 37, no. 1, pp. 93–98, February 1995. 41
- [62] Z. Lou and J.-M. Jin, "A novel dual-field time-domain finite-element domain-decomposition method for computational electromagnetics," *Antennas and Propagation, IEEE Transactions on*, vol. 54, no. 6, pp. 1850–1862, June 2006. 41
- [63] B. Stupfel, "A fast-domain decomposition method for the solution of electromagnetic scattering by large objects," *Antennas and Propagation, IEEE Transactions on*, vol. 44, no. 10, pp. 1375–1385, October 1996. 41
- [64] M. Vouvakis, K. Zhao, and J.-F. Lee, "Modeling large almost periodic structures using a non-overlapping domain decomposition method," *Antennas and Propagation Society International Symposium, 2004. IEEE*, vol. 1, pp. 343–346 Vol.1, 20-25 June 2004. 41
- [65] J. K. L. Tsang and K.-H. Ding, *Scattering of Electromagnetic Waves*. New York: John Wiley & Sons, Inc., 1964. 48, 50
- [66] E. W. Weisstein, "Nonlinear least squares fitting. <http://mathworld.wolfram.com/nonlinearleastquaresfitting.html>," *MathWorld – A Wolfram Web Resource*, 2007. 51
- [67] J.-S. Zhao and W. C. Chew, "Applying lfmlfma to solve complex pec structures," *Microwave and Optical Technology Letters*, vol. 28, no. 3, February 2001. 66
- [68] V. Okhmatovski, J. Morsey, and A. Cangellaris, "Enhancement of the numerical stability of the adaptive integral method at low frequencies through a loop-charge formulation of the method-of-moments approximation," *Microwave Theory and Techniques, IEEE Transactions on*, vol. 52, no. 3, pp. 962–970, March 2004. 69

- [69] M. Taskinen and P. Yla-Oijala, “Current and charge integral equation formulation,” *Antennas and Propagation, IEEE Transactions on*, vol. 54, no. 1, January 2006. 69
- [70] A. Peterson, C. Smith, and R. Mittra, “Eigenvalues of the moment-method matrix and their effect on the convergence of the conjugate gradient algorithm [em scattering],” *Antennas and Propagation, IEEE Transactions on*, vol. 36, no. 8, pp. 1177–1179, August 1988. 70, 72
- [71] Y.-H. Chu¹ and W. C. Chew, “Large-scale computation for electrically small structures using surface-integral equation method,” *Microwave and Optical Technology Letters*, vol. 47, no. 6, December 2005. 70
- [72] J. Brunett, V. Liepa, and D. Sengupta, “Extrapolating near-field emissions of low-frequency loop transmitters,” *Electromagnetic Compatibility, IEEE Transactions on*, vol. 47, no. 3, pp. 635–641, Aug. 2005. 82
- [73] D. M. Pozar, *Microwave Engineering*. Addison-Wesley, 1990. 87
- [74] T. M. Inc., “Matlab: The language of technical computing,” 2008. 99
- [75] “Co-netic and netic materials. <http://www.magnetic-shield.com/products>,” *Magnetic Shield Corporation*, 2008. 104
- [76] “Transportation recall enhancement, accountability, and documentation act,” *Congressional Record*, vol. 146, 2000. 106
- [77] A. Duduk, “Radial bias ply tire,” *Congressional Record. United States Patent*, vol. 146, no. 3672423, 1970. 107